Cluster Dynamical Mean-Field + Numerical Renormalization Group Approach to Strongly Correlated Systems

Andreas Gleis

Master's thesis

Chair of Theoretical Solid State Physics
Faculty of Physics
Ludwig-Maximilians-Universität München

Supervisor:
Prof. Dr. Jan von Delft

Cluster Dynamische Molekularfeldtheorie + Numerische Renormalisierungsgruppe zur Behandlung stark korrelierter Systeme

Andreas Gleis

Masterarbeit

Lehrstuhl für theoretische Festkörperphysik
Fakultät für Physik
Ludwig-Maximilians-Universität München

Betreuer:
Prof. Dr. Jan von Delft

Contents

1 Introduction

The discovery of cuprate high-T_c superconductors in 1986 by Bednorz and Müller [1] has surged major theoretical and experimental research on strongly correlated materials, leading over the years to an ever growing list of compounds showing phenomena strikingly different from normal metals like copper. These include, among others, unconventional superconductivity, pseudogap phases or metallic states, often aptly named "strange metals", with behavior vastly different from conventional Fermi liquid theory, for example showing a linear temperature dependence of the resistivity.

In order to describe and understand the intriguing phenomena of these systems, going beyond the paradigm of Fermi liquid theory, numerous theoretical tools have been developed in the past. Arguably one of the most successful of these is the dynamical mean-field theory (DMFT) [2]. It is an inherently non-perturbative approach, which maps an interacting lattice model locally onto an effective impurity model. The information on the lattice structure is then introduced via a self-consistency condition. While DMFT has been a major step forward in the description of strongly correlated systems, it cannot describe non-local correlations due to its entirely local approach.

However, many of these strongly correlated materials show clear signs of the importance of non-local correlations, for example the pseudogap phase in cuprates, where instead of a closed Fermi surface, Fermi arcs are formed, or in heavy fermion systems, where the competition of non-local magnetic correlations and local screening leads to a quantum phase transition and vast regions of non Fermi liquid behavior. This calls for extensions of DMFT to incorporate such non-local effects. In this thesis, we concern ourselves with probably the most mundane of these methods, so called quantum cluster methods [3]. The idea of these cluster extensions is to map the lattice model onto a small cluster model, thereby including short ranged non-local correlations. This cluster model is then usually be solved numerically, and whereas most commonly quantum monte carlo (QMC) methods are used, in this thesis the numerical renormalization group (NRG) [4] has been employed.

NRG, while certainly not able to reach the cluster sizes possible with QMC, nevertheless has many important advantages. First and foremost, it is able to reach arbitrary low temperatures and to resolve exponentially small energy scales, which is a major problem for QMC. Second, it generates dynamical data directly on the real axis, and is thus not dependent on analytic continuation of Matsubara data, which is numerically ill posed and prone to errors. Other than that, the NRG also generates a renormalization group flow, which provides further information apart from dynamical correlators. The NRG code used for this thesis has already been available in Jan von Delft's group and has been implemented by Andreas Weichselbaum and Seung-Sup Lee. It is one of the most highly developed NRG codes available to date, and its power has been demonstrated in various publications, including DMFT studies on models with up to three orbitals.

However, applications on quantum cluster methods are to date not among these. It is further noticeable that only two applications of NRG to cluster methods are recorded at the time of this writing [5, 6]. This is owed to the Brillouin zone integration of the lattice Green's functions,

which is necessary for cluster methods. While on the Matsubara axis, one can get away with simple $\vec{k}$-sums, this is vastly different on the real axis, especially at low temperatures, due to the pole structure of the Green's function. This has lead to the main technical achievement in the course of this thesis, which was the development of reliable and fast integration routines based on the tetrahedron method to tackle this problem.

The thesis is structured as follows. In chapter 2, the dynamical mean-field theory is introduced. It will be presented in the Baym-Kadanoff formalism, which is a particularly convenient starting point to understand cluster extensions to DMFT, which are introduced in chapter 3. There, the emphasis will be on the most popular cluster methods used to date, the cellular dynamical mean-field theory (CDMFT) and the dynamical cluster approximation (DCA). This will then lead us to the short introduction of NRG in chapter 4, where a two site cluster model will serve as an example and some specifics regarding these will be mentioned. In chapter 5 we will concern ourselves with the Brillouin zone integration, where the technical details of the implementation of the integration methods developed for this thesis are given. Having explained the methodological part of the thesis, in chapters 6 and 7, results follow. Chapter 6, where a two-site cluster approximation to the Hubbard model is introduced, will mainly serve as a benchmark test against QMC results obtained by Ferrero *et al.* [7]. It will therefore be very short as no new results where obtained there. Chapter 7, however, will show the main results of this thesis. There, the quantum critical point in the periodic Anderson model (PAM), based on previous studies by de Leo *et al.* [8, 9], will be reconsidered.

2 Dynamical Mean-Field Theory

Since its development around 30 years ago, the dynamical mean-field theory (DMFT) has been an invaluable, non-perturbative method to treat lattice models with strong electronic correlations (for reviews, see [2, 10]). The foundations of DMFT were laid by Metzner and Vollhardt [11] and Georges and Kotliar [12], by considering the Hubbard model in the limit of infinite dimensions and its relation to the Anderson impurity model. Their key insight was that in $d \to \infty$, only purely local correlation effects remain, rendering the system locally indistinguishable from an effective impurity model. To derive the DMFT equations, I will use the Baym-Kadanoff formalism [13, 14]. While there are a lot of different ways to derive the DMFT equations (see e.g. [2, 15, 16]), the Baym-Kadanoff formalism seems to be a nice starting point to generate cluster extensions to DMFT, which is the main topic of this thesis.

2.1 Model and basic notations

In this section, some basic notations on Green's functions will be introduced. For more information on this, see [17, 18] and related textbooks. To motivate the DMFT, I will use the example of the Hubbard model on a cubic lattice in d dimensions, which is described by the Hamiltonian

$$H = H_{\text{kin}} + H_{\text{int}} - \mu N = -t \sum_{\langle i,j\rangle,\sigma} c^\dagger_{i,\sigma} c_{j,\sigma} + U \sum_i n_{i,\uparrow} n_{i,\downarrow} - \mu \sum_{i,\sigma} n_{i,\sigma} \quad . \tag{2.1}$$

Here, $\sum_{\langle i,j\rangle}$ denotes a sum over pairs of nearest neighbors, $c_{i,\sigma}$ the annihilation operator for an electron at site i with spin $\sigma \in \{\uparrow,\downarrow\}$ and $n_{i,\sigma} = c^\dagger_{i,\sigma} c_{i,\sigma}$ is the number operator. Fourier transforming the kinetic part gives

$$H_{\text{kin}} = \sum_{\vec{k},\sigma} \epsilon(\vec{k}) c^\dagger_{\vec{k},\sigma} c_{\vec{k},\sigma} \quad , \tag{2.2}$$

with the dispersion relation (lattice spacing $\equiv 1$)

$$\epsilon(\vec{k}) = -2t \sum_{\alpha=1}^{d} \cos(k_\alpha) \quad . \tag{2.3}$$

The central quantity of interest in DMFT is the Green's function

$$G_{i,j}(i\omega_n) = \int_0^\beta \mathrm{d}\tau e^{i\omega_n \tau} G_{i,j}(\tau) = -\int_0^\beta \mathrm{d}\tau \, \langle \mathcal{T}_\tau c_{i,\sigma}(\tau) c^\dagger_{j,\sigma} \rangle \quad , \tag{2.4}$$

where $c_{i,\sigma}(\tau) = e^{H\tau} c_{i,\sigma} e^{-H\tau}$ is the imaginary time evolved annihilation operator, $\beta = \frac{1}{T}$ the inverse temperature, $\omega_n = T\pi(2n+1)$, n integer, a fermionic Matsubara-frequency and $\mathcal{T}_\tau$ the time ordering operator along the imaginary axis, while $\langle A \rangle$ denotes the grand canonical average of the operator A. In the following, we will assume translation invariance, in the case of which $\boldsymbol{G}(i\omega_n)$ is diagonal in momentum-space

$$G(\vec{k}, i\omega_n) = \frac{1}{i\omega_n + \mu - \epsilon(\vec{k}) - \Sigma(\vec{k}, i\omega_n)} = \frac{1}{\mathcal{G}_0^{-1}(\vec{k}, i\omega_n) - \Sigma(\vec{k}, i\omega_n)} \quad . \tag{2.5}$$

Here, we have introduced the non-interacting ($U = 0$) Green's function $\mathcal{G}_0(\vec{k}, i\omega_n)$ and the self-energy $\Sigma(\vec{k}, i\omega_n)$, encoding interaction effects. Eq. (2.5) can be rewritten in the form

$$\boldsymbol{G}(i\omega_n) = \boldsymbol{\mathcal{G}}_0(i\omega_n) + \boldsymbol{\mathcal{G}}_0(i\omega_n)\boldsymbol{\Sigma}(i\omega_n)\boldsymbol{G}(i\omega_n) \tag{2.6}$$

which is known as Dyson's equation and has the diagrammatic representation

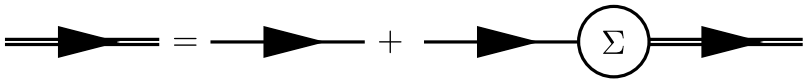

where the double line denotes the full propagator, the single line the non-interacting propagator and the circle the self-energy. We will later see that in $d \to \infty$, the self-energy becomes momentum independent, allowing its calculation from a self-consistent impurity model. Note that to make contact with experiments, the Matsubara Green's function Eq. (2.4) has to be analytically continued ($i\omega_n \to \omega + i0^+$) to the real axis. This then yields the retarded Green's function

$$G_{i,j}(\omega) = -i \int_{-\infty}^{\infty} \mathrm{d}t e^{i\omega t} \Theta(t) \left\langle \{c_{i,\sigma}(t), c_{j,\sigma}^\dagger\} \right\rangle \quad , \tag{2.7}$$

where $\{.,.\}$ is the anti-commutator and $c_{i,\sigma}(t) = e^{iHt} c_{i,\sigma} e^{-iHt}$ the real-time evolution of the annihilation operator. Because with the Numerical Renormalization Group (NRG) (see chapter 4) we are able to directly access the retarded Green's function, we will later solve the DMFT equations on the real axis. As analytic continuation is numerically ill posed, this will prove very valuable, especially at low temperatures. In the derivation of the DMFT equations, the Matsubara representation is more convenient though.

2.2 Luttinger-Ward functional

In general, the self-energy cannot be computed exactly. We will therefore need to rely on approximations. It is desirable that these approximations fulfill as many exactly known relations as possible. Thermodynamically consistent approximations [13, 14] can be constructed by requiring that the self-energy is generated as the derivative of a functional $\Phi_U[\boldsymbol{G}]$ of the full Green's function, evaluated at the physical one fulfilling Dyson's equation.

$$\begin{aligned} \boldsymbol{\Sigma}_U[\boldsymbol{G}(i\omega_n)] &= \frac{\delta \Phi_U[\boldsymbol{G}]}{\delta \boldsymbol{G}(i\omega_n)} \\ \boldsymbol{G}(i\omega_n) &= \left(\boldsymbol{\mathcal{G}}_0^{-1}(i\omega_n) - \boldsymbol{\Sigma}_U[\boldsymbol{G}(i\omega_n)] \right)^{-1} \end{aligned} \tag{2.8}$$

The functional $\Phi_U[\boldsymbol{G}]$ is called the Luttinger-Ward (LW) functional [19]. Its functional dependence is completely determined by the interaction. Diagrammatically, it is defined as the sum of all vacuum to vacuum skeleton diagrams.

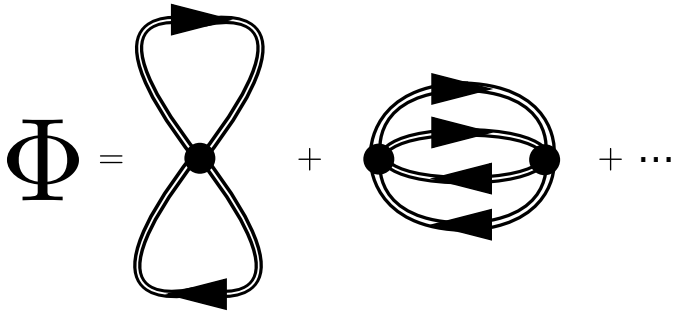

For a non-perturbative construction of the LW functional, see [20]. Taking the derivative of $\Phi_U[\boldsymbol{G}]$ removes a propagator line and gives the skeleton expansion of the self-energy.

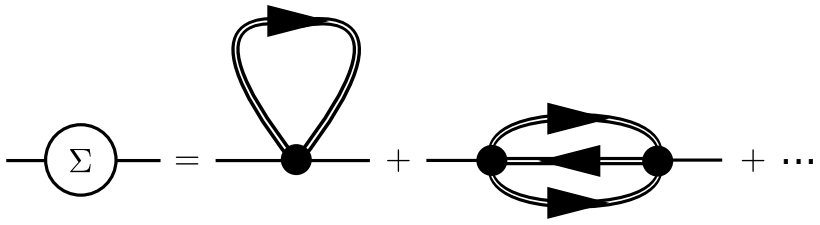

As usually no explicit expression for $\Phi_U[\boldsymbol{G}]$ is known, one relies on approximations to the LW functional. In a certain approximation, the equations Eq. (2.8) are then solved self-consistently. The self-consistency equations Eq. (2.8) can be understood as a condition for the grand-potential

$$\Omega[\boldsymbol{G}] = T\Phi_U[\boldsymbol{G}] + T\sum_n \mathrm{Tr}\big(\log\left(\boldsymbol{G}(i\omega_n)\right) - \boldsymbol{\Sigma}(i\omega_n)\boldsymbol{G}(i\omega_n)\big) \tag{2.9}$$

to be stationary as a functional of the Green's function [19]. In the following, we will see that the LW functional and the self-energy become local in $d \to \infty$, which results in the DMFT as a non-perturbative approximation scheme in finite dimensions.

2.3 The limit of infinite dimensions

It turns out that quantum lattice problems become greatly simplified, but not trivial in the limit of infinite dimensions, if the hopping amplitudes are scaled correctly to give a finite kinetic energy. In the following, this scaling is motivated for the Hubbard model Eq. (2.1) on the $d \to \infty$ dimensional cubic lattice. To keep the kinetic energy

$$E_{\mathrm{kin}} = \int_{-\pi}^{\pi} \frac{\mathrm{d}\vec{k}}{(2\pi)^d} \epsilon(\vec{k}) \sum_\sigma \langle c^\dagger_{\vec{k},\sigma} c_{\vec{k},\sigma} \rangle \tag{2.10}$$

finite, we demand that the width of the density of states (DOS)

$$D(\epsilon) = \int_{-\pi}^{\pi} \frac{\mathrm{d}\vec{k}}{(2\pi)^d} \delta(\epsilon - \epsilon(\vec{k})) \tag{2.11}$$

is independent of d. A measure for the width of the DOS is its variance

$$\langle \epsilon^2 \rangle_D = \int_{-\infty}^{\infty} \mathrm{d}\epsilon D(\epsilon)\epsilon^2 = 2t^2 d \quad . \tag{2.12}$$

To keep the variance independent of d, t has to be scaled like

$$t = \frac{t^\star}{\sqrt{d}} \quad , \tag{2.13}$$

where $t^\star$ is a constant independent of d [11]. Note that with this rescaling, the total band-width becomes infinite for $d \to \infty$, though most of the weight of $D(\epsilon)$ is positioned in an interval of width $\sim 2\sqrt{2}t^\star$ around 0. This can also be seen from actual expression of the DOS in the $d \to \infty$ limit [21], which can be calculated via the central limit theorem. We can view

$$X_\alpha = -2t\cos(k_\alpha) \tag{2.14}$$

as independent random variables with zero mean and variance $2t^2$:

$$\begin{aligned}\langle X_\alpha \rangle &= -2t \int_{-\pi}^{\pi} \frac{\mathrm{d}\vec{k}}{(2\pi)^d} \cos(k_\alpha) = 0 \\ \langle X_\alpha X_\beta \rangle &= 4t^2 \int_{-\pi}^{\pi} \frac{\mathrm{d}\vec{k}}{(2\pi)^d} \cos(k_\alpha)\cos(k_\beta) = 2t^2 \delta_{\alpha,\beta} \quad .\end{aligned} \tag{2.15}$$

By the central limit theorem, distribution function of

$$X = \frac{\sum_{\alpha=1}^{d} X_\alpha}{\sqrt{2dt^2}} \tag{2.16}$$

thus goes to a Gaussian with width 1 in the $d \to \infty$ limit. Therefore, the DOS, which is the distribution function of $\epsilon = \sqrt{2dt^2}X$, also goes towards a Gaussian:

$$D(\epsilon) = \frac{1}{\sqrt{2\pi d}\cdot t} \exp\left(-\frac{\epsilon^2}{2dt^2}\right) \overset{(2.13)}{=} \frac{1}{\sqrt{2\pi}\cdot t^\star} \exp\left(-\frac{\epsilon^2}{2t^{\star 2}}\right) \quad . \tag{2.17}$$

It is clear that the scaling Eq. (2.13) is the correct way to arrive at a non-trivial DOS.

2.4 Local nature of Φ_U and Σ in infinite dimensions

By construction, the kinetic energy per site [10]

$$E_{\text{kin}} = -2t \sum_{\sigma, j \in \text{nn}(i)} \langle c^\dagger_{i,\sigma} c_{j,\sigma} \rangle \quad , \tag{2.18}$$

where $\text{nn}(i)$ denotes the set of nearest neighbors of i, is independent of d in the large d limit. As the number of nearest-neighbors is of order d, but $t \sim \mathcal{O}(1/\sqrt{d})$,

$$\langle c^\dagger_{i,\sigma} c_{j,\sigma} \rangle = G_{j,i}(\tau = 0^-) \sim \mathcal{O}\left(\frac{1}{\sqrt{d}}\right) \quad . \tag{2.19}$$

The Green's function is therefore of $\mathcal{O}\left(1/\sqrt{d}\right)$ if i and j are nearest neighbors. It can be shown [22, 23] that

$$G_{i,j}(i\omega_n) \sim \mathcal{O}\left(\frac{1}{d^{||\vec{R}_i - \vec{R}_j||/2}}\right) \tag{2.20}$$

for general i, j, where $||\vec{R}|| = \sum_{\alpha=1}^{d} |R_\alpha|$ is the norm in the Manhattan metric, $\vec{R}$ is a lattice vector with $\vec{R} = \sum_{\alpha=1}^{d} R_\alpha \vec{a}_\alpha$ and $\vec{a}_\alpha$ are the primitive lattice vectors. From the skeleton expansion of the self-energy, we see that two vertices are always connected by at least three Green's function lines. This implies that the non-local self-energy $\Sigma_{i,j}(\omega)$ scales with $\sim \mathcal{O}(d^{-\frac{3}{2}||\vec{R}_i - \vec{R}_j||})$. As the self-energy enters always in a sum over its external labels, we have to sum over j at a fixed distance while keeping i fixed to compare it to the local contribution. This gives a factor of $\sim \mathcal{O}(d^{||\vec{R}_i - \vec{R}_j||})$, so in total the non-local contributions at Manhattan distance $||\vec{R}_i - \vec{R}_j||$ contribute with order $\sim \mathcal{O}(d^{-\frac{1}{2}||\vec{R}_i - \vec{R}_j||})$ compared to the local one, and are thus sub-leading [10, 2]. Therefore, in the $d \to \infty$ limit, only the local part remains and $\mathbf{\Sigma}$ becomes site diagonal in real-space or $\vec{k}$-independent in momentum space.

$$\begin{aligned}\Sigma_{i,j}(i\omega_n) &\overset{d\to\infty}{=} \delta_{i,j}\Sigma(i\omega_n) \\ \Sigma(\vec{k}, i\omega_n) &\overset{d\to\infty}{=} \Sigma(i\omega_n)\end{aligned} \tag{2.21}$$

The locality of the self-energy can also be seen from a momentum-space perspective [21]. Since the free propagator depends on momentum only via $\epsilon(\vec{k})$, the momentum conservation on internal vertices is governed by the vertex function

$$\begin{aligned} v(\epsilon_1, \epsilon_2, \epsilon_3, \epsilon_4) = \int_{-\pi}^{\pi} \prod_{l=1}^{4} \frac{\mathrm{d}\vec{k}_l}{2\pi} \delta(\epsilon_l - \epsilon(\vec{k}_l)) \Delta_{\mathrm{Laue}}(\vec{k}_1 - \vec{k}_2 + \vec{k}_3 - \vec{k}_4) \\ \Delta_{\mathrm{Laue}}(\vec{k}) = \sum_{\vec{R}} \exp(i\vec{R}\vec{k}) \end{aligned} \tag{2.22}$$

where $\Delta_{\mathrm{Laue}}(\vec{k})$ is called the Laue function, ensuring proper momentum conservation up to reciprocal lattice vectors. A straightforward calculation [21] shows

$$v(\epsilon_1, \epsilon_2, \epsilon_3, \epsilon_4) = \prod_{l=1}^{4} D(\epsilon_l) + \mathcal{O}(\frac{1}{d}) \tag{2.23}$$

thus

$$\Delta_{\mathrm{Laue}}(\vec{k}) \overset{d\to\infty}{\to} 1 \tag{2.24}$$

which means momentum conservation at the vertices can be ignored in $d \to \infty$. Therefore, all propagators enter the expansion only via the local propagator

$$G_{i,i}(i\omega_n) = \int_{-\infty}^{\infty} \mathrm{d}\epsilon D(\epsilon) G(\epsilon, i\omega_n) \tag{2.25}$$

which in turn renders the self-energy local. The locality of the self-energy in turn means that the LW functional in $d \to \infty$ becomes dependent on the local propagator only [2].

$$\Sigma_{i,j}(i\omega_n) = \left. \frac{\delta \Phi_U[\boldsymbol{G}]}{\delta G_{i,j}(i\omega_n)} \right|_{\boldsymbol{G}=\boldsymbol{G}_{\mathrm{phys}}} = \delta_{i,j} \Sigma(i\omega_n) \tag{2.26}$$

The LW functional can therefore be written as a sum over functionals depending on the local propagator on every site [2].

$$\Phi_U[\boldsymbol{G}] = \sum_i \phi_U[G_{i,i}] \tag{2.27}$$

2.5 Relation to impurity models

Despite its simplified form, the functional Eq. (2.27) is still unknown. As the functional $\phi_U[G_{i,i}]$ is determined by a purely local interaction and depends only on a local propagator, it should be possible to generate it from a model with interactions on a single localized site [2]. To represent possible branch cuts in $G_{i,i}$ on the real axis, the model should nevertheless have $\to \infty$ degrees of freedom. It turns out [12, 2] that the functional ϕ is the LW functional of an impurity model with the same local impurity Hamiltonian as the local lattice Hamiltonian.

$$H_{\mathrm{loc,latt}} = -\mu \sum_{\sigma} c_\sigma^\dagger c_\sigma + U n_\uparrow n_\downarrow \overset{!}{=} H_{\mathrm{imp}} \tag{2.28}$$

The whole impurity model consists of an interacting impurity Hamiltonian H_{imp} which is coupled to a non interacting, infinitely large bath described by H_{bath} via a hybridization Hamiltonian H_{hyb}.

$$\begin{aligned} H &= H_{\text{imp}} + H_{\text{bath}} + H_{\text{hyb}} \\ H_{\text{imp}} &= -\mu \sum_{\sigma} c_{\sigma}^{\dagger} c_{\sigma} + U n_{\uparrow} n_{\downarrow} \\ H_{\text{bath}} &= \sum_{\lambda} \epsilon_{\lambda,\sigma} a_{\lambda,\sigma}^{\dagger} a_{\lambda,\sigma} \\ H_{\text{hyb}} &= \sum_{\lambda,\sigma} (V_{\lambda} a_{\lambda,\sigma}^{\dagger} c_{\sigma} + \bar{V}_{\lambda} c_{\lambda}^{\dagger} a_{\lambda,\sigma}) \end{aligned} \tag{2.29}$$

The Green's function of such an impurity model then reads

$$G_{\text{imp}}(i\omega_n) = \frac{1}{\mathcal{G}_{0,\text{imp}}^{-1}(i\omega_n) - \Sigma_{\text{imp}}(i\omega_n)} = \frac{1}{i\omega_n + \mu - \Delta(i\omega_n) - \Sigma_{\text{imp}}(i\omega_n)} \quad , \tag{2.30}$$

where

$$\Delta(i\omega_n) = \sum_{\lambda} \frac{|V_{\lambda}|^2}{i\omega_n - \epsilon_{\lambda}} \tag{2.31}$$

is the hybridization function describing hopping from the impurity into the bath and back onto the impurity while $\Sigma_{\text{imp}}(i\omega_n)$ encodes interaction effects. The Σ-functional

$$\Sigma[G(i\omega_n)] = \frac{\delta \phi_U[G]}{\delta G(i\omega_n)} \tag{2.32}$$

can then be evaluated at $G = G_{\text{imp}}$ by solving the impurity model. This is exploited in DMFT to solve the self-consistency equations Eq. (2.8) in the approximation Eq. (2.27).

2.6 DMFT equations

The dynamical mean-field theory, assumes a LW functional of the form Eq. (2.27) even in finite dimensions [2]. The self-consistency equation Eq. (2.8) then gives

$$G_{i,i}(i\omega_n) \equiv G_{\text{loc}}(i\omega_n) = \int_{-\pi}^{\pi} \frac{\mathrm{d}\vec{k}}{(2\pi)^d} \left(\mathcal{G}_{0,\text{latt}}^{-1}(\vec{k}, i\omega_n) - \Sigma[G_{\text{loc}}(i\omega_n)] \right)^{-1} \quad , \tag{2.33}$$

where $\mathcal{G}_0(\vec{k}, i\omega_n)$ is the non-interacting lattice propagator and $\Sigma[G] = \frac{\delta \phi[G]}{\delta G}$ is the self-energy as a functional of G. As $\Sigma[G]$ is not available in a closed form, one has to rely on evaluating the functional via an impurity model. For a particular choice of the hybridization $\Delta(i\omega_n)$, calculating the self-energy gives the Σ-functional

$$\Sigma[G_{\text{imp}}(i\omega_n)] = \Sigma_{\text{imp}}(i\omega_n) \equiv \Sigma(i\omega_n) \tag{2.34}$$

evaluated at the corresponding $G_{\text{imp}}(i\omega_n)$ Eq. (2.30). Consequently, Eq. (2.33) when $\Delta(i\omega_n)$ is chosen such that

$$\begin{aligned} G_{\text{loc}}(i\omega_n) &\stackrel{!}{=} G_{\text{imp}}(i\omega_n) \\ \int_{-\pi}^{\pi} \frac{\mathrm{d}\vec{k}}{(2\pi)^d} \left(\mathcal{G}_0^{-1}(\vec{k}, i\omega_n) - \Sigma(i\omega_n) \right)^{-1} &\stackrel{!}{=} \left(\mathcal{G}_{0,\text{imp}}^{-1}(i\omega_n) - \Sigma(i\omega_n) \right)^{-1} \quad , \end{aligned} \tag{2.35}$$

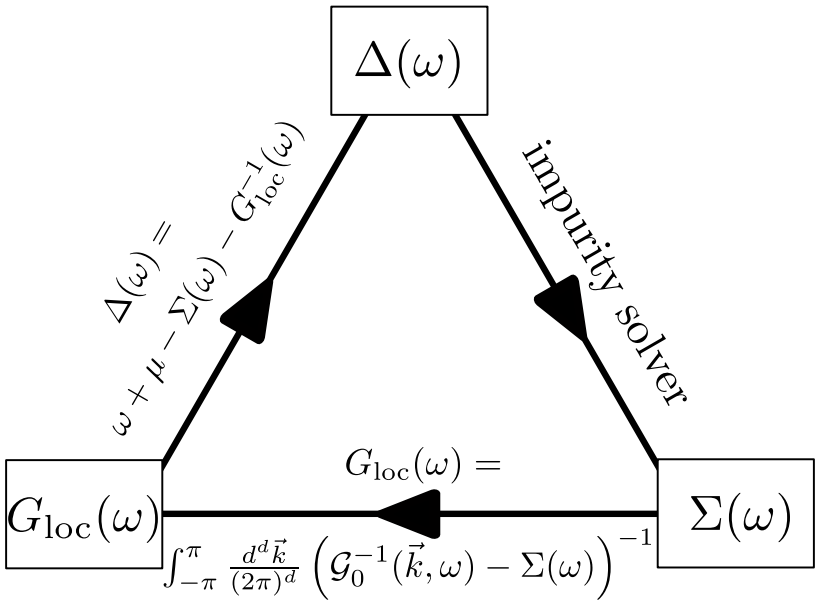

Figure 2.1: graphical illustration of the DMFT self-consistency cycle

where $\mathcal{G}_{0,\rm imp}^{-1}(i\omega_n) = i\omega_n + \mu - \Delta(i\omega_n)$ is the non-interacting impurity Green's function. This equation is the DMFT self-consistency equation. $\Delta(i\omega_n)$ or $\mathcal{G}_{0,\rm imp}(i\omega_n)$ are often called a dynamical mean-field. In principle, any approach leading to the right $\Delta(i\omega_n)$, which fulfills Eq. (2.35), can be used. In practice, usually the iterative scheme

$$\Delta_{\rm new}(i\omega_n) = i\omega_n + \mu - \Sigma(i\omega_n) - G_{\rm loc}^{-1}(i\omega_n) \tag{2.36}$$

is used. Here $\Sigma(i\omega_n)$ and $G_{\rm loc}(\omega)$ are the self-energy and the local Green's function calculated with a given input $\Delta_{\rm old}(i\omega_n)$. The input for the next iteration is then $\Delta_{\rm new}(i\omega_n)$. Eq. (2.36) is terminated when $\Delta_{\rm new}(i\omega_n) = \Delta_{\rm old}(i\omega_n)$. It should again be noted that the DMFT self-consistency equation can be solved both on the Matsubara axis or on the real axis. While in principle there is no difference in choosing either, in practice the Matsubara data must be analytically continued to the real axis to connect to experiments. As analytic continuation is numerically ill posed and can lead to large errors in the real-frequency data if small errors in the Matsubara-data exist, it is desirable to solve Eq. (2.35) directly on the real axis. This is possible when using the NRG to solve the impurity model. In the following, the DMFT algorithm is summarized, choosing ω on the real axis:

1. the algorithm is initialized with some guess for $\Delta(\omega)$
2. solve the impurity model to obtain $\Sigma(\omega)$. In this thesis, the NRG (Ch.4) is chosen for this step.
3. calculate the local lattice Green's function $G_{\rm loc}(\omega) = \int_{-\pi}^{\pi} \frac{\mathrm{d}\vec{k}}{(2\pi)^d} \left(\mathcal{G}_0^{-1}(\vec{k},\omega) - \Sigma(\omega)\right)^{-1}$. For this step, the tetrahedron method (Ch.5) was used in this thesis.
4. update the dynamical mean field $\Delta_{\rm new}(\omega) = \omega + \mu - \Sigma(\omega) - G_{\rm loc}^{-1}(\omega)$. Go to step 2 and iterate until convergence is reached.

3 Cluster Extensions to DMFT

In this chapter the two most commonly used cluster extensions to dynamical mean-field theory, the cellular dynamical mean-field theory (CDMFT) [24] and the dynamical cluster approximation (DCA) [25, 26], are described. These extensions are designed to incorporate short ranged non-local corrections to the self-energy in a non-perturbative way. The two approaches can be understood as an approximation to the Luttinger-Ward functional of the lattice problem by one which can be generated by a small cluster model. For a review of these methods, see [3]. In the following, the cluster methods will be explained using the $d = 2$ Hubbard model (Eq. (2.1)) on a square lattice as an example. If specified, a cluster size of $N_c = 2$ will be chosen.

3.1 Cellular dynamical mean-field theory

CDMFT [24] is best understood from a real-space perspective. The lattice is tiled into a super-lattice of cells with N_c sites per cell, an example for $N_c = 2$ is shown in Fig. 3.1. In the following, the Green's function is written in a matrix representation

$$\begin{aligned} \boldsymbol{G}_{i,j}(\omega) &= \int_{-\pi}^{\pi} \frac{\mathrm{d}\vec{K}}{(2\pi)^2} \exp(i\vec{K}(\vec{R}_i - \vec{R}_j))\boldsymbol{G}(\vec{K},\omega) \\ \boldsymbol{G}(\vec{K},\omega) &= \left(\boldsymbol{\mathcal{G}}_0^{-1}(\vec{K},\omega) - \boldsymbol{\Sigma}(\vec{K},\omega)\right)^{-1} \quad , \end{aligned} \tag{3.1}$$

where $\boldsymbol{G}$, $\boldsymbol{\mathcal{G}}_0$ and $\boldsymbol{\Sigma}$ are $N_c \times N_c$ matrices in the intra-cell site index while $\vec{R}_i$ and $\vec{R}_j$ denote the position of the cell in the super-lattice and $\vec{K}$ is a reciprocal lattice vector in the first Brillouin zone of the super-lattice. Similar to the DMFT, the dependence of the LW functional on the inter-cell propagator is neglected.

$$\Phi_U[\boldsymbol{G}] \overset{\mathrm{CDMFT}}{=} \sum_i \phi_U[\boldsymbol{G}_{i,i}] \tag{3.2}$$

As a consequence, the self-energy is confined within a cell and therefore independent of $\vec{K}$.

$$\begin{aligned} \boldsymbol{\Sigma}_{i,j}(\omega) &\overset{CDMFT}{=} \boldsymbol{\Sigma}(\omega)\delta_{i,j} \\ \boldsymbol{\Sigma}(\vec{K},\omega) &\overset{CDMFT}{=} \boldsymbol{\Sigma}(\omega) \end{aligned} \tag{3.3}$$

The self-consistency equation (2.8) then reads

$$\boldsymbol{G}_{\mathrm{loc}}(\omega) \equiv \boldsymbol{G}_{i,i}(\omega) = \int_{-\pi}^{\pi} \frac{\mathrm{d}\vec{K}}{(2\pi)^d} \left(\boldsymbol{\mathcal{G}}_0^{-1}(\vec{K},\omega) - \boldsymbol{\Sigma}_U[\boldsymbol{G}_{\mathrm{loc}}(\omega)]\right)^{-1} \quad , \tag{3.4}$$

where the Σ-functional must be evaluated with the help of a N_c-site cluster model. Its Hamiltonian is given by

$$H_{\mathrm{c}} = H_{\mathrm{cl}} + H_{\mathrm{bath}} + H_{\mathrm{hyb}} \tag{3.5}$$

where H_{cl} is the interacting Hamiltonian of a N_c site cell of the lattice model while H_{bath} describes a non-interacting continuous bath and H_{hyb} the hybridization of bath and impurity.

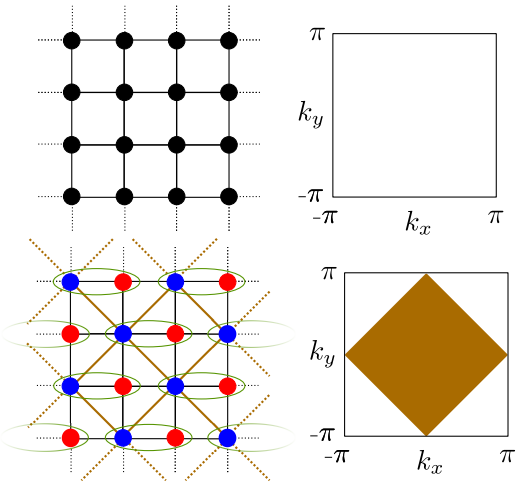

Figure 3.1: Tiling of a $d = 2$ square lattice into a super-lattice of two-site clusters. On the right, the first Brillouin zone of the super-lattice is shown in yellow.

For the case of $N_c = 2$ on the 2 dimensional Hubbard model

$$\begin{aligned} H_{\mathrm{cl}} &= -t \sum_{\sigma} \left(c^{\dagger}_{1,\sigma} c_{2,\sigma} + h.c. \right) + U \sum_{i=1}^{2} n_{i,\uparrow} n_{i,\downarrow} + \mu \sum_{i=1,2;\sigma} n_{i,\sigma} \\ H_{\mathrm{bath}} &= \sum_{i=1,2;\lambda,\sigma} \epsilon_{(i,\lambda)} a^{\dagger}_{(i,\lambda),\sigma} a_{(i,\lambda),\sigma} \\ H_{\mathrm{hyb}} &= \sum_{i,j,\lambda,\sigma} \left(V_{i,(j,\lambda)} c^{\dagger}_{i,\sigma} a_{(j,\lambda),\sigma} + h.c. \right) \quad , \end{aligned} \tag{3.6}$$

with cluster Green's function

$$\begin{aligned} \boldsymbol{G}_{\mathrm{cl}}(\omega) &= \left(\boldsymbol{\mathcal{G}}^{-1}_{0,\mathrm{cl}}(\omega) - \boldsymbol{\Sigma}_{\mathrm{cl}}(\omega) \right)^{-1} \\ \boldsymbol{\mathcal{G}}^{-1}_{0,\mathrm{cl}}(\omega) &= \omega + \mu + t \cdot \boldsymbol{\sigma}_x - \boldsymbol{\Delta}(\omega) \end{aligned} \tag{3.7}$$

where $\boldsymbol{\sigma}_x$ is the x-Pauli-matrix,

$$\boldsymbol{\Delta}_{i,j}(\omega) = \sum_{(l,\lambda)} \frac{V_{i,(l,\lambda)} \bar{V}_{j,(l,\lambda)}}{\omega - \epsilon_{(l,\lambda)}} \tag{3.8}$$

the hybridization function and

$$\boldsymbol{\Sigma}_{\mathrm{cl}}(\omega) = \boldsymbol{\Sigma}_U[\boldsymbol{G}_{\mathrm{cl}}(\omega)] \equiv \boldsymbol{\Sigma}(\omega) \tag{3.9}$$

the cluster self-energy and thus the Σ-functional evaluated at $\boldsymbol{G}_{\mathrm{cl}}$. We therefore need to find $\boldsymbol{\Delta}(\omega)$ such that

$$\begin{aligned} \boldsymbol{G}_{\mathrm{cl}}(\omega) &\stackrel{!}{=} \boldsymbol{G}_{\mathrm{loc}}(\omega) \\ \left(\boldsymbol{\mathcal{G}}^{-1}_{0,\mathrm{cl}}(\omega) - \boldsymbol{\Sigma}(\omega) \right)^{-1} &\stackrel{!}{=} \int_{-\pi}^{\pi} \frac{\mathrm{d}\vec{K}}{(2\pi)^d} \left(\boldsymbol{\mathcal{G}}^{-1}_{0}(\vec{K}, \omega) - \boldsymbol{\Sigma}(\omega) \right)^{-1} \quad . \end{aligned} \tag{3.10}$$

As in DMFT, this is usually solved by iterating the equation

$$\boldsymbol{\Delta}_{\text{new}}(\omega) = \boldsymbol{\Delta}_{\text{old}}(\omega) + \boldsymbol{G}_{\text{cl}}^{-1}(\omega) - \boldsymbol{G}_{\text{loc}}^{-1}(\omega) \tag{3.11}$$

until a fixed point is reached. Note that by construction, CDMFT breaks translation invariance, which has to be reintroduced by post-processing the self-energy (see Sec. 3.3) after convergence.

3.2 Dynamical cluster approximation

The dynamical cluster approximation (DCA) [25, 26], in contrast to the CDMFT, is a cluster extension most easily viewed from a momentum-space perspective. While in DMFT, the Laue function $\Delta_{\text{Laue}}(\vec{k})$ is constant over the whole Brillouin zone, neglecting any momentum conservation at internal vertices, in the DCA, momentum conservation is partially reinstated. This is done by dividing the Brillouin zone into N_c patches with equal size (see Fig. 3.2) and neglecting momentum conservation within patches, but not between them. The corresponding Laue function then reads

$$\begin{gathered}\Delta_{\text{Laue}}(\vec{k}_1, \vec{k}_2, \vec{k}_3, \vec{k}_4) = N_c \delta_{\vec{K}_1 + \vec{K}_3, \vec{K}_2 + \vec{K}_4} \\ \vec{K}_i = \vec{K}(\vec{k}_i)\end{gathered} \tag{3.12}$$

where $\vec{K}(\vec{k})$ maps the momentum $\vec{k}$ onto a representative momentum $\vec{K}$ of the patch it is contained in, e.g. the mid-point momentum of the patch. As a result, the momenta within each patch can freely be summed over (see Fig. 3.2), rendering the LW functional dependent only on the Green's function averaged over the corresponding patches

$$\bar{G}(\vec{K}_i, \omega) = \int_{\mathcal{P}(\vec{K}_i)} \frac{\mathrm{d}\vec{k}}{\mathcal{V}_{\mathcal{P}}} G(\vec{k}, \omega) \quad , \tag{3.13}$$

where $\mathcal{P}(\vec{K}_i)$ denotes the patch in the Brillouin zone represented by $\vec{K}_i$ while $\mathcal{V}_{\mathcal{P}} = \int_{\mathcal{P}(\vec{K}_i)} \mathrm{d}\vec{k} = \frac{\mathcal{V}_{1.\text{BZ}}}{N_c}$ denotes its volume. Because the LW functional depends only on the patch averaged Green's function

$$\Phi_U[\boldsymbol{G}] \overset{\text{DCA}}{=} \Phi_U[\bar{\boldsymbol{G}}] \quad , \tag{3.14}$$

the self energy is constant over each patch.

$$\begin{gathered}\Sigma(\vec{k}, \omega) = \frac{\delta \Phi_U[\bar{\boldsymbol{G}}]}{\delta G(\vec{k}, \omega)} = \frac{\delta \Phi_U[\bar{\boldsymbol{G}}]}{\delta \bar{G}(\vec{K}(\vec{k}), \omega)} \frac{\delta \bar{G}(\vec{K}(\vec{k}), \omega)}{\delta G(\vec{k}, \omega)} = \Sigma(\vec{K}(\vec{k}), \omega) \\ \Sigma(\vec{K}(\vec{k}), \omega) = \Sigma_U[\bar{G}(\vec{K}(\vec{k}), \omega)] = \frac{1}{\mathcal{V}_{\mathcal{P}}} \frac{\delta \Phi_U[\bar{\boldsymbol{G}}]}{\delta \bar{G}(\vec{K}(\vec{k}), \omega)}\end{gathered} \tag{3.15}$$

The self-consistency equation Eq. (2.8) then gives

$$\bar{G}(\vec{K}, \omega) = \int_{\mathcal{P}(\vec{K})} \frac{\mathrm{d}\vec{k}}{\mathcal{V}_{\mathcal{P}}} \left(\mathcal{G}_0^{-1}(\vec{k}, \omega) - \Sigma_{\text{DCA}}[\bar{G}(\vec{K}, \omega)] \right)^{-1} \quad , \tag{3.16}$$

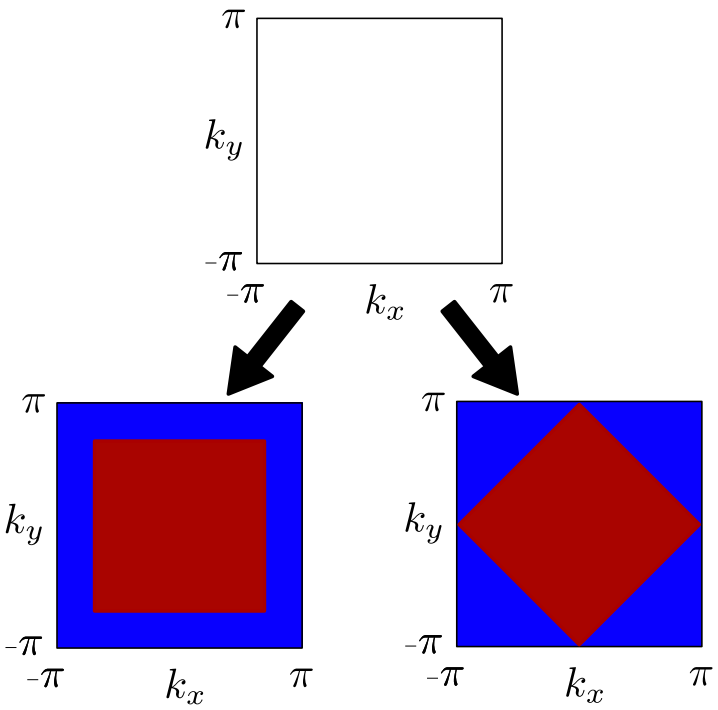

Figure 3.2: two possible patching schemes with $N_c = 2$ of a $d = 2$ square lattice Brillouin zone.

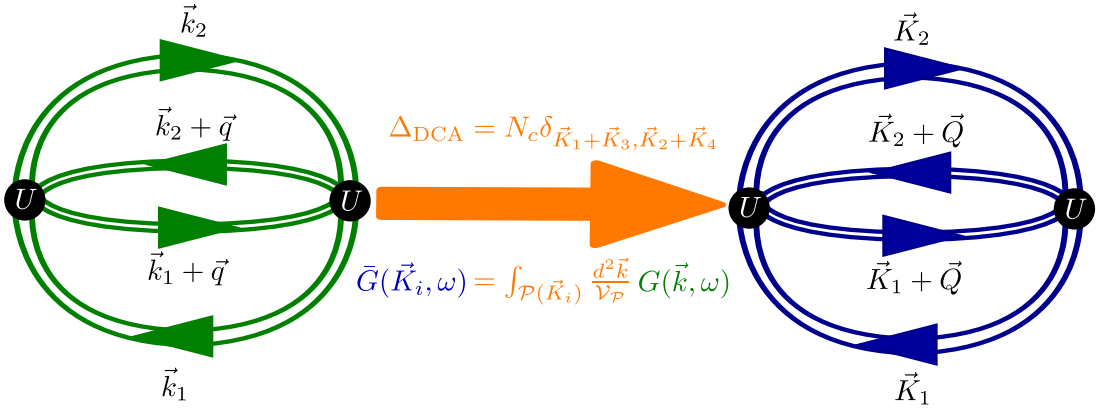

Figure 3.3: Simplification of the second-order term in the LW functional with the DCA approximation for the Laue function. Double lines denote full propagators, black dots interaction vertices.

which can be solved with the help of a N_c site cluster model. It is set up as a coarse grained version of the lattice model in momentum space:

$$\begin{aligned} H_{\text{latt}} &= \sum_{\vec{k},\sigma} (\epsilon(\vec{k}) - \mu) c^\dagger_{\vec{k},\sigma} c_{\vec{k},\sigma} + U \sum_{\vec{k}_1,\vec{k}_2,\vec{q}} c^\dagger_{\vec{k}_1+\vec{q},\uparrow} c^\dagger_{\vec{k}_2-\vec{q},\downarrow} c_{\vec{k}_2,\downarrow} c_{\vec{k}_1,\uparrow} \\ \epsilon(\vec{k}) &= -2t \sum_{\alpha=1}^{d} \cos(k_\alpha) \end{aligned} \tag{3.17}$$

$$\begin{aligned} H_c &= H_{cl} + H_{\text{bath}} + H_{\text{hyb}} \\ H_{cl} &= \sum_{i=1;\sigma}^{i=N_c} (\epsilon_{\vec{K}_i} - \mu) c^\dagger_{\vec{K}_i,\sigma} c_{\vec{K}_i,\sigma} + U \sum_{i,j,l=1}^{N_c} c^\dagger_{\vec{K}_i+\vec{Q}_l,\uparrow} c^\dagger_{\vec{K}_j-\vec{Q}_l,\downarrow} c_{\vec{K}_j,\downarrow} c_{\vec{K}_i,\uparrow} \\ \epsilon_{\vec{K}_i} &= \int_{\mathcal{P}(\vec{K}_i)} \frac{\mathrm{d}\vec{k}}{\mathcal{V}_{\mathcal{P}}} \epsilon(\vec{k}) \\ H_{\text{bath}} &= \sum_{(i,\lambda),\sigma} \epsilon_{(i,\lambda)} a^\dagger_{(i,\lambda),\sigma} a_{(i,\lambda),\sigma} \\ H_{\text{hyb}} &= \sum_{i,\lambda,\sigma} \left(V_{i,\lambda} a^\dagger_{(i,\lambda),\sigma} c_{i,\sigma} + h.c. \right) \end{aligned} \tag{3.18}$$

Solving the cluster model gives Σ_U evaluated at G_{cl}

$$\begin{aligned} \Sigma_{cl}(\vec{K}_i, \omega) &= \Sigma_{\text{DCA}}[G_{cl}(\vec{K}_i, \omega)] \\ G_{cl}(\vec{K}_i, \omega) &= \left(\omega - \epsilon_{\vec{K}_i} + \mu - \Delta(\vec{K}_i, \omega) - \Sigma_{cl}(\vec{K}_i, \omega) \right)^{-1} \end{aligned} \tag{3.19}$$

where the hybridization function

$$\Delta(\vec{K}_i, \omega) = \sum_{\lambda} \frac{|V_{i,\lambda}|^2}{\omega - \epsilon_{(i,\lambda)}} \tag{3.20}$$

has to be found such that

$$\begin{aligned} \bar{G}(\vec{K}_i, \omega) &\stackrel{!}{=} G_{cl}(\vec{K}_i, \omega) \\ \int_{\mathcal{P}(\vec{K}_i)} \frac{\mathrm{d}\vec{k}}{\mathcal{V}_{\vec{P}}} \left(\mathcal{G}_0^{-1}(\vec{k}, \omega) - \Sigma_{cl}(\vec{K}_i, \omega) \right)^{-1} &\stackrel{!}{=} \left(\mathcal{G}_0^{-1}(\vec{K}_i, \omega) - \Sigma_{cl}(\vec{K}_i, \omega) \right)^{-1} \end{aligned} \tag{3.21}$$

which is the DCA self-consistency condition. The self-consistent hybridization is, as in DMFT and CDMFT, usually found by iterating

$$\Delta_{\text{new}}(\vec{K}_i, \omega) = \Delta_{\text{old}}(\vec{K}_i, \omega) + G_{cl}^{-1}(\vec{K}_i, \omega) - \bar{G}^{-1}(\vec{K}_i, \omega) \tag{3.22}$$

until a fixed point is reached. Note that opposed to the CDMFT, DCA is translation invariant due to its momentum space formulation. On the other hand, the self-energy in DCA is discontinuous, jumping between momentum space patches. This requires post-processing to remove these jumps, which will be discussed in the next section.

3.3 Determination of continuous lattice self-energy

After self-consistency is reached, the self-energy both in CDMFT and DCA have to be post-processed. While the discontinuities of the DCA self-energy have to be cured by interpolation, the CDMFT self-energy has to be reperiodized. As long as these interpolation/reperiodization schemes preserve causality ($\mathrm{Im}(\Sigma(\vec{k},\omega)) \leq 0$), it is to some extent arbitrary and different methods have been put forward [27, 28]. The quality of the scheme also depends on the specific quantity which is used for interpolation/periodization. Apart from the self-energy itself, the cumulant [29, 30]

$$\boldsymbol{M}(\omega) = (\omega + \mu - \boldsymbol{\Sigma}(\omega))^{-1} \tag{3.23}$$

and the Green's function [31] have been used. As it seems that the cumulant usually gives good results [32, 29, 30] when compared to larger clusters or exact results, especially when correlations are strong, in this thesis M-interpolation/reperiodization has been applied throughout. For the two patch DCA calculations, trigonometric interpolation as in [32] was employed.

$$\begin{aligned} M(\vec{k},\omega) &= M_+(\omega)a_+(\vec{k}) + M_-(\omega)a_-(\vec{k}) \\ a_\pm(\vec{k}) &= \frac{1}{2}\left(1 \pm \frac{1}{d}\sum_{\alpha=1}^{d}\cos(k_\alpha)\right) \end{aligned} \tag{3.24}$$

Here, $+$ and $-$ denote the patch around $\Gamma = (0,...,0)$ (red patch in the middle in Fig. 3.2) and the one around $\Pi = (\pi,...,\pi)$ (blue one in Fig. 3.2), respectively. CDMFT, in contrast to the DCA, does not yield a discontinuous self-energy, but breaks translation invariance due to its construction. As a result, both the self-energy and the cumulant are not diagonal in $\vec{k}$-space but depend on two momenta

$$\begin{aligned} \Sigma(\omega,\vec{k}_1,\vec{k}_2) &= \frac{1}{N_c}\sum_{\vec{Q}}\sum_{i,j} e^{i\vec{k}_1\vec{x}_i}\Sigma_{i,j}(\omega)e^{-i\vec{k}_1\vec{x}_j}\delta_{\vec{k}_1-\vec{k}_2,\vec{Q}} \\ M(\omega,\vec{k}_1,\vec{k}_2) &= \frac{1}{N_c}\sum_{\vec{Q}}\sum_{i,j} e^{i\vec{k}_1\vec{x}_i}M_{i,j}(\omega)e^{-i\vec{k}_1\vec{x}_j}\delta_{\vec{k}_1-\vec{k}_2,\vec{Q}} \quad , \end{aligned} \tag{3.25}$$

where x_i are intra-cluster positions and $\vec{Q}$ are reciprocal lattice vectors of the super-lattice. To reperiodize the result, the $\vec{Q} = 0$ component is used either for Σ or M. After interpolating/periodizing the cumulant, the self-energy is given by

$$\Sigma(\vec{k},\omega) = \omega + \mu - M(\vec{k},\omega)^{-1} \quad . \tag{3.26}$$

It should be noted that the interpolated/reperiodized self-energies must not be used in the self-consistency equations, as this can lead to non-causal ($\mathrm{Im}(\Delta(\omega)) > 0$) mean fields.

3.4 Causality and other cluster extensions

Apart from CDMFT and DCA, one can think of constructing many different cluster methods. Notably, a periodic version of the CDMFT, the periodized CDMFT (PCDMFT) [33] and a version of the DCA with continuous self-energy, the DCA$^+$ [34, 35] have been developed. One

of the main issues of constructing new cluster extensions is that they have to preserve causality. Early attempts to construct a cluster extension [36], called the nested cluster scheme (NCS), failed to generate causal results for arbitrary parameter regimes [33, 37] (see also [38, 39]). While Biroli *et al.* [33], it was argued that causality should be preserved in NCS for $N_c \to \infty$, Vučičević *et al.* [37] found indications that NCS converges to a non-causal solution even in the $N_c \to \infty$ limit which they blamed on the recently discovered multivaluedness of the LW-functional [40, 41]. It should be noted here that NCS, if there is no causality violation, is expected to yield superior results to CDMFT and DCA at comparable cluster sizes [33, 37]. Unfortunately, during the work for this thesis, it was not possible to stabilize a causal solution with NCS + NRG for the $d = 2$ Hubbard model, even for quite low interactions.

4 Numerical Renormalization Group

To solve the cluster model, the numerical renormalization group (NRG) has been used. NRG has been developed by Wilson [42] to solve the Kondo problem and has over the years been improved into a powerful impurity solver [4]. The code used here has been developed by Andreas Weichselbaum and Seung-Sup Lee. In the following, the NRG procedure will shortly be summarized. The two impurity Anderson model (2IAM), on which all cluster calculations in this thesis are based on, will serve as an example.

4.1 Two impurity Anderson model

The 2IAM, described by the Hamiltonian

$$\begin{aligned} H_{\text{2IAM}} &= H_{\text{imp}} + H_{\text{bath}} + H_{\text{hyb}} \\ H_{\text{imp}} &= \sum_{\sigma;\alpha=1,2} (\epsilon_{d,\alpha} - \mu) d^\dagger_{\alpha,\sigma} d_{\alpha,\sigma} - t \sum_{\sigma} (d^\dagger_{1,\sigma} d_{2,\sigma} + h.c.) + H_{\text{int}} \\ H_{\text{int}} &= U \sum_{\alpha=1,2} n_{\alpha,\uparrow} n_{\alpha,\downarrow} \\ H_{\text{bath}} &= \sum_{\sigma;\alpha=1,2,\lambda} \epsilon_{\sigma,(\lambda,\alpha)} c^\dagger_{\sigma,(\lambda,\alpha)} c_{\sigma,(\lambda,\alpha)} \\ H_{\text{hyb}} &= \sum_{\sigma,\alpha,\beta,\lambda} (V^\sigma_{\alpha,(\beta,\lambda)} d^\dagger_{\alpha,\sigma} c_{\sigma,(\lambda,\beta)} + h.c.) \quad , \end{aligned} \tag{4.1}$$

consists of two impurity orbitals with annihilation operators $d_{\alpha,\sigma}$ and number operators $n_{\alpha,\sigma} = d^\dagger_{\alpha,\sigma} d_{\alpha,\sigma}$ coupled to an infinite bath, described by the annihilation operators $c_{\sigma,(\lambda,\alpha)}$. In the following, the two impurity orbitals and their spin directions will be assumed equivalent, which means that $\epsilon_{d,\alpha} = \epsilon_d$, $\epsilon_{\sigma,(\lambda,\alpha)} = \epsilon_\lambda$ and $V^\sigma_{\alpha,(\beta,\lambda)} = V_{\alpha,(\beta,\lambda)} = V_{\beta,(\alpha,\lambda)}$ with V purely real will be considered, as this was the case for all calculations in this thesis. Therefore, the hybridization

$$\Delta_{\alpha,\beta}(\omega) = \sum_{(\gamma,\lambda)} \frac{V_{\alpha,(\gamma,\lambda)} \bar{V}_{\beta,(\gamma,\lambda)}}{\omega - \epsilon_\lambda} \tag{4.2}$$

fulfills $\boldsymbol{\Delta}(\omega) = \boldsymbol{\Delta}^\top(\omega)$ and can thus be diagonalized independent of ω by

$$\boldsymbol{\mathcal{U}} = \frac{1}{\sqrt{2}} \begin{pmatrix} 1 & 1 \\ 1 & -1 \end{pmatrix} \quad . \tag{4.3}$$

Using a bonding/anti-bonding basis

$$\begin{aligned} c_{\sigma,(\lambda,\pm)} &= \frac{1}{\sqrt{2}} (c_{\sigma,(\lambda,1)} \pm c_{\sigma,(\lambda,2)}) \\ d_{\sigma,\pm} &= \frac{1}{\sqrt{2}} (d_{\sigma,1} \pm d_{\sigma,2}) \quad , \end{aligned} \tag{4.4}$$

the hybridization $\boldsymbol{\Delta}$, the Green's function $\boldsymbol{G}$ and thus also the self-energy $\boldsymbol{\Sigma}$ will be diagonal. The Hamiltonian in this basis then reads

$$\begin{aligned} H_{\text{2IAM}} &= H_{\text{imp}} + H_{\text{bath}} + H_{\text{hyb}} \\ H_{\text{imp}} &= \sum_{\sigma;\alpha=\pm} (\epsilon_{d,\alpha} - \mu \mp t) d^\dagger_{\alpha,\sigma} d_{\alpha,\sigma} + H_{\text{int}} \\ H_{\text{bath}} &= \sum_{\sigma;\alpha=\pm,\lambda} \epsilon_\lambda c^\dagger_{\sigma,(\lambda,\alpha)} c_{\sigma,(\lambda,\alpha)} \\ H_{\text{hyb}} &= \sum_{\sigma,\alpha=\pm,\lambda} (V_{\alpha,\lambda} d^\dagger_{\alpha,\sigma} c_{\sigma,(\lambda,\alpha)} + h.c.) \quad . \end{aligned} \tag{4.5}$$

As a consequence, bonding and anti-bonding are completely decoupled in the $U = 0$ case and mix only via H_{int}.

4.2 NRG procedure and calculation of observables

The hybridization density of states

$$\Gamma_\pm(\omega) = -\frac{1}{\pi}\text{Im}(\Delta_\pm(\omega)) = \sum_\lambda |V_{\pm,\lambda}|^2 \delta(\omega - \epsilon_\lambda) \tag{4.6}$$

has a finite band-with in the interval $[-D^<_\pm, D^>_\pm]$ with $D^{\lessgtr}_\pm > 0$. Now, a discretization parameter $\Lambda > 1$ is used to define a logarithmic grid with grid points at $\pm D^{\lessgtr}_\pm \cdot \Lambda^{-n}$ with $n = \{0, 1, 2, 3, ...\}$ integer and the bath is approximated by a single state in each interval $I^{\lessgtr}_{\pm,n} = \pm D^{\lessgtr}_\pm \cdot [\Lambda^{-n}, \Lambda^{-n-1}]$. The state chosen in each interval is the one directly coupling to the impurity orbitals

$$\begin{aligned} a_{\lessgtr,\sigma,\alpha,n} &= \sum_{\epsilon_\lambda \in I^{\lessgtr}_{\alpha,n}} \frac{V_{\alpha,\lambda}}{\gamma^{\lessgtr}_{\alpha,n}} c_{\sigma,(\lambda,\alpha)} \\ \gamma^{\lessgtr}_{\alpha,n} &= \sqrt{\sum_{\epsilon_\lambda \in I^{\lessgtr}_{\alpha,n}} |V_{\alpha,\lambda}|^2} \sim \Lambda^{-\frac{n}{2}} \quad , \end{aligned} \tag{4.7}$$

leaving H_{hyb} unchanged but approximating H_{bath} by

$$\begin{aligned} H_{\text{bath}} &= \sum_{n,\alpha,\sigma,\lessgtr} \xi^{\lessgtr}_{\alpha,n} a^\dagger_{\lessgtr,\sigma,\alpha,n} a_{\lessgtr,\sigma,\alpha,n} \\ \xi^{\lessgtr}_{\alpha,n} &= \sum_{\epsilon_\lambda \in I^{\lessgtr}_{\alpha,n}} \epsilon_\lambda \left(\frac{V_{\alpha,\lambda}}{\gamma^{\lessgtr}_{\alpha,n}}\right)^2 \sim \Lambda^{-n} \quad . \end{aligned} \tag{4.8}$$

The resulting discretized Hamiltonian

$$\begin{aligned} H_{\text{2IAM}} &= H_{\text{imp}} + H_{\text{bath}} + H_{\text{hyb}} \\ H_{\text{imp}} &= \sum_{\sigma;\alpha=\pm} (\epsilon_{d,\alpha} - \mu \mp t) d^\dagger_{\alpha,\sigma} d_{\alpha,\sigma} + H_{\text{int}} \\ H_{\text{bath}} &= \sum_{n,\alpha,\sigma,\lessgtr} \xi^{\lessgtr}_{\alpha,n} a^\dagger_{\lessgtr,\sigma,\alpha,n} a_{\lessgtr,\sigma,\alpha,n} \\ H_{\text{hyb}} &= \sum_{\sigma,\alpha,n,\lessgtr} (\gamma^{\lessgtr}_{\alpha,n} d^\dagger_{\alpha,\sigma} a_{\lessgtr,\sigma,\alpha,n} + h.c.) \end{aligned} \tag{4.9}$$

can then be mapped on a semi-infinite tight binding chain with the impurity at the beginning. This is done by tridiagonalization, using

$$\begin{aligned} f_{\sigma,0,\alpha} &= \sum_{\alpha,n,\lessgtr} \frac{\gamma^{\lessgtr}_{\alpha,n}}{t_{0,\alpha}} a_{\lessgtr,\sigma,\alpha,n} \\ t_{0,\alpha} &= \sqrt{\sum_{\alpha,n,\lessgtr} |\gamma^{\lessgtr}_{\alpha,n}|^2} \end{aligned} \tag{4.10}$$

as the seed state, which leads to the so called Wilson chain Hamiltonian.

$$\begin{aligned} H &= H_{\text{imp}} + H_{\text{chain}} \\ H_{\text{chain}} &= \sum_{\sigma,\alpha} \{ g_{0,\alpha} f^\dagger_{\sigma,0,\alpha} f_{\sigma,0,\alpha} + (t_{0,\alpha} d^\dagger_{\sigma,\alpha} f_{\sigma,0,\alpha} + h.c.) \} + \sum_{n=1}^{\infty} h_n \\ h_n &= \sum_{\sigma,\alpha} \{ g_{n,\alpha} f^\dagger_{\sigma,n,\alpha} f_{\sigma,n,\alpha} + (t_{n,\alpha} f^\dagger_{\sigma,n,\alpha} f_{\sigma,n-1,\alpha} + h.c.) \} \end{aligned} \tag{4.11}$$

It comes with a exponentially decreasing energy scale at the chain site n, inherited from the logarithmic discretization.

$$\begin{aligned} t_{n,\alpha} &\sim \Lambda^{-\frac{n}{2}} \\ g_{n,\alpha} &\sim \Lambda^{-n} \end{aligned} \tag{4.12}$$

Due to the energy scale separation between site n and $n+1$, the Wilson chain can be diagonalized iteratively in a renormalization group like procedure, starting from large energy scales and zooming in on ever smaller scales. To do this, consider the Hamiltonian up to site N,

$$\tilde{H}_N = H_{\text{imp}} + \sum_{\sigma,\alpha} \{ g_{0,\alpha} f^\dagger_{\sigma,0,\alpha} f_{\sigma,0,\alpha} + (t_{0,\alpha} d^\dagger_{\sigma,\alpha} f_{\sigma,0,\alpha} + h.c.) \} + \sum_{n=1}^{N} h_n \quad , \tag{4.13}$$

whose lowest energy scale is of order $\sim \Lambda^{-\frac{N}{2}}$. To zoom into the low energy spectrum, we define

$$H_N = \Lambda^{\frac{N}{2}} \tilde{H}_N \quad , \tag{4.14}$$

whose lowest energy scale is of order 1, which allows for a resolution of the lowest energy scales with a numerical accuracy independent of N. The problem is of course that H_N cannot be diagonalized exactly for large N, due to the exponentially increasing Hilbert space dimension. As h_{N+1} is a pertubation of order $\Lambda^{-\frac{1}{2}}$ with respect to H_N, we expect that the low energy physics of H_{N+1} can be accurately described starting from the lowest eigenstates of H_N. This motivates the following procedure to go from N to $N+1$:

1. take the lowest N_{keep} eigenstates $\{|m\rangle_N\}$ of H_N with eigenenergies $E_N(m)$. The ground state energy is set to 0.

2. add the basis $\{|s\rangle_{N+1}\}$ of the $N+1$ site to the $\{|m\rangle_N\}$ to get the basis $\{|n\rangle_{N+1}\} = \{|m\rangle_N \otimes |s\rangle_{N+1}\}$. Represent the Hamiltonian

$$H_{N+1} = \Lambda^{\frac{1}{2}} [H_N + \Lambda^{\frac{N}{2}} h_{N+1}] \tag{4.15}$$

in the subspace spanned by this basis.

3. diagonalize H_{N+1} on this subspace to obtain the lowest $16 \cdot N_{\text{keep}}$ eigenstates $\{|m\rangle_{N+1}\}$ of H_{N+1}.

The above procedure is initialized by the exact diagonalization of H_0 and iterated until the desired energy resolution of order $\Lambda^{-\frac{N}{2}}$ is reached. Conducting the iterative not only allows to diagonalize the impurity Hamiltonian up to a certain energy resolution, but also gives a renormalization group flow of the lowest energy levels, allowing to analyze the behavior of the impurity model at different energy scales [43]. In the following, some technical improvements, allowing the accurate calculation of observables at arbitrary temperatures and reducing the computational complexity, are shortly listed.

Complete many-body basis and full density matrix
From the truncated states at each iteration, a complete set of approximate eigenstates of the Wilson chain can be constructed [44]. These can be used to construct the full density matrix (fdmNRG) and allows the calculation of real-frequency dynamical response functions via their spectral representation [45].

Exploiting symmetries and matrix product states
The NRG can be efficiently formulated using matrix product states (MPS) [46]. With the implementation of the QSpace tensor network library [47], this allows to exploit abelian and non-abelian symmetries of the Hamiltonian, considerably reducing computational effort.

Z-averaging
The resolution of NRG, especially at large energies, can be enhanced by performing multiple calculations with shifted grid (z-shifting) [48, 49] and averaging over them. Analyzing the behavior of the Wilson chain on z-shifting, improved methods to determine the Wilson chain parameters [50, 51] can be obtained.

Adaptive broadening
By analyzing how discrete spectral weight behaves when shifting the grid, it can be inferred whether features are physical or not. This allows to adapt the broadening width accordingly, which results in improved resolution of dynamical correlation functions at finite frequencies [52].

Interleaved NRG (iNRG)
By shifting the grids of different orbitals relative to each other, energy scale separation between orbitals along the chain can be generated. This allows to truncate between orbitals [53, 54], reducing computational effort. It should be noted that this procedure treats different orbitals on a different footing, in particular, it artificially breaks symmetries between orbitals, if present. For the 2IAM, it is therefore important to interleave in the bonding/anti-bonding basis and not in the real-space basis.

5 Brillouin-zone integration

To implement the iterative procedures for finding the self-consistent mean-field in the CDMFT and the DCA, respectively, a momentum-space integral of the Green's function has to performed. Generically, this has to be done numerically. When using NRG to solve the cluster model, the self-consistency is conducted on the real-frequency axis and often calculations are done at very low temperatures. As the Green's function has its poles on the real-frequency axis, it becomes an extremely sharply peaked function of $\vec{k}$ for a fixed value of ω, especially at low temperatures and frequencies. This renders the integration intractable for standard routines. In this thesis, 6402 frequency grid points with exponential resolution towards $\omega = 0$ have been used, leaving at most a few seconds per frequency point to perform the integration to the desired precision before becoming impractical. To solve this, the tetrahedron method [55, 56, 57] with an adaptive $\vec{k}$ grid which can meet accuracy and speed demands, has been implemented.

5.1 Tetrahedron method - general procedure

The tetrahedron method has been developed to tackle integrals of the form

$$I = \int_{1.\mathrm{BZ}} \mathrm{d}\vec{k} A(\vec{k}) B(\epsilon(\vec{k})) \quad , \tag{5.1}$$

where $A(\vec{k})$ is an arbitrary, smooth function of $\vec{k}$, $\epsilon(\vec{k})$ is the dispersion, also assumed smooth, while B may be some discontinuous or peaked function. For the integration of Green's functions [58, 59, 60] we are specifically interested in the case $B(\epsilon(\vec{k})) = \frac{1}{a+b\epsilon(\vec{k})}$, where a and b are complex valued constants. The generic form of the integrand I will from now on assume is

$$I = \int_{1.\mathrm{BZ}} \mathrm{d}\vec{k} \frac{f(\vec{k})}{g(\vec{k})} \quad , \tag{5.2}$$

where both f and g are smooth functions, such that low order polynomial interpolation is applicable over small areas. In the tetrahedron method, the Brillouin-zone is tiled into a mesh of tetrahedra (see Fig. 5.1). Both f and g are then interpolated linearly over each tetrahedron. The integral over each tetrahedron

$$I_n = 6V_T \int_0^1 \mathrm{d}x \int_0^{1-x} \mathrm{d}y \int_0^{1-x-y} \mathrm{d}z \frac{f_1 + f_{2,1}x + f_{3,1}y + f_{4,1}z}{g_1 + g_{2,1}x + g_{3,1}y + g_{4,1}z} \tag{5.3}$$

is then evaluated analytically. Here, $f_i = f(\vec{k}_i)$ is the function f evaluated at the 4 corner points of the tetrahedron, $f_{i,j} = f_i - f_j$ are the differences between the corner values, V_T the volume of the tetrahedron and n denotes its number in some arbitrarily chosen enumeration of tetrahedra in the tiling. I_n can then be written as

$$I_n = \sum_{i=1}^{4} f_i w_i(\{g_j\}) \quad , \tag{5.4}$$

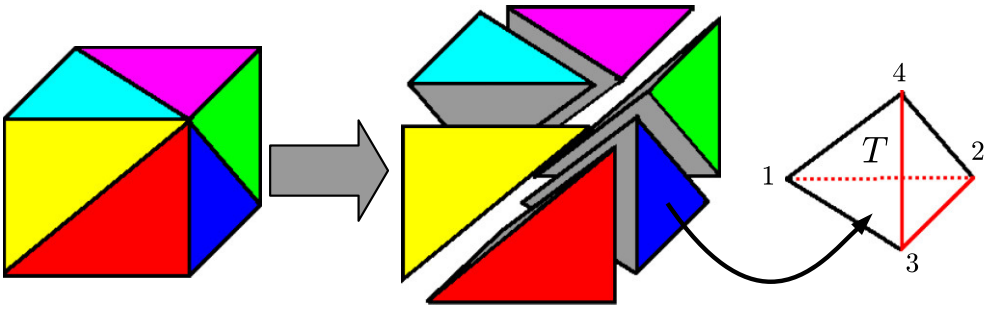

Figure 5.1: Partition of a cube into 6 tetrahedra. Figure taken from [61].

where w_i is a weight function depending only on the g_j. The total integral is then obtained by summing over all tetrahedra

$$I = \sum_n I_n \quad . \tag{5.5}$$

As the expressions for w_i are quite lengthy and are given in a practical formulation, handling degeneracies of the g_i, elsewhere [62], they are not repeated in this thesis. The method of course also works for $d = 2$ and $d = 1$ with triangles and lines instead of tetrahedra, respectively.

5.2 Integration of matrix valued Green's functions

When using the CDMFT, the Green's function, breaking translation invariance, ultimately becomes a matrix valued function of the super-lattice momentum $\vec{K}$. We are usually given the inverse Green's function $\boldsymbol{G}^{-1}(\vec{K},\omega)$ which is a smooth matrix valued function of $\vec{K}$ at a fixed ω. To integrate the matrix Green's function with the tetrahedron method [63], $\boldsymbol{G}^{-1}(\vec{K},\omega)$ is diagonalized

$$\boldsymbol{G}^{-1}(\vec{K},\omega) = \boldsymbol{U}(\vec{K},\omega)\boldsymbol{D}(\vec{K},\omega)\boldsymbol{U}^{-1}(\vec{K},\omega) \tag{5.6}$$

at every $\vec{K}$-grid point, where $\boldsymbol{D}(\vec{K},\omega)$ is a diagonal matrix. The integral can then be evaluated with the tetrahedron method by writing it as

$$I_{i,j}(\omega) = \int_{1.\mathrm{BZ}} \mathrm{d}\vec{K} G_{i,j}(\vec{K},\omega) = \sum_\alpha \int_{1.\mathrm{BZ}} \mathrm{d}\vec{K} \frac{U_{i,\alpha}(\vec{K},\omega)\cdot(U^{-1})_{\alpha,j}(\vec{K},\omega)}{D_\alpha(\vec{K},\omega)} \quad , \tag{5.7}$$

which has the same form as Eq. (5.2). As the diagonalization is done numerically, one has to make sure that the α-th eigenvalue $D_\alpha(\vec{K}_i,\omega)$ at grid point $\vec{K}_i$ is adiabatically connected to the α-th eigenvalues at the neighboring grid points. In this thesis, this has been done in the following way at a certain grid point $\vec{K}_i$:

1. take $\boldsymbol{U}(\vec{K}_j,\omega)$ at a neighboring grid-point, where the diagonalization has already been done
2. calculate $\tilde{\boldsymbol{D}}(\vec{K}_i,\omega) = \boldsymbol{U}^{-1}(\vec{K}_j,\omega)\boldsymbol{G}^{-1}(\vec{K}_i,\omega)\boldsymbol{U}(\vec{K}_j,\omega)$, where $\tilde{\boldsymbol{D}}(\vec{K}_i,\omega)$ is now almost diagonal
3. diagonalize $\tilde{\boldsymbol{D}}(\vec{K}_i,\omega) = \tilde{\boldsymbol{U}}(\vec{K}_i,\omega)\boldsymbol{D}(\vec{K}_i,\omega)\tilde{\boldsymbol{U}}^{-1}(\vec{K}_i,\omega)$ and sort the eigenvalues such that $\tilde{\boldsymbol{U}}(\vec{K}_i,\omega)$ is as close to $\mathbb{1}$ as possible

4. $\boldsymbol{U}(\vec{K}_i, \omega) = \boldsymbol{U}(\vec{K}_j, \omega)\tilde{\boldsymbol{U}}(\vec{K}_i, \omega)$

The scheme is initialized at an arbitrary grid-point where $\boldsymbol{G}^{-1}$ is just diagonalized normally.

5.3 Adaptive $\vec{k}$-grid

To increase speed, an adaptive grid has been implemented such that the grid-point density is chosen region dependent in $\vec{k}$-space according to accuracy demands. In the beginning, some desired total integration error ε is chosen and the integration area is divided into $(N_k - 1)^d$ cubes by choosing N_k evenly spaced grid points per dimension. Then, the error is estimated and the grid fine-grained in the following way (see Fig. 5.3):

1. every cube is divided into m_k^d finer cubes
2. the integral is solved on the coarse cubes and the fine ones
3. if $|I_{\text{coarse}} - I_{\text{fine}}| \leq \varepsilon$, the integral is considered converged
4. otherwise, all cubes with $|I_{n,\text{coarse}} - I_{n,\text{fine}}| \leq \varepsilon \frac{\mathcal{V}_c}{\mathcal{V}}$, where $\mathcal{V}$ is the volume of the total integration area while $\mathcal{V}_c$ is the volume of the coarse cube, are considered converged. For all other cubes, the m_k^d fine cubes are now considered coarse cubes. This is iterated until the integral is converged.

To test the efficiency of the adaptive grid, it was tested against a non-adaptive grid fine enough to yield the same integration error. For the test, the ϵ-point where the integration was hardest in the accuracy tests in section 5.4 was used. The test showed a 20-fold speedup in $d = 1$ and a 140-fold speedup in $d = 2$. For $d = 3$, the integration was not doable without an adaptive grid. It seems therefore that the use of an adaptive $\vec{k}$-grid is absolutely crucial for the tetrahedron method to be practical.

5.4 Accuracy tests

To test the accuracy of the integration routines, the non-interacting local Green's function of a cubic lattice in $d = \{1, 2, 3\}$ with nearest neighbor hopping is calculated both numerically and analytically. The total band-width is set to 1 so the dispersion is given by

$$\epsilon(\vec{k}) = -\frac{1}{2d} \sum_{\alpha=1}^{d} \cos(k_\alpha) \quad . \tag{5.8}$$

For general complex arguments, the local Green's function is given by the d dimensional integral

$$\mathcal{G}_{0,\text{loc}}(z) = \int_{-\pi}^{\pi} \frac{\mathrm{d}\vec{k}}{(2\pi)^d} \frac{1}{z - \epsilon(\vec{k})} \quad . \tag{5.9}$$

Numerically, the integral was evaluated for $z = \epsilon + i\eta$ slightly above the real axis

$$\mathcal{G}_0(\epsilon) = \mathcal{G}_{0,\text{loc}}(\epsilon + i\eta) \quad . \tag{5.10}$$

where η is a small regulator.

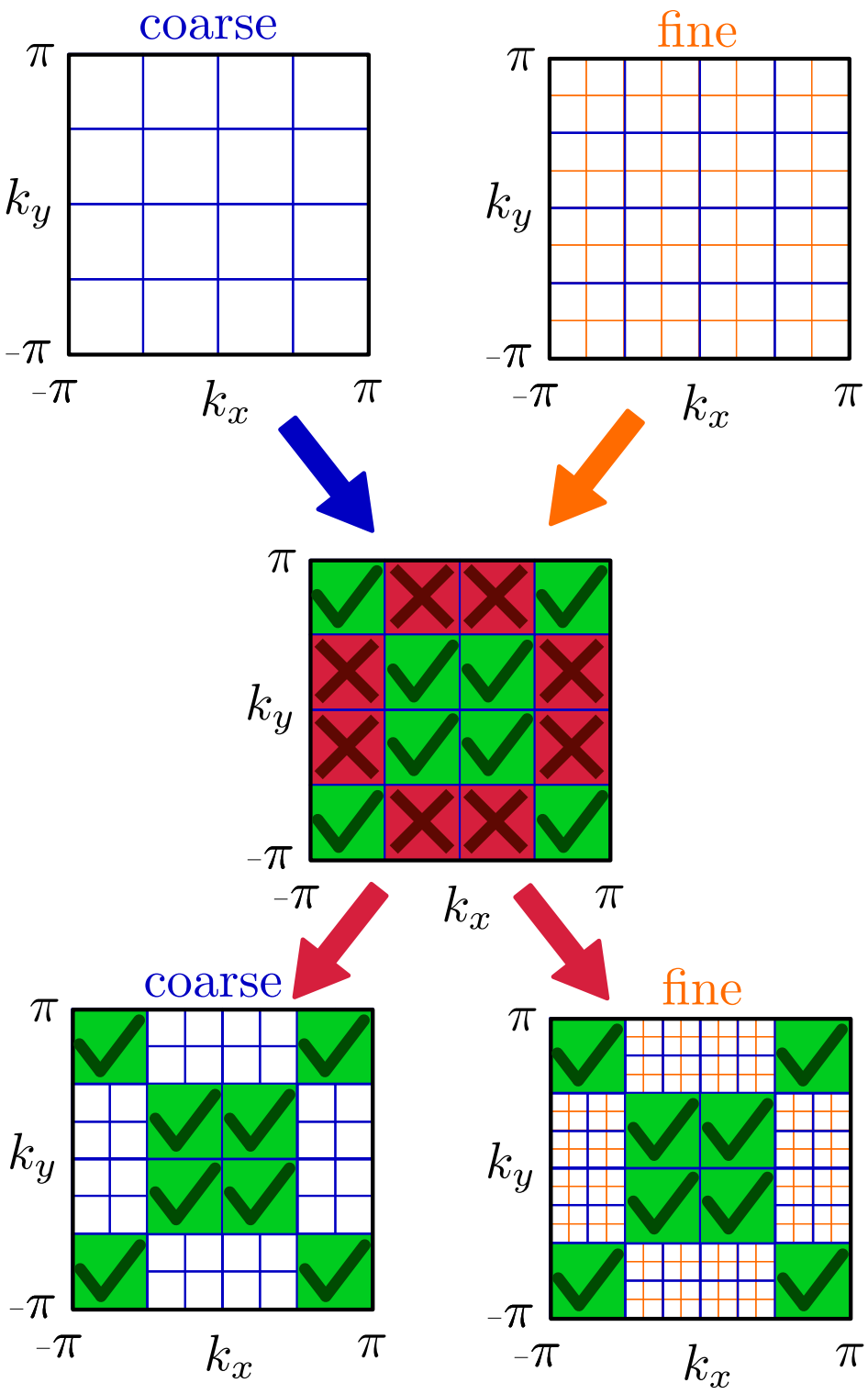

Figure 5.2: Schematic illustration of the adaptive grid in $d = 2$ with $N_k = 5$ and $m_k = 2$. First, the integral is performed on both the coarse and the fine grid. Then, the result is compared. If the error is too large, the part is fine-grained, otherwise, it is taken as converged. This is repeated until the integral is converged on the whole area.

Analytically, the integral for $\mathcal{G}_{0,\mathrm{loc}}(z)$ can be evaluated exactly for $d = \{1, 2, 3\}$ with the formulas:

1. in $d = 1$, a straight forward calculation gives

$$\begin{aligned} \mathcal{G}^{1d}_{0,\mathrm{loc}}(z) &= \frac{\mathrm{sgn}(|z_1| - 1)}{\sqrt{z^2 - \frac{1}{4}}} \\ z_1 &= 2\left(z + \sqrt{z^2 - \frac{1}{4}}\right) \end{aligned} \tag{5.11}$$

2. in $d = 2$, the integral is given by [64]

$$\begin{aligned} \mathcal{G}^{2d}_{0,\mathrm{loc}}(z) &= \frac{2}{\pi z} K\left(\frac{1}{2z}\right) \\ K(x) &= \int_0^{\frac{\pi}{2}} \mathrm{d}\theta \frac{1}{\sqrt{1 - x^2 \sin^2(\theta)}} \end{aligned} \tag{5.12}$$

   where $K(x)$ is the complete elliptic integral of the first kind.

3. in $d = 3$, it is given by [65]

$$\begin{aligned} \mathcal{G}^{3d}_{0,\mathrm{loc}}(z) &= \frac{1}{z} \frac{\sqrt{1 - \frac{3}{4}x_1}}{1 - x_1} \left[\frac{2}{\pi} K(k_+)\right] \left[\frac{2}{\pi} K(k_-)\right] \\ k^2_\pm &= \frac{1}{2} \pm \frac{1}{4} x_2 \sqrt{4 - x_2} - \frac{1}{4}(2 - x_2)\sqrt{1 - x_2} \\ x_1 &= \frac{1}{2} + \frac{1}{24 \cdot z^2} - \frac{1}{2}\sqrt{1 - \frac{1}{4 \cdot z^2}}\sqrt{1 - \frac{1}{36 \cdot z^2}} \\ x_2 &= \frac{x_1}{x_1 - 1} \end{aligned} \tag{5.13}$$

   where $K(x)$ again is the complete elliptic integral of the first kind.

The numerical calculations were done on 202 grid points evenly spaced between -1.005 and 1.005. For the $d = 1, 2$, the regulator was chosen $\eta = 10^{-10}$ while for $d = 3$, $\eta = 10^{-4}$ was used to reduce computational complexity at the kinks in $\mathcal{G}^{3d}_0(\epsilon)$ at $\sim \pm 0.2$. Results are shown in Fig. 5.4. It should be noted that in interacting calculation, the self-energy naturally introduces an imaginary part in the denominator, which usually renders the integration easier than in the non-interacting case demonstrated here. For all calculations, the integration error was chosen $\varepsilon = 10^{-3}$ and for the fine-graining of the grid, $m_k = 2$ was chosen. The actual errors and integration times, together with the average number of the maximum of 12 cores are given in the following table.

	maximum total error	maximum relative error	integration time in seconds	average number of cores
$d = 1$	$6.2 \cdot 10^{-4}$	$2.5 \cdot 10^{-4}$	0.25	9.6
$d = 2$	$4.5 \cdot 10^{-4}$	$1 \cdot 10^{-4}$	3.4	11
$d = 3$	$1.1 \cdot 10^{-3}$	$3 \cdot 10^{-4}$	93	9

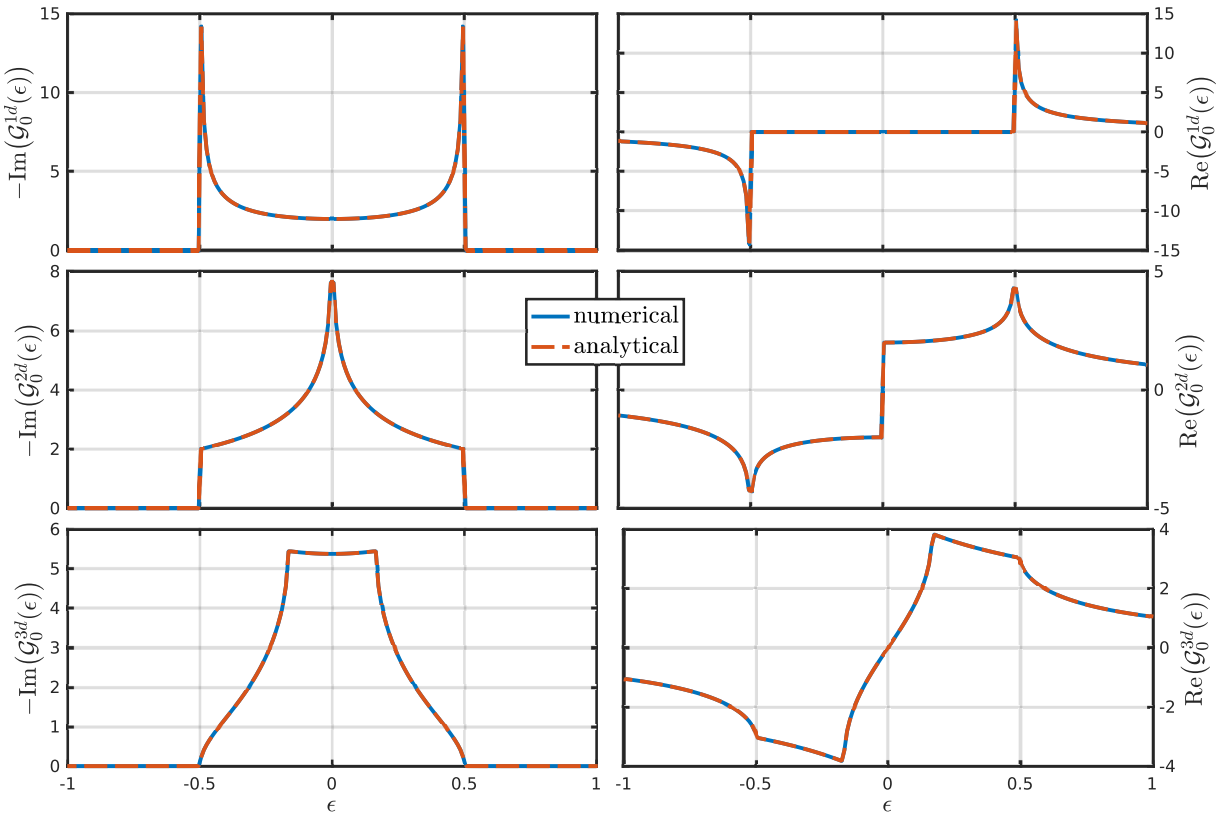

Figure 5.3: Comparison of analytical and numerical result for the local Green's function on a d-dimensional cubic lattice.

In $d = 1, 2$, the error is well below the set error bound, while the total error for $d = 3$ is 10% above the error bound. It should be noted though that the relative error is still well below 10^{-3}, the integration thus seems to be accurate enough to be practical. While in the presented case, the integration time is reasonable for all dimensions, it should be said here that most of the time is spent around the kinks and singularities in the Green's function. In DMFT+NRG calculations, this can lead to problems if these areas are around $\epsilon = 0$ as the grid is exponentially fine there.

6 Pseudogap in the Hubbard model

In this chapter, the Hubbard model in two dimensions using two-site dynamical cluster approximation will be discussed. The results shown here will serve as a benchmark for the cluster extensions + NRG method as high quality results [32], calculated with continuous time quantum monte carlo (CTQMC) [66], are available. All discussions will thereby be based on extracts of [32], and for more information, the original work is to be referred to.

6.1 Motivation

The two dimensional Hubbard model is thought to be a model capable of at least a qualitative description of cuprate superconductors [67]. These materials show quite a rich phase diagram in the doping versus temperature plane. Particularly interesting is the so called pseudogap (PG) phase, which develops at low to intermediate doping (underdoped) below a temperature $T^\star$ but above the superconducting transition temperature T_c. It is characterized by a suppression of spectral weight at the chemical potential [68]. Angle resolved photoemission spectroscopy (ARPES) measurements of the Fermi-surface [69, 70] show that a gap opens at the anti-nodal points $(0, \pi)$, leading to the formation of Fermi-arcs instead of a closed Fermi-surface. As this

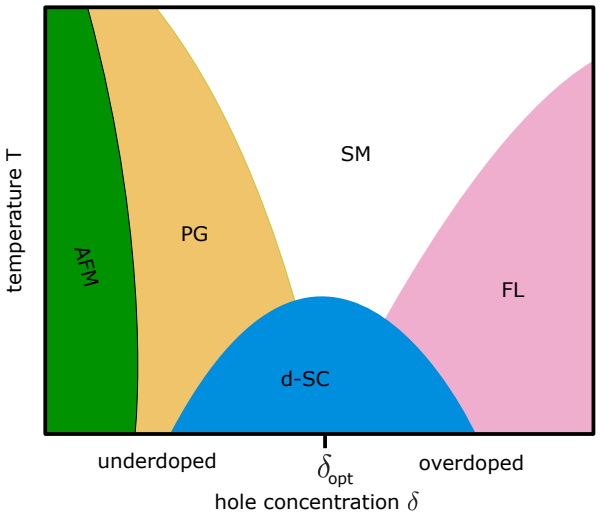

Figure 6.1: Schematic phase diagram of hole-doped cuprates. Near the Mott-insulator at $\delta = 0$, these materials typically show antiferromagnetism (AFM). When the hole concentration is increased, a pseudogap (PG) phase is observed above T_c, while at low temperatures, d-wave superconductivity (d-SC) develops in a dome shaped region. The largest critical temperature is reached for an optimal concentration δ_{opt}, which divides the phase diagram into a so called underdoped and an overdoped region. Raising the temperature at δ_{opt} above T_c, one enters a strange metal (SM) phase, which crosses over to a conventional Fermi-liquid (FL) deep in the overdoped region.

kind of momentum-space differentiation cannot be described by single-site DMFT, Ferrero *et al.* [32] studied the PG phase in a two-patch DCA setup, which turned out to be already capable of capturing the phenomena qualitatively. In the following, some these results will be reproduced for benchmark purposes. As it is possible with NRG to go to much lower temperatures than with QMC, this has also been considered. However, no qualitative difference from the high temperature results could have been made out. Therefore they are not shown here.

6.2 Technical details

In this chapter, the Hubbard model on a square lattice

$$\begin{aligned} H &= \sum_{\vec{k},\sigma} \epsilon_{\vec{k}} c^{\dagger}_{\vec{k},\sigma} c_{\vec{k},\sigma} + U \sum_{i} n_{i,\uparrow} n_{i,\downarrow} \\ \epsilon_{\vec{k}} &= -2t \left(\cos(k_x) + \cos(k_y)\right) - 4t' \cos(k_x)\cos(k_y) \end{aligned} \tag{6.1}$$

with nearest (t) and next nearest (t') neighbor hopping is considered. As in [32], $U/t = 10$ and $t'/t = -0.3$ are chosen, which are typical for modeling cuprates. As an energy scale, $D = 4t = 1$ is used and all calculations were done at a temperature $T = \frac{1}{200}$. Any possible symmetry breaking was suppressed in the calculations. As a tuning parameter the hole concentration δ is used.

In the DCA, the freedom to choose the shape of the patches is exploited by choosing the patches such that one (P_+) encloses the nodal region while the other one encloses the anti-nodal region (P_-).The patching and the corresponding densities of states are shown in Fig. 6.2.It is motivated by the formation of Fermi arcs in these materials, which suggests that at low doping, spectral weight will accumulate in the nodal region while the anti-nodal region will be gapped,

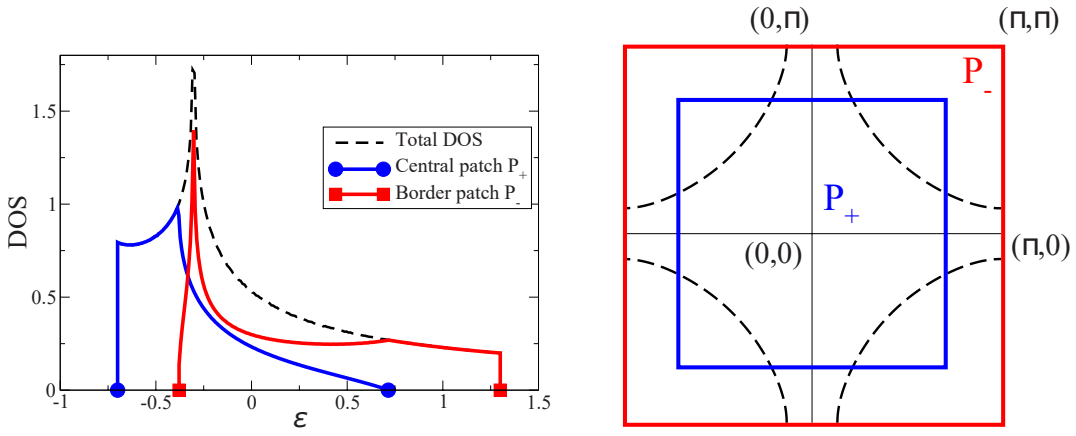

Figure 6.2: Patching of the Brillouin zone and corresponding densities of states. The dashed line denotes the non-interacting ($U = 0$) Fermi surface at $\delta = 0.1$. From ARPES experiments, it is expected that the anti-nodal patch (P_-) will be gapped while the nodal one (P_+) will be metallic. Note that the van Hove singularity is contained in P_- and is directly at its lower band-edge. The pseudogap phase will appear when the system is hole-doped towards the van Hove singularity. Figure adapted from [32].

leading to a pseudogap in the local spectral function.

The cluster model is set up as in Eq. (3.18), with $N_c = 2$. As $\epsilon(\vec{k})$ is mostly negative in the nodal patch, the cluster on-site energy $\epsilon_+ = -\epsilon_-$ for the nodal patch will be negative, while for the anti-nodal patch it is positive. The self-consistency procedure is done as explained already in chapter 3.

Because no symmetry between + and − states can be exploited, we interleave them in the iNRG. As parameters for the NRG, $\Lambda = 3$ was used to discretize the bath, $N_{\text{keep}} = 10000$ $SU(2)$ spin multiplets where kept and $n_z = 2$ z-shifts were performed.

6.3 DCA: Comparison to quantum monte carlo

We start the presentation of the NRG results and its comparison to the CTQMC results from [32] by looking at the spectral functions of the even and odd patches as a function of doping, shown in Fig. 6.3. For the anti-nodal patch, we see that with NRG, $A_-(\omega)$ develops a gap below the doping $\delta_c = 0.16$. Further, a sharp central peak is visible which is centered at $\omega = 0$ at $\delta = 0.2$ and moves to positive frequencies below $\delta_c = 0.16$, giving way to the gap. This gap becomes broader with smaller doping, while the peak moves away from $\omega = 0$ to ever larger positive frequencies. It should be noted that this peak is due to the van Hove singularity present in the anti-nodal patch.

Generally, CTQMC produces qualitatively similar results, though the exact values differ. Note however that for CTQMC, no true gap develops, but rather only a pseudogap. Also, the overall height and sharpness of the central peak is much lower, especially at large doping. Nevertheless, the critical doping, at which the central peak becomes centered at $\omega = 0$, is the same for both methods.

The spectral function for the nodal patch, $A_+(\omega)$, on the other hand, remains metallic for all doping levels shown in Fig. 6.3. Its total spectral weight at $\omega = 0$ increases quite considerably for the NRG result, while in CTQMC, this is more marginal. Also for CTQMC, the peak at negative energies, shown in the inset, reduces in height with increased doping and moves towards $\omega = 0$. For NRG, the total peak height roughly stays the same when doping is increased, though it also moves towards $\omega = 0$. Still, both methods produce qualitatively very similar results.

All in all, the behavior of the spectral function in the nodal and anti-nodal regions show that below a critical doping $\delta_c \simeq 0.16$, a pseudogap develops in the local spectral function $0.5 \cdot (A_+(\omega) + A_-(\omega))$, due to the gap opening in the anti-nodal patch. This also means that there are no coherent quasiparticles in the anti-nodal region below δ_c. This is also observed in ARPES experiments [70], where spectral weight, for low hole doping, starts to develop in the nodal region first, finally spreading from there to the anti-nodal region when doping is increased.

We will now have a look at the real-part of the self-energy at $\omega = 0$, which will provide us with a mechanism for the gap formation in the nodal patch, discussed above. $\text{Re}\Sigma_\pm(0)$ is shown as a function of doping in Fig. 6.4. Note that the CTQMC in the right panel of Fig. 6.4 are given by the diamonds only, while the solid line was obtained obtained via slave boson methods and are presented and discussed in the same reference [32] the CTQMC results are taken from. For the shown NRG results, the solid line is a guide to the eye, connecting the data points denoted by diamonds. First of all, we see that the CTQMC and NRG results are quite similar and almost

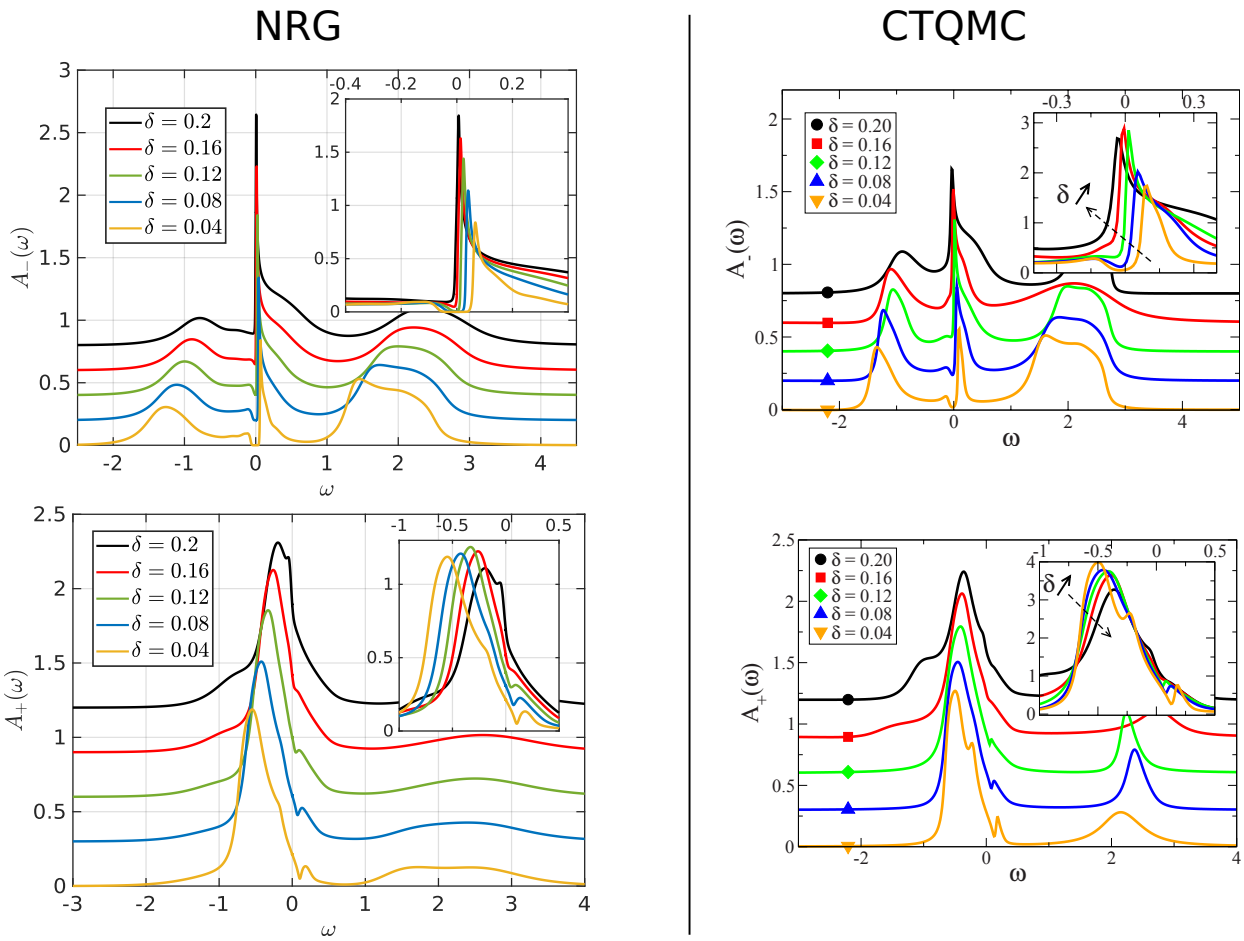

Figure 6.3: Spectral functions for the anti-nodal (upper panels) and the nodal (lower panel) patches. The left panels show the NRG results produced for this thesis, while the panels on the right show the CTQMC results, published by Ferrero *et al.* in [32] (Fig. 7 and 9). In the main panels, a vertical shift of 0.2 for the anti-nodal spectral functions and of 0.3 for the nodal ones has been added. The inset shows a zoom into the region around $\omega = 0$, without any vertical shift. Note that the y-scale for the insets of the CTQMC results is off when compared to the scale of the main plot. Presumably, in the insets a factor of $\frac{1}{pi}$ is missing.

match quantitatively. We see that at large doping, the self-energies at $\omega = 0$ for the nodal and anti-nodal patches are almost the same, indicating that single-site DMFT should produce quite accurate results there. As the doping is lowered, $\mathrm{Re}\Sigma_+(0)$ remains almost constant, while $\mathrm{Re}\Sigma_-(0)$ significantly increases, which pushes $\mu - \mathrm{Re}\Sigma_-(0)$ below the lower non-interacting band edge of the anti-nodal patch at $\epsilon_{\mathrm{min}} = -0.38$. This means that the $\vec{k}$-dependent Green's function for the anti-nodal patch has no poles at $\omega = 0$, rendering it gapped. As the doping is lowered, the $\mu - \mathrm{Re}\Sigma_-(0)$ becomes ever smaller, which increases the size of the gap.

The doping dependence of the anti-nodal gap is shown in Fig. 6.5, where Δ is the energy of the lowest positive energy poles in the anti-nodal Green's function, calculated via

$$\Delta + \mu - \epsilon_{\mathrm{min}} - \mathrm{Re}(\Sigma_-(\Delta)) \stackrel{!}{=} 0 \quad , \tag{6.2}$$

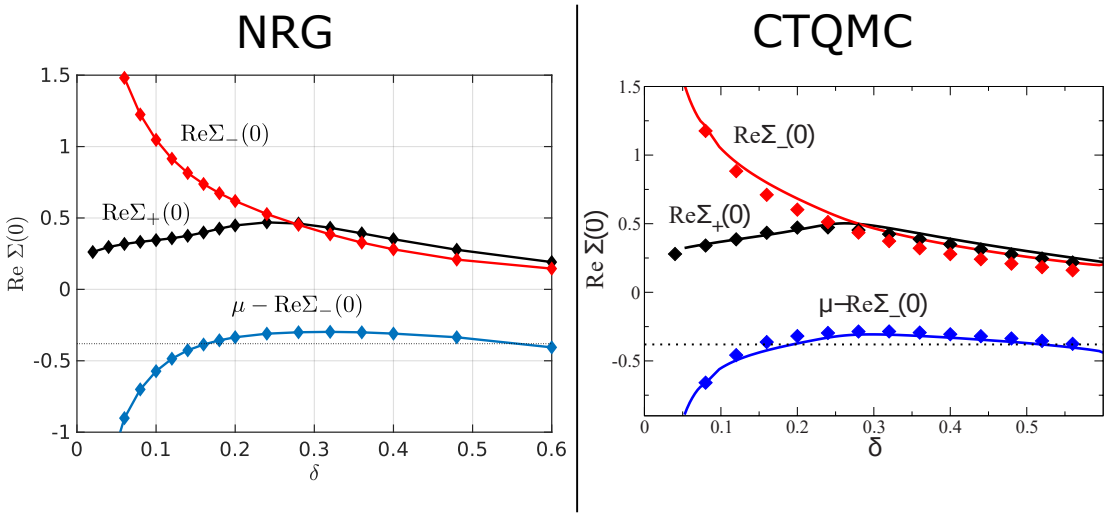

Figure 6.4: Doping dependence of the self-energy at $\omega = 0$. The results on the left were produced with NRG during this thesis, the diamonds denote data points while the lines are guides to the eye. On the right, results obtained from CTQMC (diamonds) and the slave boson method described in [32] (solid lines). In both figures, the dashed horizontal line denotes the lower band-edge of the anti-nodal patch, positioned at $\epsilon_{\text{min}} = -0.38$. The CTQMC figure on the right is taken from [32] (Fig. 3).

as in reference [32]. In Fig. 6.5 we see that for both NRG and CTQMC, starting at low doping, the gap continuously gets smaller before closing at $\delta_c = 0.16$. For NRG, it is slightly larger than for CTQMC at low doping. The NRG result suggests that it closes faster for low doping than shortly before reaching δ_c, whereas CTQMC rather suggests a linear doping dependence of the gap. It should be noted that the doping dependence of the gap is surprisingly smooth using NRG compared to the CTQMC result.

To conclude the discussion on the Hubbard model, in Fig. 6.6 the doping dependence of statistical weights of various cluster states is given. Here, S (blue) denotes the spin-singlet, 1+ (green) the states with one electron in the nodal orbital, T (black) the spin-triplet and E (red) the empty state. Note that for NRG, the weight of the whole multiplet is shown, while for CTQMC, the weight of a single state. Therefore, to directly compare values, the 1+ data for CTQMC has to be multiplied by 2 and the T data by 3. We see that the two methods compare quite well, and for both methods, the pseudogap is singlet dominant while for increased doping, the empty and single electron states dominate. For a more information and a more detailed discussion, refer to [32].

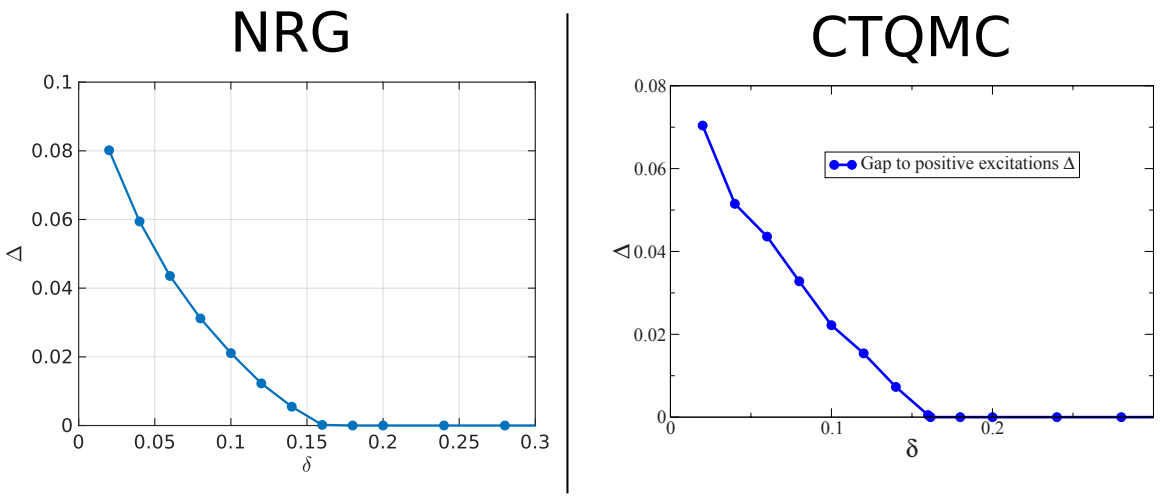

Figure 6.5: Doping dependence of the gap in the anti-nodal patch. The left panel shows NRG results produced for this thesis while the right panel shows results obtained with CTQMC, taken from [32] (Fig.8).

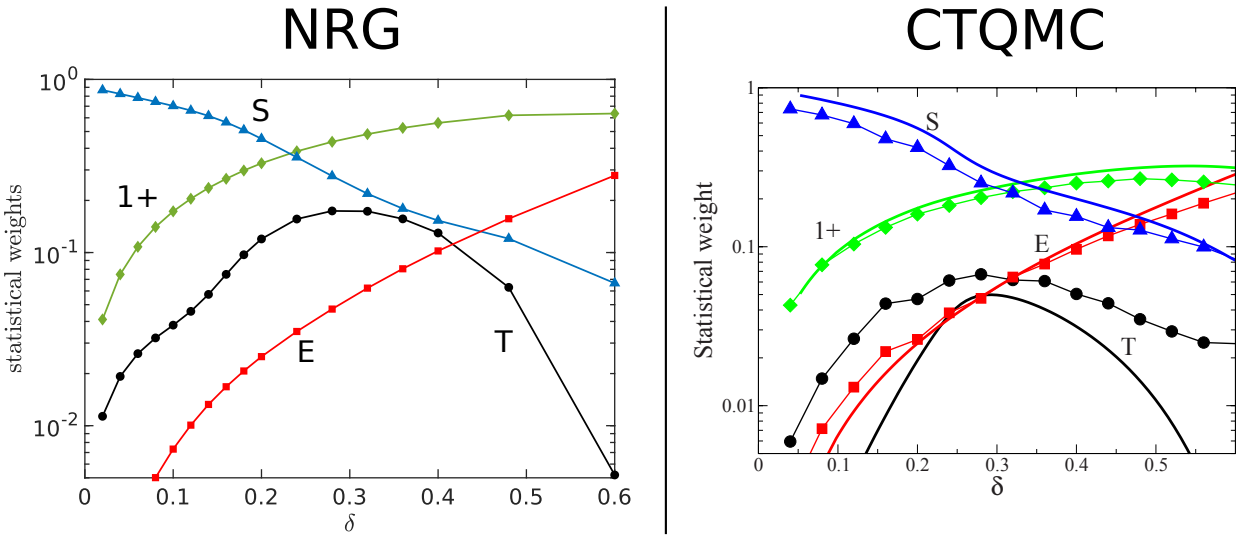

Figure 6.6: Statistical weights of various cluster states. S denotes the intra-cluster singlet, 1+ the state with one electron in the nodal orbital, T the intra-dimer triplet and E the empty state. Note that for NRG, the weight of the whole multiplet is shown, while the CTQMC data shows the weight of single states. In the right panel, symbols denote CTQMC data while the solid bold lines show slave boson results. Note that for NRG, multiplet dimensions are included, while this is not the case for CTQMC. To directly compare the values, the CTQMC data for 1+ (green) has to be multiplied by 2 while the one for T (black) must be multiplied by 3. For more information, refer to [32] Fig. 15, where the CTQMC and slave boson data was adapted from.

7 Quantum criticality in the periodic Anderson model

We will now turn to a two-site CDMFT approximation of the periodic Anderson model (PAM). This model is thought to be capable of describing heavy fermion (HF) compounds, some of which show a critical point at $T = 0$, called a quantum critical point (QCP). Hints on a QCP in the PAM using two-site CDMFT was found by De Leo *et al.* [9, 8] using exact diagonalization (ED) and by Sun and Kotliar [71] and Tanaskovič *et al.* [72] using quantum monte Carlo (QMC). However, while ED is able to access the QCP, it is not able to reliable resolve the vanishing small energy scales occurring at the QCP. Together with overall limited data quality, ED did not allow for a close investigation of the QCP. QMC, on the other hand, provides high quality data, but is not able to reach low enough temperatures to closely investigate the QCP. The necessary analytic continuation of the Matsubara data adds to this problem. Because of these difficulties arising with ED and QMC, we are here reconsidering the problem with NRG. Due to its construction, revealing ever lower energy scales when going down the Wilson chain, NRG is perfectly suited to resolve the vanishing energy and diverging time scales appearing at the QCP.

This chapter is structured in the following way. First, a short review of the current experimental and theoretical situation is given, motivating the numerical setup used later. Then, the PAM is introduced, and some technical details regarding the CDMFT approximation is given. Last, the results obtained with CDMFT + NRG are presented, where first the low temperature physics on both sides of the QCP, but well away from it is given. This will then lead us to a closer investigation of the QCP, where we will focus on two aspects of it, motivated by the current experimental and theoretical situation introduced earlier.

7.1 Motivation

The name "heavy fermions" (HF) is used for a class of materials showing Fermi-liquid (FL) behavior with remarkable large quasiparticle masses, sometimes exceeding 1000 times the bare electron mass [73, 74]. Their physics is derived from broad conduction bands (c-bands) hybridized to narrow, localized d- or f-orbitals (henceforth denoted just by "f-orbitals"). Some of these materials can be tuned between a FL and an antiferromagnetic (AFM) phase, through a critical point at zero temperature. Such a quantum critical point (QCP) can for example be observed in $YbRh_2Si_2$ (YRS) [75], which, at $T = 0$, can be tuned from its AFM phase to a FL by applying pressure or a magnetic field. At finite temperatures near its QCP, YRS shows pronounced non-Fermi-liquid (NFL) behavior, for example a linear temperature dependence of the resistivity [75, 76] and a logarithmic temperature dependence of the specific heat increment $\gamma = \frac{\Delta C}{T}$ [75, 76, 77, 78], where $\Delta C = C(T) - C(0)$ and $C(T)$ is the specific heat at temperature T.

It is generally believed that quantum criticality in HF systems is driven by the competition between Kondo screening and the Rudermann-Kittel-Kasuya-Yosida (RKKY) interaction (see [17, 74, 73] for more details on this). When a localized magnetic moment is antiferromagnetically coupled to a conduction band, the conduction electrons will try to screen the moment, which is generally known as Kondo screening. This screening is associated with a certain energy scale,

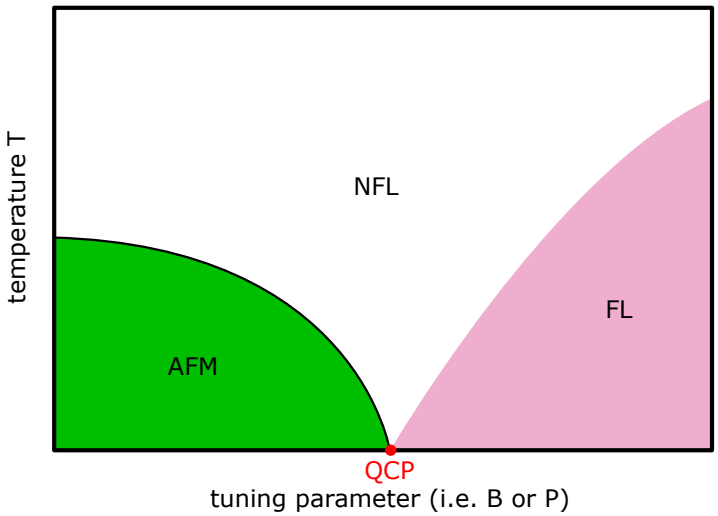

Figure 7.1: Schematic phase diagram of heavy fermion materials, depending on temperature versus some tuning parameter, where for example a magnetic field (B) or pressure (P) can serve. At zero temperature, an antiferromagnetic (AFM) and a Fermi liquid (FL) phase can be observed in certain tuning parameter ranges, separated by a quantum critical point (QCP). Above a certain temperature scale, non-Fermi liquid (NFL) behavior can be observed. Whether the FL temperature vanishes at the QCP is not fully settled and may be material dependent [74].

called the Kondo temperature

$$T_K \sim \exp\left(-\frac{1}{\rho_c J}\right) \quad , \tag{7.1}$$

where ρ_c is the conduction electron density of states at the Fermi level and J is the antiferromagnetic coupling constant between the local moment and the local conduction electron spin. At energy scales below T_K, the conduction band manages to screen the moment, thus quenching it, while at scales above T_K, it will behave like a free magnetic moment. The conduction electrons, on the other hand, will be antiferromagnetically correlated with the local moment in its vicinity due to the coupling J. If a second local moment is introduced close to the first one, it will feel this correlation, introducing an effective interaction between the two moments, termed the RKKY interaction. The strength of this effective coupling is of the scale

$$E_{\mathrm{RKKY}} \sim J^2 \rho_c \quad . \tag{7.2}$$

While the sign of the RKKY interaction changes with impurity distance, we will in the following assume it to be antiferromagnetic, which is realized when the local moments are one lattice spacing apart in a roughly half-filled conduction band, as this case will be relevant later. The Kondo effect and the RKKY interaction will compete with each other for moment-bath and moment-moment singlet formation, respectively. As they come with different functional dependencies on the coupling J, Kondo screening will dominate at large J while the RKKY interaction dominates the low J regime. This competition is particularly interesting when a local moment resides on every lattice site, as then a phase transition between an RKKY dominated and a Kondo dominant phase can be expected [79]. Such a Kondo-lattice model is believed to qualita-

tively describe most of the physics relevant to HF systems. The local moments in these systems are generated by the localized f-orbitals, where a strong Coulomb repulsion prevents double occupancy thereby suppressing charge fluctuations and leaving a singly occupied orbital with a spin degree of freedom. This spin degree of freedom is then antiferromagnetically coupled to the c-bands via virtual hopping between c and f states. When charge fluctuations are integrated out, one is then left, at low energy scales, with a Kondo lattice model.

While the existence of a QCP between a Kondo and an RKKY regime is well established, the nature of the QCP is still an unsettled issue. Regarding the QCP, there are two main scenarios under consideration [73, 74, 80]:

Hertz-Millis theory (Spin density wave instability)

Hertz-Millis theory [81, 82] describes the QCP as a spin density wave instability of the heavy Fermi liquid. Near the critical point, the quasi-particles are scattered by the critical spin density wave, but remain intact and evolve smoothly across the QCP. In particular, the specific heat increment, proportional to the inverse quasi-particle weight Z^{-1}, remains finite and the Fermi surface and together with the Hall coefficient R_H evolve smoothly across the QCP.

Kondo breakdown (KB)

In this scenario, in contrast to Hertz-Millis theory, the heavy quasiparticles break up at the transition. While in the Kondo regime, the QP are compounds of c and f states, in the RKKY regime the f states form local moments immersed in a Fermi liquid formed by the c-bands. Thus the Fermi surface (FS), incorporating both c and f electrons in the Kondo regime (large FS), jumps to a small FS incorporating only the c electrons in the RKKY phase. This means that Luttingers theorem [83], which relates the Fermi surface volume $\mathcal{V}_{\mathrm{FS}}$ to the particle number n_e,

$$n_e(\mathrm{mod}\quad 2) = 2\frac{\mathcal{V}_{\mathrm{FS}}}{(2\pi)^3} \quad , \tag{7.3}$$

suddenly becomes violated when going from the Kondo to the RKKY phase. This proposed jump of the effective carrier density n_e may lead to a jump of the Hall coefficient [80] $R_H \sim \frac{1}{n_e}$ at the QCP. Because the quasiparticles break up at the transition and are not smoothly connected across it, the quasiparticle residue Z needs to go to zero and the specific heat increment is expected to diverge. A complete and final description of the KB critical point is still missing, even though a lot has been proposed(e.g. [84, 85, 80]). An experimental example of a KB QCP can be found in the material YRS, already mentioned above. Most notable, a crossover of the Hall coefficient, which sharpens as $T \to 0$ and suggests a jump at $T = 0$, can be observed [86, 87] (see Fig. 7.2). In the following, based on the study done in [8, 9], the QCP in HF systems will be investigated using the periodic Anderson model (PAM) in a two site CDMFT approximation, as this is the minimal cluster size able to capture the competition of Kondo screening and RKKY interaction. We will thereby focus on a KB scenario, where experimental evidence on YRS [88, 89] shows that the antiferromagnetic and KB QCPs are distinct and can be separated by e.g. chemical pressure, suggesting frustration as an additional tuning parameter [90]. Therefore, as this also lowers the computational complexity, we will not allow for spin rotation symmetry breaking, thereby focusing on an artificially highly frustrated case.

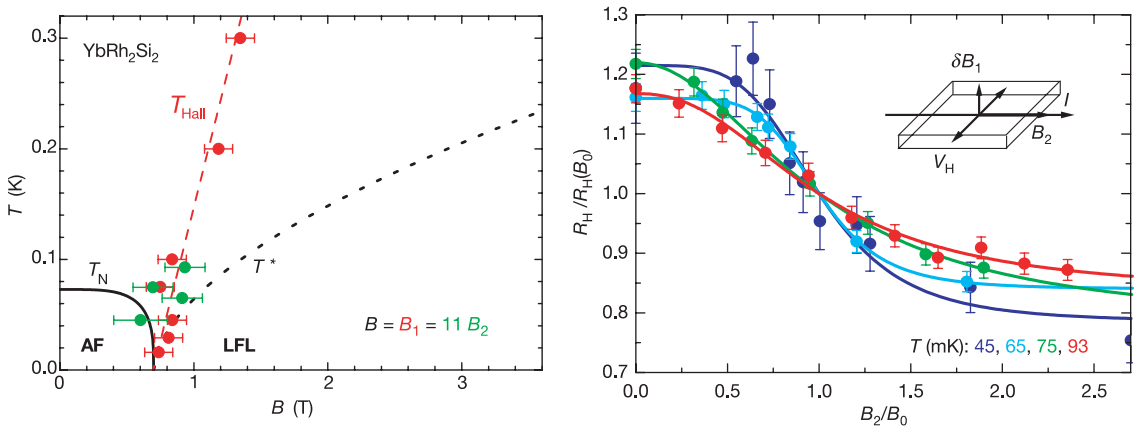

Figure 7.2: Experimental data on the crossover of the Hall coefficient in $YbRh_2Si_2$, measured by Paschen *et al.* [86] (Fig. 3a and 2b). On the left, the experimental phase diagram is shown in the temperature-magnetic field plane. YRS can be tuned with the magnetic field along a magnetically "hard" axis (B_1) and an "easy" axis (B_2), where around $\sim$ 11 times weaker fields are necessary compared to the "hard" axis. On the large field side for low temperatures, Landau Fermi liquid (LFL) behavior is observed, which crosses over to non Fermi liquid behavior at a temperature around $T^\star$. For low fields, YRS is antiferromagnetic (AF) below the Néél temperature T_N. The left panes shows the Hall coefficient measured by tuning along the "easy" axis, where the points denote measurements and the curves a best fit. R_H is normalized its value at a crossover field B_0, obtained from the fit. This crossover field is also shown in the phase diagram on the left by red (from measurement along "hard" axis) and green (measured along "easy" axis) dots. The dashed line marked by T_{Hall} shows the crossover line fitted to the experimental data. For $T \to 0$, the Hall coefficients on the right, which correspond to the green dots on the left, suggest a discontinuous jump. For more information, see [86].

7.2 Technical details

To study the KB critical point, the periodic Anderson model (PAM)

$$\begin{aligned} H_{\mathrm{PAM}} &= H_f + H_c + H_{c-f} \\ H_f &= (E_f - \mu) \sum_{i,\sigma} f^\dagger_{i,\sigma} f_{i,\sigma} + U \sum_i n^f_{i,\uparrow} n^f_{i,\downarrow} \\ H_c &= -\mu \sum_{i,\sigma} c^\dagger_{i,\sigma} c_{i,\sigma} - t \sum_{\langle i,j\rangle,\sigma} c^\dagger_{i,\sigma} c_{j,\sigma} \\ H_{c-f} &= V \sum_{i,\sigma} \left(f^\dagger_{i,\sigma} c_{i,\sigma} + h.c. \right) \end{aligned} \tag{7.4}$$

was employed. Here, $f_{i,\sigma}$ are annihilation operators for localized f-orbitals while $c_{i,\sigma}$ annihilate electrons in broad conduction bands (c-orbitals). Electrons in the f-orbitals are tightly bound by a binding energy E_f but also interact strongly via the density-density interaction U, while no direct hopping between f-orbitals is allowed. In contrast to that, c-electrons do not interact, but may hop between nearest neighbors with amplitude t. The electrons can locally move from c to f states with a hybridization strength V, described by H_{c-f}.

In the following, we will consider the PAM on a $d = 3$ cubic lattice, where the dispersion relation reads

$$\epsilon(\vec{k}) = -2t \sum_{\alpha=1}^{3} \cos(k_\alpha) \quad , \tag{7.5}$$

with the lattice spacing again set to 1. The band-width was set to $W = 12|t| \equiv 2$, while with $U = 10$, $E_f = -5.5$ and $\mu = 0.2$, an electron doped model is considered. These parameters were based on the studies done in [8, 9]. If not explicitly mentioned otherwise, all calculations were done at a temperature of $T = 10^{-8}$.

The PAM is, as in [8, 9], approached in a two site CDMFT approximation, to capture the competition between Kondo and RKKY physics. For that, the simple cubic lattice is tiled into

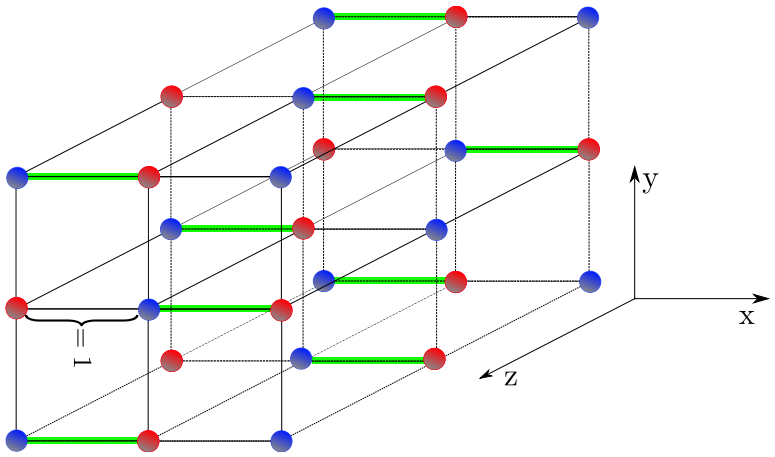

Figure 7.3: Tiling of a $d = 3$ simple cubic lattice into a face-centered cubic super-lattice of two-site clusters.

a face-centered cubic super-lattice of two-site clusters, illustrated in Fig. 7.3. The f-electron Green's function then reads

$$\boldsymbol{G}_f(\vec{k},\omega) = \left(\omega + \mu - E_f - V^2\boldsymbol{\mathcal{G}}_{c,0}(\vec{k},\omega) - \boldsymbol{\Sigma}_{cl}(\omega)\right)^{-1} \quad , \tag{7.6}$$

where $\boldsymbol{\mathcal{G}}_{c,0}(\vec{k},\omega)$ is the c-electron Green's function at $V = 0$. It is given by

$$\boldsymbol{\mathcal{G}}^{-1}_{c,0}(\vec{k},\omega) = \begin{pmatrix} \omega+\mu & e^{ik_x}\epsilon(\vec{k}) \\ e^{-ik_x}\epsilon(\vec{k}) & \omega+\mu \end{pmatrix} \quad , \tag{7.7}$$

where we have assumed that the clusters are aligned in x-direction. When setting up the cluster model

$$\begin{aligned} H_{\text{cluster}} &= H_{\text{cl}} + H_{\text{bath}} + H_{\text{hyb}} \\ H_{\text{cl}} &= (E_f - \mu)\sum_{i=1,2;\sigma} f^\dagger_{i,\sigma} f_{i,\sigma} + U\sum_{i=1,2} n^f_{i,\uparrow} n^f_{i,\downarrow} \\ H_{\text{bath}} &= \sum_{i=1,2;\lambda,\sigma} \epsilon_\lambda a^\dagger_{(\lambda,i),\sigma} a_{(\lambda,i),\sigma} \\ H_{\text{hyb}} &= \sum_{i,j,\lambda,\sigma} \left(V_{i,(j,\lambda)} f^\dagger_{i,\sigma} a_{(\lambda,j),\sigma} + h.c.\right) \quad , \end{aligned} \tag{7.8}$$

only the interacting f-orbitals are considered explicitly while the non-interacting c-band is put into the bath together with the dynamical mean field. The self-consistency equation then reads

$$\boldsymbol{G}_{f,\text{loc}}(\omega) = \int_{-\pi}^{\pi} \frac{\mathrm{d}^3\vec{k}}{(2\pi)^3} \boldsymbol{G}_f(\vec{k},\omega) \stackrel{!}{=} \boldsymbol{G}_{\text{cl}}(\omega) = (\omega + \mu - E_f - \boldsymbol{\Delta}(\omega) - \boldsymbol{\Sigma}_{cl}(\omega))^{-1} \quad , \tag{7.9}$$

where $\boldsymbol{\Delta}(\omega)$ is the hybridization function.

Note that the $\vec{k}$-integral cannot simply be done in this form with the tetrahedron method as $\boldsymbol{\mathcal{G}}_{c,0}(\vec{k},\omega)$ has a branch cut on the real axis and therefore is not a smooth function of $\vec{k}$. $\boldsymbol{\mathcal{G}}_{c,0}(\vec{k},\omega)$ therefore needs to be pulled out of the denominator. Furthermore, we can lump up the k_y and the k_z direction into a DOS integration, leaving in total only a two dimensional integration which is much easier to perform. All in all, the integral then reads

$$\begin{aligned} &\boldsymbol{G}_{f,\text{loc}}(\omega) = \\ &\boldsymbol{M}_{cl}(\omega) + V^2\boldsymbol{M}_{cl}(\omega)\int_{-\pi}^{\pi}\frac{\mathrm{d}k_x}{2\pi}\int_{-1}^{1}\mathrm{d}\varepsilon\rho_{\text{2D}}(\varepsilon)\left(\boldsymbol{\mathcal{G}}^{-1}_{c,0}(k_x,\varepsilon,\omega) - V^2\boldsymbol{M}(\omega)\right)^{-1}\boldsymbol{M}_{cl}(\omega) \\ &= \boldsymbol{M}_{cl}(\omega) + V^2\boldsymbol{M}_{cl}(\omega)\boldsymbol{G}_{c,\text{loc}}(\omega)\boldsymbol{M}_{cl}(\omega) \quad , \end{aligned} \tag{7.10}$$

where

$$\rho_{\text{2D}}(\varepsilon) = \int_{-\pi}^{\pi}\frac{\mathrm{d}^2\vec{k}}{(2\pi)^2}\delta\left(\varepsilon + 0.5(\cos(k_x) + \cos(k_y))\right) \tag{7.11}$$

is the DOS of a 2D square lattice,

$$\boldsymbol{\mathcal{G}}^{-1}_{c,0}(k_x,\varepsilon,\omega) = \begin{pmatrix} \omega+\mu & -2te^{ik_x}\left(\cos(k_x)+2\varepsilon\right) \\ -2te^{-ik_x}\left(\cos(k_x)+2\varepsilon\right) & \omega+\mu \end{pmatrix} \quad , \tag{7.12}$$

the inverse c-Green's function at $V = 0$ and

$$\boldsymbol{M}_{cl}(\omega) = (\omega + \mu - E_f - \boldsymbol{\Sigma}_{cl}(\omega))^{-1} \tag{7.13}$$

is the cluster cumulant. This also gives a relation between the local cluster f-Green's function $\boldsymbol{G}_{f,\mathrm{loc}}(\omega)$ and the corresponding c-Green's function $\boldsymbol{G}_{c,\mathrm{loc}}(\omega)$.

The cluster model Eq. (7.8) is solved via the interleaved NRG, where the bonding and anti-bonding

$$f_{\pm,\sigma} = \frac{1}{\sqrt{2}}(f_{1,\sigma} \pm f_{2,\sigma}) \tag{7.14}$$

states where interleaved, as these are not related by the lattice inversion symmetry. As parameters for the NRG, the discretization parameter was set to $\Lambda = 3$, the number of kept states at each iNRG iteration was $N_{\mathrm{keep}} = 10000$ and $n_z = 2$ z-shifts were conducted.

In the following, only translation invariant solutions will be considered and to compute continuous lattice quantities after convergence, reperiodization will be done via the cumulant

$$M(\vec{k},\omega) = (\boldsymbol{M}_{cl})_{1,1}(\omega) + (\boldsymbol{M}_{cl})_{1,2}(\omega) \cdot \frac{1}{3}\sum_{\alpha=1}^{3}\cos(k_\alpha) \quad . \tag{7.15}$$

Later, also the Hall coefficient R_H will be calculated from the reperiodized result via the equations (4-18) given in [91]. Note that the spectral function in Eq. (4,5) of [91] is only the c-electron one, as the f-electrons lack a direct, non-local hopping term and therefore do not directly contribute to linear electromagnetic transport.

7.3 Low temperature physics far from the transition

To set the stage for examining the QCP, we first want to investigate the behavior on both sides of it far from the transition. We begin with showing the local cluster spectral function of both the c- and f-orbitals in the RKKY regime ($V = 0.4$) and the Kondo phase ($V = 0.7$) in Fig. 7.4. The QCP lies closer to the shown RKKY result at $V_c \simeq 0.4575$ and the Hubbard bands are positioned at $\omega \sim \pm 5$, well out of the shown frequency range.

In the Kondo phase, a clear Kondo resonance at the Fermi level is visible. Also, the c- and f-electron spectral functions are of the same magnitude at $\omega = 0$, indicating that both are itinerant and contribute to the Fermi surface. We therefore expect that Luttinger's theorem Eq. (7.3) is obeyed. On the logarithmic scale, it can be seen that the Kondo peak has a width of $\sim 10^{-2}$–10^{-3}, which indicates that the Fermi liquid temperature T_{FL}, which is discussed later together with Fig. 7.6, is of this order. The quasiparticle residue Eq. (7.16) is $Z = 0.0291$ for $V = 0.7$, which means that the quasiparticle masses are enhanced by a factor $Z^{-1} \simeq 35$. Notice also the large pseudogap at negative frequencies, which is most prominently visible in the c-orbital spectral function. This is the hybridization gap, already opening up in the $U = 0$ case due to V. It therefore signals that f and c electrons are strongly hybridized and suggests that the Kondo phase is adiabatically connected to the $U = 0$ case.

This is in stark contrast to the RKKY phase, where the hybridization gap is missing, indicating that c- and f-orbitals are mostly decoupled. An even clearer indicator for this is the missing Kondo peak, which has been replaced by a pseudogap, and the much smaller spectral weight near $\omega = 0$ compared to the Kondo phase. It is therefore expected that the f-electrons do not contribute to the Fermi surface any more. As the f-orbitals are nevertheless roughly singly occupied, Luttingers theorem Eq. (7.3) is violated as a result. Also notice the peaks in the f-spectral function at $|\omega| \sim 10^{-4}$ and the corresponding suppressions in the c spectral function.

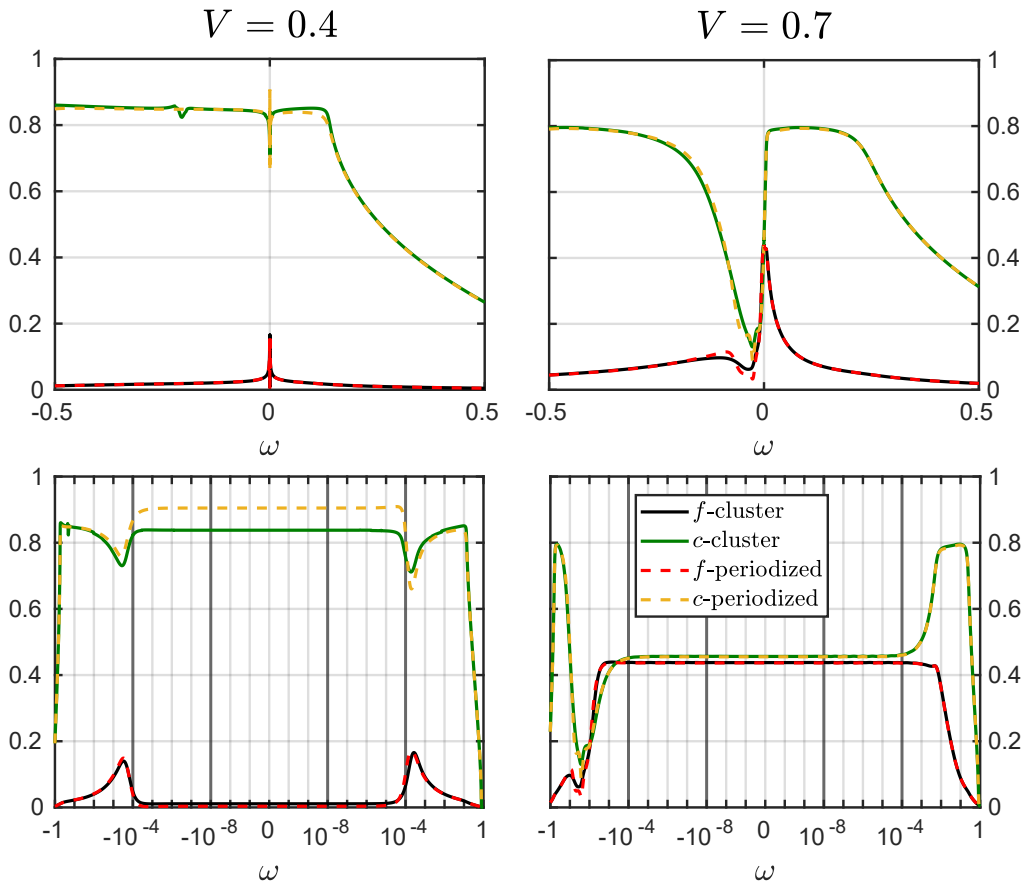

Figure 7.4: Local spectral functions for both the RKKY ($V = 0.4$) and the Kondo ($V = 0.7$) phases. For better visibility of the low energy structure, a logarithmic scale in the lower panels is provided in addition to the linear one in the upper panels. The dashed lines show the local spectral functions calculated with the reperiodized self-energy while the solid lines show the local cluster spectral functions. Note that the Hubbard bands are at $\omega \sim \pm 5$ and thus not in the picture.

It turns out that this is the energy scale of antiferromagnetic spin fluctuations on the RKKY side (see Fig. 7.10 and the discussion around it), which are not only quite large, but also fairly localized in energy in this phase. One may infer that quasiparticles are therefore only well defined up to $|\omega| \lesssim 10^{-4}$ and are broken up by violent spin fluctuations at $\omega \sim \pm 10^{-4}$. As a result, the Fermi liquid temperature T_{FL} (see discussion on Fig. 7.6) should be of this order. In the numerical calculation, it is found that the quasiparticle residue at $V = 0.4$ is $Z = 3.26 \cdot 10^{-5}$, which at a first glance is surprising as one might expect Z to be large when the c-orbitals are decoupled from the f ones, at least larger than in the Kondo phase. Such a comparably small quasiparticle residue, indicated by measurements of the specific heat increment γ, has also been found in experiments [78] and is to our knowledge to date still unexplained.
The quasiparticle residue

$$Z = \left(1 - \frac{\partial \Sigma(\omega)}{\partial \omega}\bigg|_{\omega=0}\right)^{-1} \tag{7.16}$$

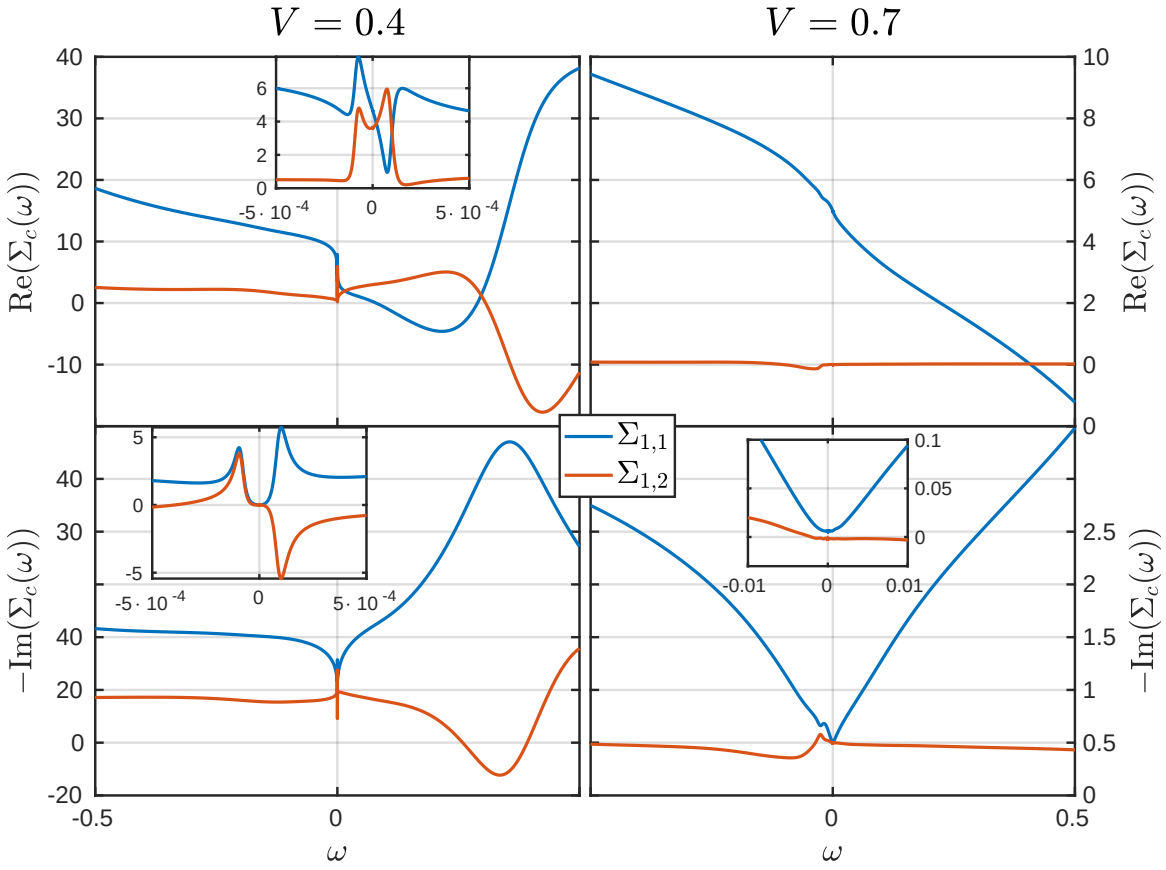

Figure 7.5: Real and imaginary part of the cluster self-energy in the Kondo ($V = 0.7$) and the RKKY ($V = 0.4$) regime. The insets show a zoom into the low frequency dependence.

can be calculated from the self-energy, shown in Fig. 7.5. We see that in the RKKY phase, the real part of $\Sigma_{1,1}$ indeed has a slope of order 10^4, while $\Sigma_{1,2}$ has a local minimum at $\omega = 0$. This means that Z is of the order of 10^{-4} for both the bonding and the anti-bonding cluster states, suggesting that Z is uniform over momenta. On the RKKY side, one further immediately notices the peaks at $|\omega| \simeq 10^{-4}$ in both the real and the imaginary part of Σ, associated with scattering due to AFM spin excitations. From the imaginary part, we see that the scattering rates at $\omega \simeq \pm 10^{-4}$ are quite large, though they differentiate between bonding and anti-bonding. While hole excitations have low scattering rate in the anti-bonding state, they are strongly scattered in the bonding orbital, and vice versa for particle excitations. This in turn means that the scattering rates at $\omega \simeq 10^{-4}$ are strongly non-local and therefore momentum dependent. Overall, the non-local part of the self-energy is comparable to the local one in the RKKY phase, reflecting the large non-local antiferromagnetic correlation of the f orbitals by the RKKY interaction.

In the Kondo regime however, the situation is vastly different. Here, the non-local part of the self-energy is practically negligible compared to the local one, reflecting that f- and

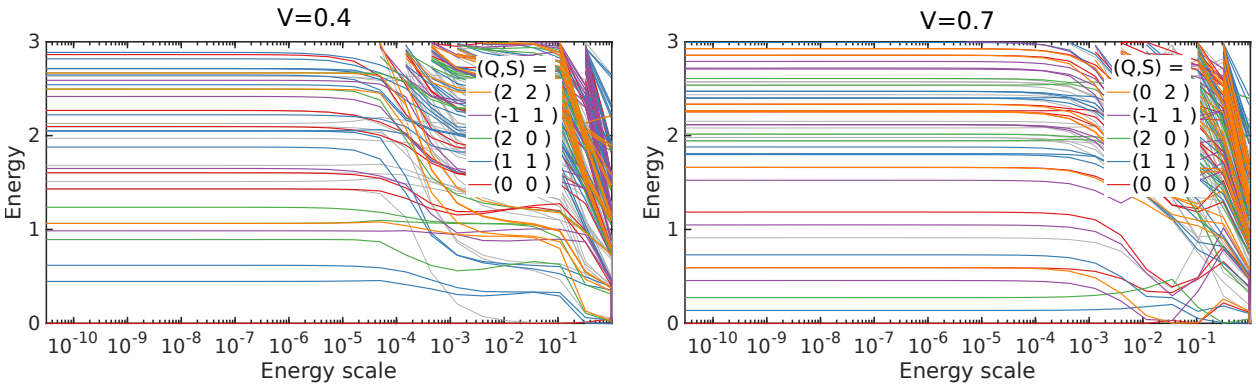

Figure 7.6: NRG flow of the low energy spectra along the Wilson chain, rescaled by their respective energy scale. The spectra are shown for even (≡ even number of Wilson chain sites) NRG iterations only. Q and S denote the total charge and spin quantum numbers of the states, respectively. The system is in the Kondo phase for $V = 0.7$ and in the RKKY phase for $V = 0.4$.

c-orbitals become locally strongly entangled by forming Kondo singlets, leaving no room for non-local antiferromagnetic f-f correlations. It should also be noted that the overall scale of the self-energy in the Kondo phase is considerably smaller than in the RKKY regime, while also showing much less complex frequency behavior, suggesting that the Kondo phase is generally less correlated. Surprisingly, the imaginary part of Σ on the Kondo side is of order 10^{-2} at $\omega = 0$, which is quite large and uncommon for a Fermi liquid at $T = 0$. On the other hand, a Fermi liquid like ω^2 behavior at low frequencies can be observed. For the RKKY side of the transition, the imaginary part of the self-energy seems not to follow a ω^2 dependence, but rather some larger power law at low frequencies. While this is not completely at odds with a well defined, coherent quasiparticle part in the spectral function, it nevertheless poses the question if at low energies, the system is indeed described as a Fermi liquid.

Fortunately, this can unambiguously be resolved by looking at the flow of the finite size spectra generated by the NRG, shown in Fig. 7.6. Here, the lowest few eigenstates at even NRG iterations, rescaled by their respective energy scale, is depicted. We see, that in both the Kondo and the RKKY regime, a low energy fixed point with a Fermi liquid spectrum is reached at energy scales below $\sim 10^{-3}$ and $\sim 10^{-4}$, respectively, as in both cases in this fixed point, the low energy spectrum is completely determined by the lowest single particle excitations. The crossover region to the stable Fermi liquid fixed point is therefore at an energy scale well above the temperature $T = 10^{-8}$ namely at $\sim 10^{-4}$ in the RKKY and $\sim 10^{-3}$ in the Kondo phase and coincide with the Fermi liquid temperatures conjectured in the discussion above. In the RKKY phase, an intermediate, unstable fixed point between energy scales 10^{-3} and 10^{-1} can be made out. Its nature is to date unknown to us, though it is certainly interesting to investigate it, as it governs the high temperature physics at $V = 0.4$ and might describe the non-Fermi liquid behavior observed in experiments. For the Kondo regime, the eigenenspectrum flows much faster towards the Fermi liquid, and no intermediate fixed point can be made out over a finite energy range. When approaching the KB QCP, we expect that the crossover scale towards the Fermi liquid goes to zero and as a result, the physics at any finite temperatures will be governed by

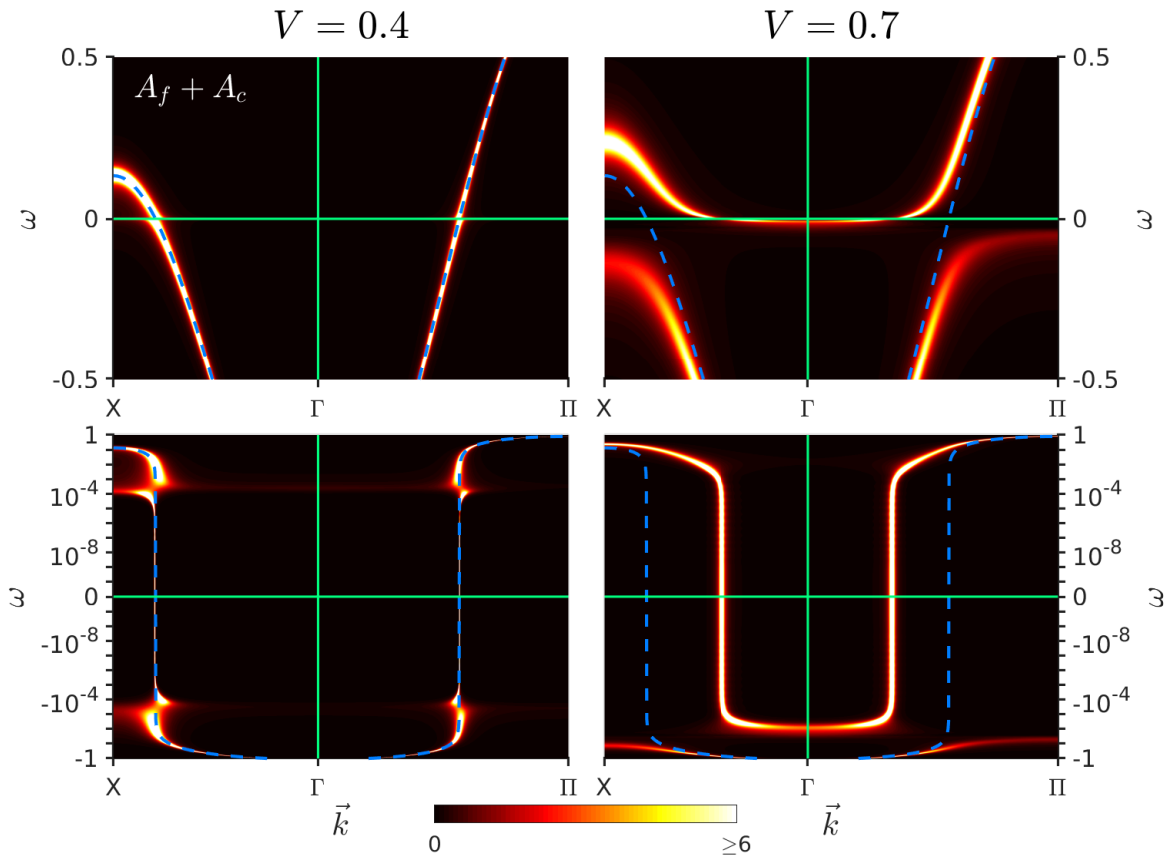

Figure 7.7: Total $\vec{k}$-resolved spectral function on a linear (upper panels) and a logarithmic (lower panels) frequency scale. The $\vec{k}$-path is chosen from $X = (\pi, \pi, 0)$ over $\Gamma = (0, 0, 0)$ to $\Pi = (\pi, \pi, \pi)$. For reference, the dispersion at $V = 0$ (blue dashed line) and the chemical potential (green horizontal line) are drawn. For $V = 0.7$, the system is in a Kondo phase while for $V = 0.4$ it is in an RKKY phase.

an extended, non Fermi liquid fixed point.

Before studying the QCP itself, we would first like to investigate the bandstructure and the Fermi surface of the RKKY and Kondo phases well away from the transition. To accomplish this, the converged cluster result is reperiodized using Eq. (7.15). We test the quality of the interpolation by computing the local spectral functions with the reperiodized self-energy, shown as dashed lines in Fig. 7.4. It can be seen that the reperiodized result matches the one obtained directly from the cluster model quite w well. With the quality established, will now have a look at the total $\vec{k}$-resolved spectral function $A_c(\vec{k}, \omega) + A_f(\vec{k}, \omega)$, shown as an intensity map in Fig. 7.7. On the RKKY side, shown in the left panels, the spectral function mostly follows the $V = 0$ dispersion (dashed blue line) of the c-electrons. However, on the logarithmic frequency scale, flat features at $|\omega| \sim 10^{-4}$ can be seen, associated with antiferromagnetic excitations.

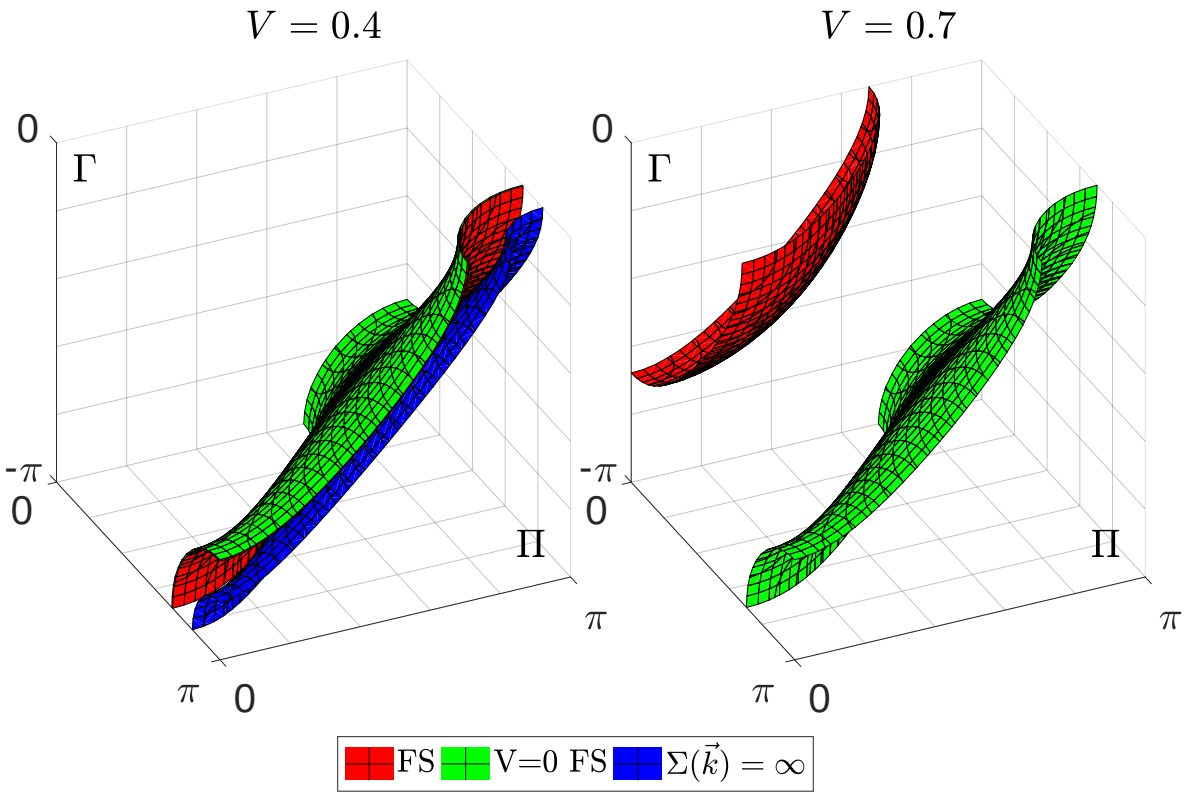

Figure 7.8: Fermi surfaces on both sides ($V = 0.7$: Kondo, $V = 0.4$: RKKY) of the QCP in one octant of the first Brillouin zone. The actual Fermi-surface is shown in red and defined by Eq. (7.17) while the $V = 0$ Fermi-surface is shown in green as a reference. On the RKKY side, a $\Sigma(\vec{k}, \omega = 0) = \infty$ surface shows up which is numerically calculated from $\mathrm{Re}(M(\vec{k}, \omega = 0)) = 0$. The $\Gamma = (0, 0, 0)$-point in the upper left corner while the $\Pi = (\pi, \pi, \pi)$ point is in the lower right corner.

Notably, for $|\omega| > 10^{-4}|$, the spectral function becomes considerably broader and scattering seems to be enhaced compared to the $|\omega| < 10^{-4}$ range, where an extremely thin band suggests that quasiparticles are unaffected by scattering. The most obvious difference from the $V = 0$ bandstructure can be observed at $\omega = \pm 10{-}4$ itself, where the $V = 0$ band seems to be disconnected, such that a three band structure rather than a single band is suggested. The band which crosses the Fermi level is thereby squeezed between $-10^{-4} < \omega < 10^{-4}$, rendering it extremely flat, in line with the small quasiparticle residue discussed earlier. Nevertheless, the crossing of the Fermi level coincides with the $V = 0$ case, suggesting a respective Fermi surface, as expected in the RKKY regime.

In contrast, on the Kondo side, the spectral function crosses the Fermi surface at a considerably

different point, hinting that the Fermi surface may reconstruct at the QCP in between, as expected in the KB scenario. In total, the spectral function on the Kondo side is as expected, and its two band structure can be inferred from the $U = 0$ case, as already mentioned earlier. Turning on U then renormalizes the bands, but leaves the crossing of the Fermi level of the upper band as a Kondo resonance. The only notable qualitative difference from the $V = 0$ case is the relative broadness of the spectral function, even at small ω, which is related to the non-zero imaginary part of $\Sigma(\omega = 0)$ already discussed earlier.

To conclude the discussion on the physics well away from the QCP, we will have a look at the Fermi surfaces, shown in Fig. 7.8 in one octant of the first Brillouin zone. All other octants can easily be obtained via the symmetries of the cubic lattice. The FS was calculated by searching the zeros of the real part of the inverse c-electron Green's function at the Fermi level.

$$\mathrm{Re}\left(\mu - \epsilon(\vec{k}) - V^2 M(\vec{k}, \omega = 0)\right) \stackrel{!}{=} 0 \quad . \tag{7.17}$$

As long as the imaginary part of $\mathbf{\Sigma}(\omega = 0)$ is not too large, this coincides well with the real part zeros of the inverse f-orbital Green's function. For the data shown in Fig. 7.8, this was explicitly checked and it was further confirmed that the surface coincides with the intensity maxima of the spectral functions at $\omega = 0$. In Fig. 7.8, the Fermi surface of the c-electrons at $V = 0$ is also shown as a reference. Note that for finite V, the inverse f-electron Green's function has poles on this surface, thus $\boldsymbol{G}_f(\vec{k}, \omega = 0)$ is zero there. A second surface of zeros of G_f also appears on the RKKY side, where the self-energy has a surface of divergencies. Thereby, the Fermi surface, where $\mathrm{Re}(G_f^{-1}(\vec{k}, \omega))$ becomes zero, is sandwiched between two surfaces where the inverse f-orbital Green's function diverges, suppressing its spectral weight at $\omega = 0$ and thus decoupling it from the c-states.

On the Kondo side, no $\Sigma(\vec{k}, \omega = 0) = \infty$ surface can be observed, thus its appearance is a clear feature of the RKKY phase. The Fermi surface on the Kondo side is centered around the $\Gamma = (0, 0, 0)$-point, opposed to the $V = 0$ Fermi surface and the one on the RKKY side, which are both centered around $\Pi = (\pi, \pi, \pi)$. Therefore, the charge carriers on the Kondo side are particle like, while on the RKKY side, they are hole like. This implies that we can expect the Hall coefficient

$$R_H \equiv \frac{1}{q_H \cdot n_H} \tag{7.18}$$

where n_H is the effective Hall carrier density and q_H their charge, to be negative on the Kondo side ($q_H = -e$, where e is the elementary charge), while it will be positive for the hole like carriers in the RKKY side.

7.4 Evolution across the QCP

After the discussion of the Kondo and RKKY phases well away from quantum criticality, we would like to investigate the QCP itself, which was found to be at the critical hybridization $V_c = 0.4575$. This is done in two parts, which is due to two different reasons. First, we want to establish in this section whether the QCP is a Hertz-Millis type one or a Kondo breakdown critical point. To do that, we will examine the behavior of the two main hallmarks distinguishing them. This is the suppression of the Fermi liquid scale and the vanishing of the quasiparticle

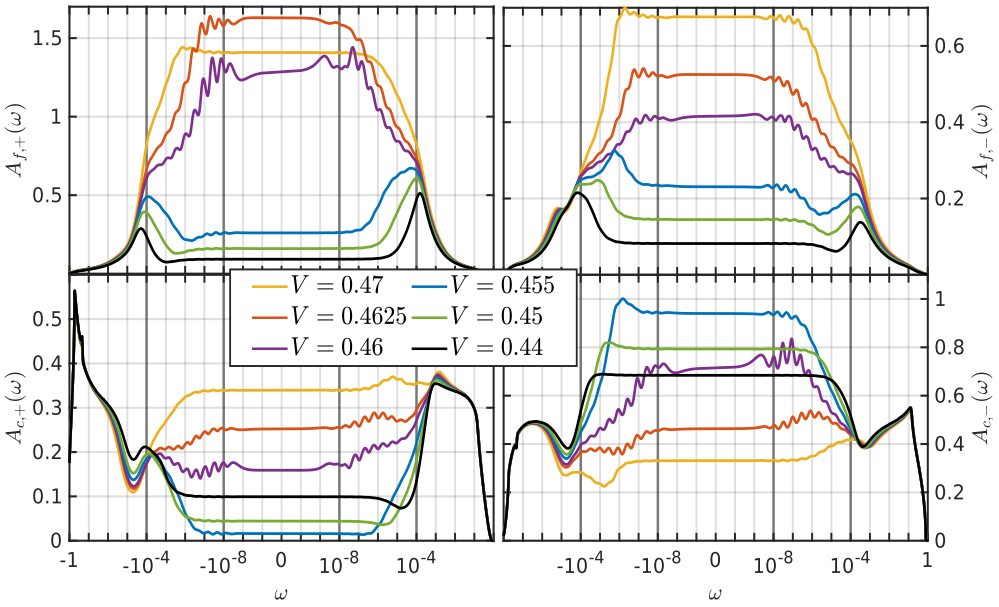

Figure 7.9: Evolution of the c (lower panels) and f (upper panels) electron cluster spectral functions across the QCP, for both the bonding (left panels) and the anti-bonding (right panels) cluster states. The system is in a Kondo phase for $V > V_c = 0.4575$ and in an RKKY phase for $V < V_c$. Note the wiggles at low frequencies, which especially become quite large near $V = V_c$ on the Kondo side. These are due to underbroadening of the discrete spectral data, which seems to affect results more severely the closer they are to the transition. The wiggles can fortunately be tamed by using a larger broadening width. This should however be done self-consistently and not as a post-processing step. As this has not been done systematically yet, the underbroadened results are shown.

residue in the whole Brillouin zone at the Kondo breakdown QCP, in contrast to the Hertz-Millis QCP, in the first place, and the Fermi surface reconstruction with a corresponding change in the Hall coefficient in the KB scenario on the other hand. Second, when the suppression of the Fermi liquid scale is examined, there is no need for reperiodization, which means that all quantities used in this part are the self-consistent cluster quantities directly obtained from the CDMFT. To investigate the Fermi surface however, reperiodization is necessary, which is the reason why all results in the second part are obtained from the reperiodized self-energy, calculated via Eq. (7.15). As the reperiodization is somewhat ad hoc, a clear line dividing self-consistent and reperiodized results is nice to have.

7.4.1 Suppression of the Fermi liquid scale at the QCP

In the Kondo breakdown scenario of the heavy fermion QCP, the Fermi liquid temperature renormalizes to zero at the critical point. Therefore, when going from Kondo to RKKY, a new Fermi liquid arises and the quasiparticles of the Kondo and RKKY phases are not adiabatically connected. This in turn means that the quasiparticle residue Z renormalizes to zero for all momenta and the specific heat increment $\gamma = \frac{\Delta C}{T} \sim Z^{-1}$ diverges.

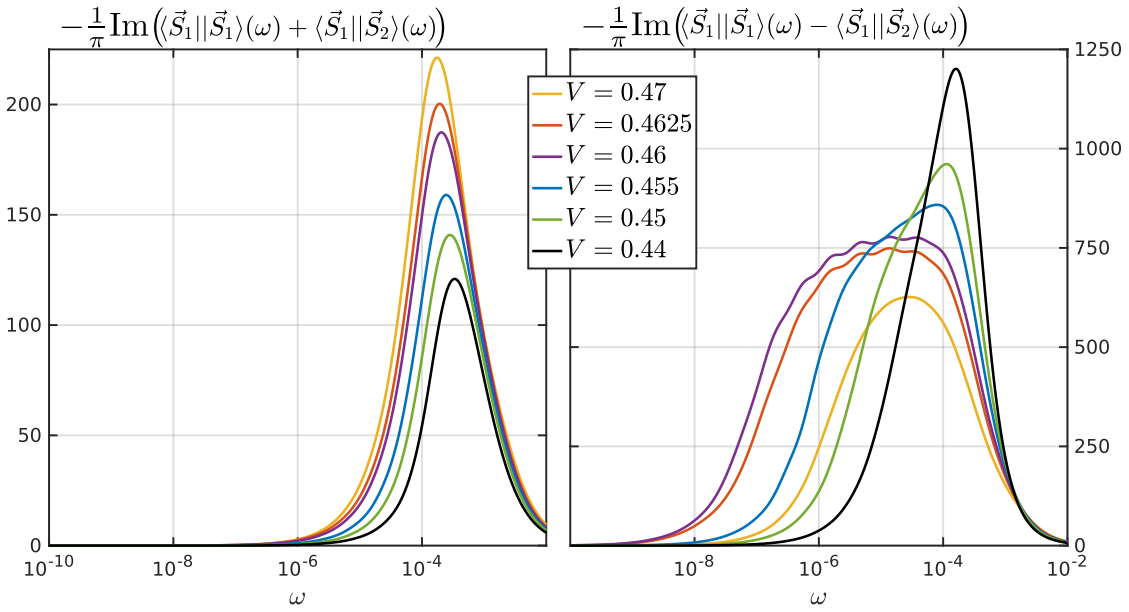

Figure 7.10: Evolution of the imaginary part of the ferromagnetic (left panel) and the antiferromagnetic (right panel) spin susceptibility. For $V > V_c = 0.4575$, the system is in a Kondo phase while for $V < V_c$, it is in an RKKY phase.

The decrease of the Fermi liquid scale can be seen from the width of the Kondo peak in the f-spectral function, shown in Fig. 7.9. We see that for $V > V_c = 0.4575$, the Kondo peak gets considerably narrower as the transition is approached. This narrowing equally affects the bonding and the anti-bonding orbitals, suggesting that both Z_+ and Z_- vanish at the QCP, which in turn means that Z vanishes for all momenta. After the critical point, at $V < V_c$, the Kondo peak in the f-spectral function is replaced by a pseudogap, signaling that the f-c composite quasiparticles at the Fermi surface have broken up. It should again be mentioned that this happens at the same time for bonding and anti-bonding, which means that the breakdown is uniform in $\vec{k}$-space and thus local in real space. Also, the absolute value of the f-spectral function at $\omega = 0$, while considerably different for bonding and anti-bonding on the Kondo side, is roughly equal after the KB on the RKKY side. All this suggests that the f-orbitals suddenly stop contributing to the coherent quasiparticle part of the spectral function at the Fermi surface when going through the QCP. Note however, that at $\omega \simeq \pm 10^{-4}$, new peaks are emerging, whose energy scale is roughly equal to the characteristic scale of antiferromagnetic excitations in the RKKY phase.

In contrast to the f-spectral function, which becomes of same magnitude at the Fermi level in the RKKY regime, the c-spectral function at $V = 0.455$ becomes almost gapped for the bonding state while it displays a narrow peak in the anti-bonding orbital. As the coherent part of the spectral function at $\omega = 0$ is contributed by the c-electrons, this means that the Fermi-surface moves from the Γ-point at $V > V_c$, which is represented by the bonding part, to the Π-point at $V < V_c$, represented by the anti-bonding spectral function. The resulting Fermi surface reconstruction and its implication on the Hall coefficient will be discussed in the second part of the discussion on the QCP.

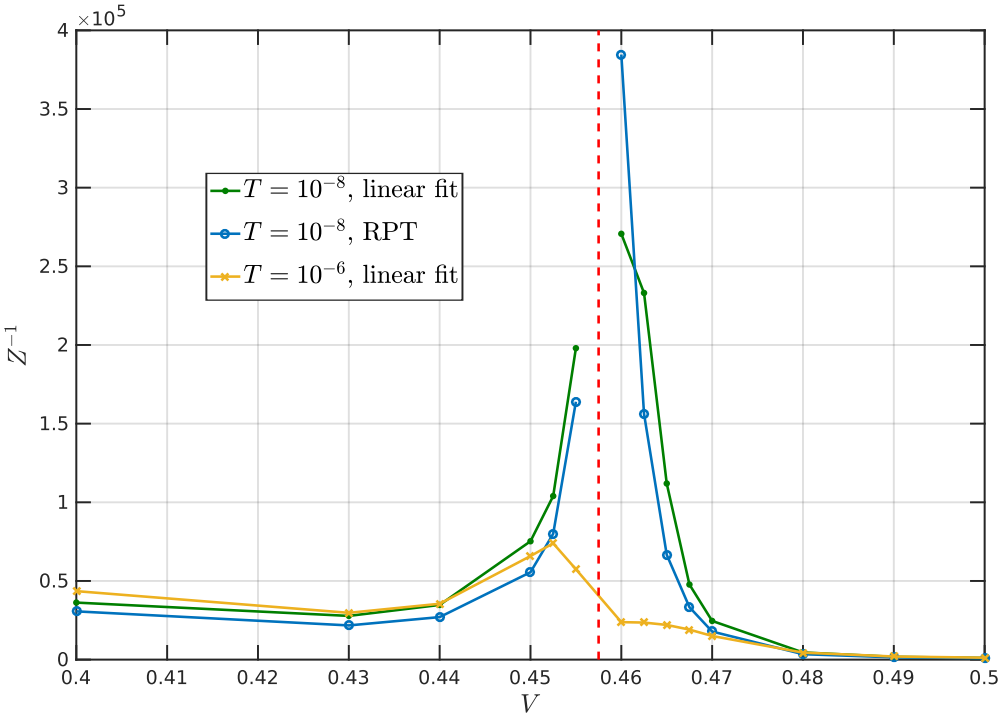

Figure 7.11: Behavior of the inverse quasiparticle residue across the QCP. The critical hybridization $V_c = 0.4575$ is marked as a red dashed line, while for $V > V_c$, the system is in a Kondo phase and for $V < V_c$ in an RKKY phase. The blue line is obtained from renormalized perturbation theory (RPT) [92, 93] at $T = 10^{-8}$ directly from the low energy Fermi liquid fixed point, while the green and yellow lines are obtained from a linear fit to the self-energy at $\omega = 0$ and Eq. (7.16) for $T = 10^{-8}$ and $T = 10^{-6}$, respectively. All results are averaged over bonding and antibonding contributions, which, at least in the shown parameter regime, differ by a factor of $\mathcal{O}(1)$.

It is of course desirable to investigate what suppresses the Fermi liquid scale when going to the QCP and to identify the degrees of freedom which loose their characteristic energy scale and become quantum critical. As, on grounds of the competition of between Kondo effect and RKKY interaction, we suspect magnetic fluctuations to be a possible candidate for this, we will now investigate their density of states, shown in Fig. 7.10. Here, $\langle \vec{S}_i || \vec{S}_j \rangle(\omega)$ denotes the imaginary part of the retarded spin correlator in the real-space basis,

$$\langle \vec{S}_i || \vec{S}_j \rangle(\omega) = \int_{-\infty}^{\infty} \mathrm{d}t \left(-i\Theta(t) \left\langle \left[\vec{S}_i(t), \vec{S}_j \right] \right\rangle \right) e^{i\omega t} \quad . \tag{7.19}$$

From the ferromagnetic (FM) part $\langle \vec{S}_1 || \vec{S}_1 \rangle(\omega) + \langle \vec{S}_1 || \vec{S}_2 \rangle(\omega)$, we see that the characteristic energy scale of FM spin excitations is well defined across the QCP, with an energy scale somewhere between 10^{-4} and 10^{-3}, which increases as one moves from large to low V. Also, the overall scale of $\langle \vec{S}_1 || \vec{S}_1 \rangle(\omega) + \langle \vec{S}_1 || \vec{S}_2 \rangle(\omega)$ decreases as V is lowered, as expected when the antiferromagnetic nature of the RKKY interaction is remembered.

In contrast to that, the overall scale of AFM susceptibility $\langle \vec{S}_1 || \vec{S}_1 \rangle(\omega) - \langle \vec{S}_1 || \vec{S}_2 \rangle(\omega)$ increases

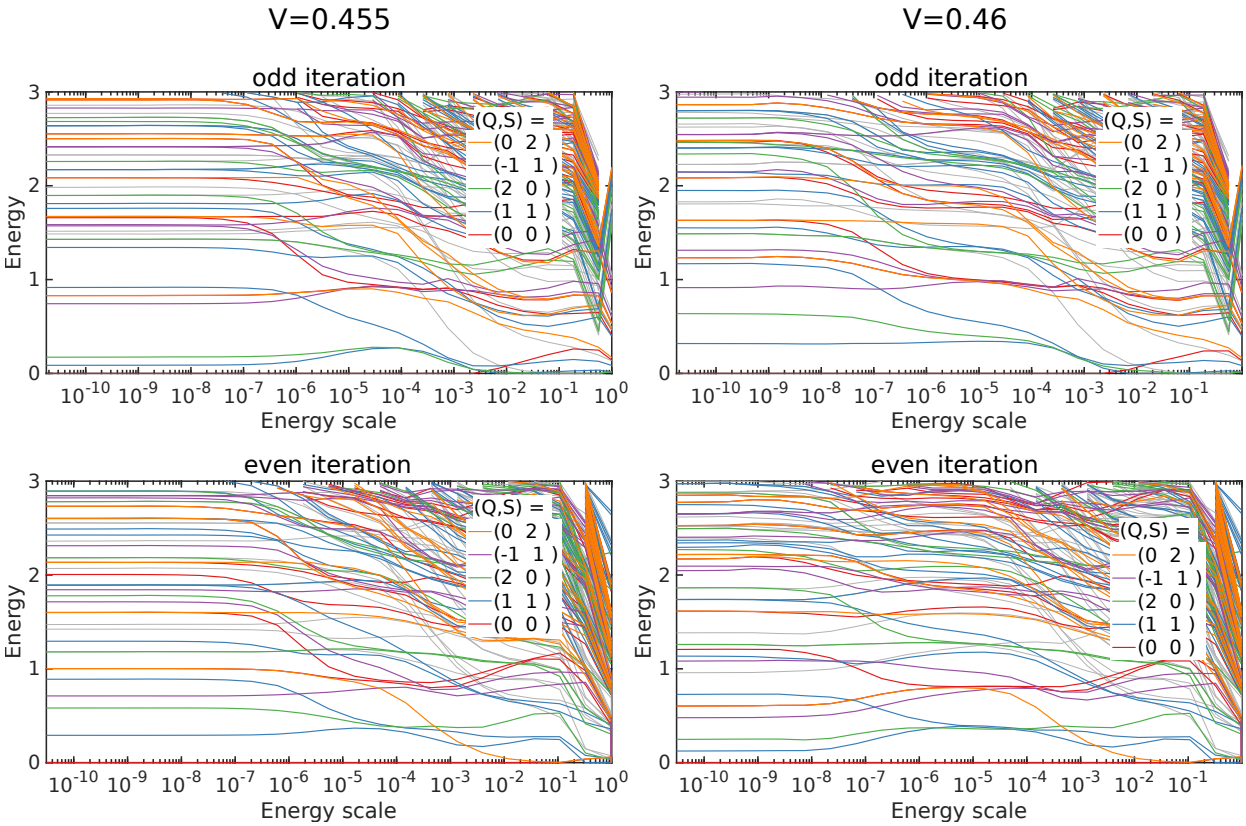

Figure 7.12: Energy level flow chart obtained from odd (upper panel) and even (lower panel) NRG iterations. The left panel shows the closest available solution to the QCP at $V_c = 0.4575$ in the RKKY phase while the right one shows the respective solution in the Kondo phase. The x-axis shows the energy scale of the respective NRG iteration, by which the eigenenergies are rescaled. Q and S denote the total charge and spin quantum numbers of the states, respectively.

when V is lowered, and is overall of larger scale than the FM one. Most important however, the AFM excitations loose their characteristic energy scale when approaching the QCP. This is most clearly seen at $V = 0.46$, where the AFM fluctuations extend over roughly 3 decades in ω. Note that the temperature is 10^{-8}, which could already prevent the fluctuations to extend up to even lower energy scales than is the case here. At the QCP itself at $T = 0$, it is expected that the AFM spin excitation density of states extends from its high frequency cutoff at $\omega \simeq 10^{-4}$ down to $\omega = 0$, meaning that AFM spin fluctuations extend over arbitrary time scales, with a low time cutoff given by the frequency $\omega \simeq 10^{-4}$. On the RKKY side of the transition, we see that a characteristic energy scale at $\omega \simeq 10^{-4}$ emerges and AFM fluctuations can again be associated with a characteristic time or energy scale. The strong AFM fluctuations suggest that they break up coherent quasiparticles above ever lower energy scales, thereby renormalizing the Fermi liquid scale and the quasiparticle fraction Z to zero.

That this is indeed the case, is shown in Fig. 7.11, where the inverse quasiparticle fraction, which is directly proportional to the specific heat increment γ, is displayed. It can be calculated, assuming Fermi liquid behavior, from a linear fit to the real part of the self-energy at $\omega = 0$

and by invoking Eq. (7.16), or directly from the low energy Fermi liquid fixed point in the NRG flow using renormalized perturbation theory (RPT) [92, 93]. In general, the RPT result is more reliable, as it directly and solely accesses the Fermi liquid and is not affected by non Fermi liquid effects showing up when the temperature reaches the Fermi liquid scale. Also and more importantly, the linear fit to the self-energy is prone to some arbitrariness. In Fig. 7.11, both the result from linear fitting and from RPT is shown. As the quasiparticle residue is not vastly different for bonding and anti-bonding channels, differing, at least for the shown parameters, only by a factor of $\mathcal{O}(1)$, their mean value is shown. This is also owed to difficulties of distinguishing them in RPT, as bonding and anti-bonding cannot be easily separated due to missing conserved quantum numbers characterizing them unambiguously. From the RPT result in Fig. 7.11, we see that Z^{-1} really diverges at the QCP, which reassures that the we are really dealing with a Kondo breakdown QCP and not a Hertz-Millis type one. The result from linear fitting at $T = 10^{-8}$ is consistently slightly larger, but nevertheless roughly follows the same trend, except for $V = 0.46$. There, the linear fit indicates a maximum, in contrast to RPT, which suggests that the Fermi liquid scale is already only of order 10^{-8} at $V = 0.46$. At the larger temperature $T = 10^{-6}$, this is more obvious. While away from the QCP, the result closely follows the $T = 10^{-8}$ line, it considerably deviates for $0.45 < V < 0.47$ and clearly does not diverge, indicating that in this parameter regime, the Fermi liquid scale is already smaller than 10^{-6}. Note that Z^{-1} is larger on the RKKY side than on the Kondo side, a peculiar phenomenon which also shows up in experimental results [78], and which we earlier ascribed to strong AFM spin fluctuations at $\omega \sim \pm 10^{-4}$. A clear explanation on firmer grounds however is still missing.

The suppression of the Fermi liquid scale can best be observed from the flow of the energy spectra generated by NRG, presented in Fig. 7.12. Here, the spectra for both even and odd NRG iterations, rescaled by their respective energy scale, are shown for both $V = 0.455 < V_c$ and $V = 0.46 > V_c$. First of all, in both cases a Fermi liquid spectrum can be observed in the low energy fixed point. The crossover scale to the Fermi liquid, however, is extremely low, at around $\sim 10^{-7}$ for $V = 0.455$ and $\sim 10^{-8}$ for $V = 0.46$, which is of the same order as the temperature used there. This explains the different behavior between the RPT and linear fit results for Z^{-1} at $V = 0.46$ and $T = 10^{-8}$ in Fig. 7.11. Also, we observe an intermediate fixed point at energy scales above the Fermi liquid one, extending over several orders in energy scale. It is noticeable that this the intermediate fixed point extends over roughly the same energy scales as the AFM spin fluctuations in Fig. 7.10 at the respective V. This suggests that the critical spin fluctuations are described by this intermediate fixed point, though a determination of its nature is unfortunately still missing. Strikingly, the spectra for $V = 0.46$ and $V = 0.455$ are quite similar, though with even and odd iterations interchanged. This suggests that, when going from $V = 0.46$ to $V = 0.455$ over the QCP, some tightly bound object formed over early Wilson chain sites unbinds at the transition, or vice versa. Presumably, this is related the unbinding of c-f-orbital composites at the transition.

7.4.2 Fermi surface reconstruction

After establishing the suppression of the Fermi liquid scale at the QCP and the resulting vanishing of the quasiparticle fraction, we would like to have a look at the second hallmark of the

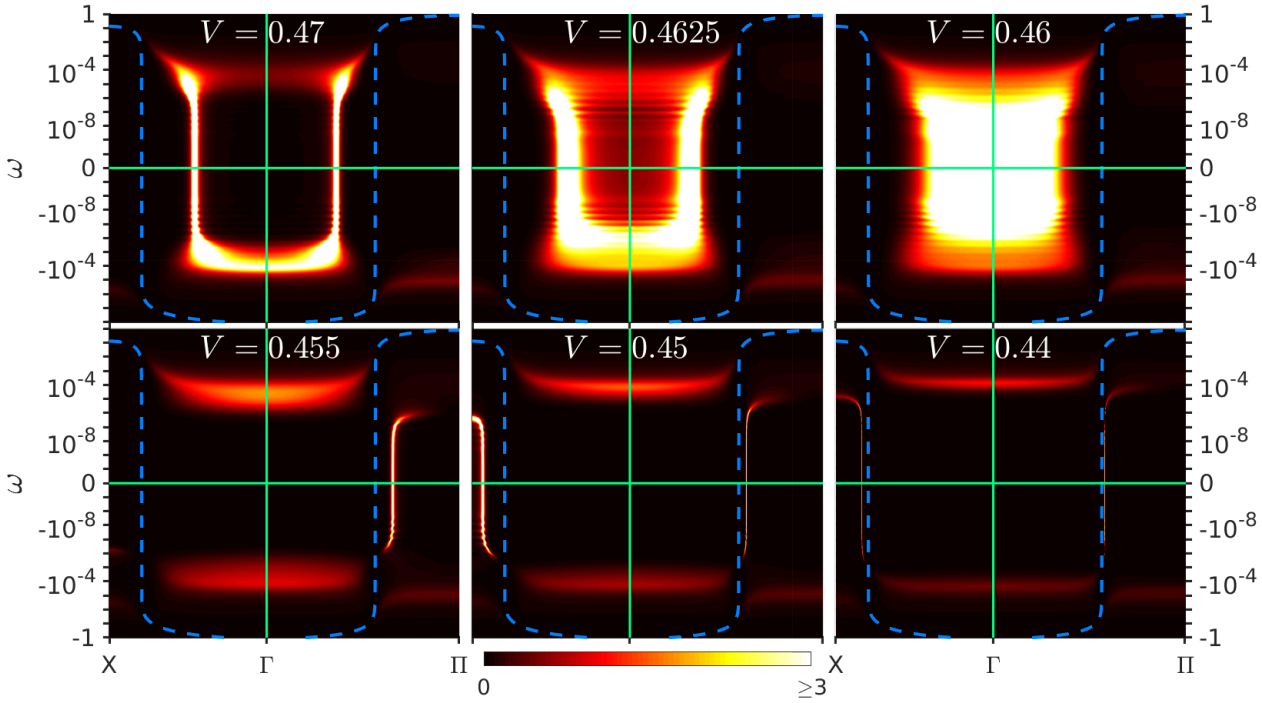

Figure 7.13: Evolution of the $\vec{k}$-resolved f-electron spectral function across the QCP on a logarithmic frequency scale. The critical hybridization is $V_c = 0.4575$ while for $V < V_c$ or $V > V_c$, the system is in an RKKY or a Kondo phase, respectively. It is shown on a $\vec{k}$ path going from $X = (\pi, \pi, 0)$ over $\Gamma = (0, 0, 0)$ to $\Pi = (\pi, \pi, \pi)$. The blue dashed line shows the $V = 0$ c-electron dispersion.

Kondo breakdown, namely the reconstruction of the Fermi surface, accompanied by an experimentally observable change in the Hall coefficient, displayed in Fig. 7.2. To do that, repreiodized results are required and therefore, all results following here are computed with a reperiodized self-energy, done via Eq. (7.15), except for the particle numbers shown in Fig. 7.16.

We begin by investigating the evolution of the $\vec{k}$ resolved spectral function for both the f-electrons (Fig. 7.13) and the c-orbitals (Fig. 7.14) across the QCP. From the f spectral function in Fig. 7.13, we see that in the Kondo regime, it contributes considerable weight at the Fermi level. The Fermi surface is close to the Γ-point, as has already pointed out earlier. When moving towards the transition, we see that the spectral weight moves towards the Γ-point and gets considerably smeared out while it becomes increasingly hard to define a point where the spectral function crosses the Fermi level. This in turn means that the Fermi surface becomes somewhat indeterminate, and one may speak of Fermi surface fluctuations, a term used by Paschen *et al.* in [86]. At $V = 0.46$, where this is most extreme, the spectral weight becomes completely pulled towards the Γ-point and vanishes there at the QCP, to reappear at the Π-point after the QCP at $V = 0.455$. Note that despite the missing Kondo peak in the RKKY phase, spectral weight of the f-orbitals is still clearly visible crossing the Fermi level, though it readily dwindles when moving away from the transition. Also, the flat features near $\omega \simeq \pm 10^{-4}$ should be noted, which are part of the three band structure already mentioned earlier and appear at

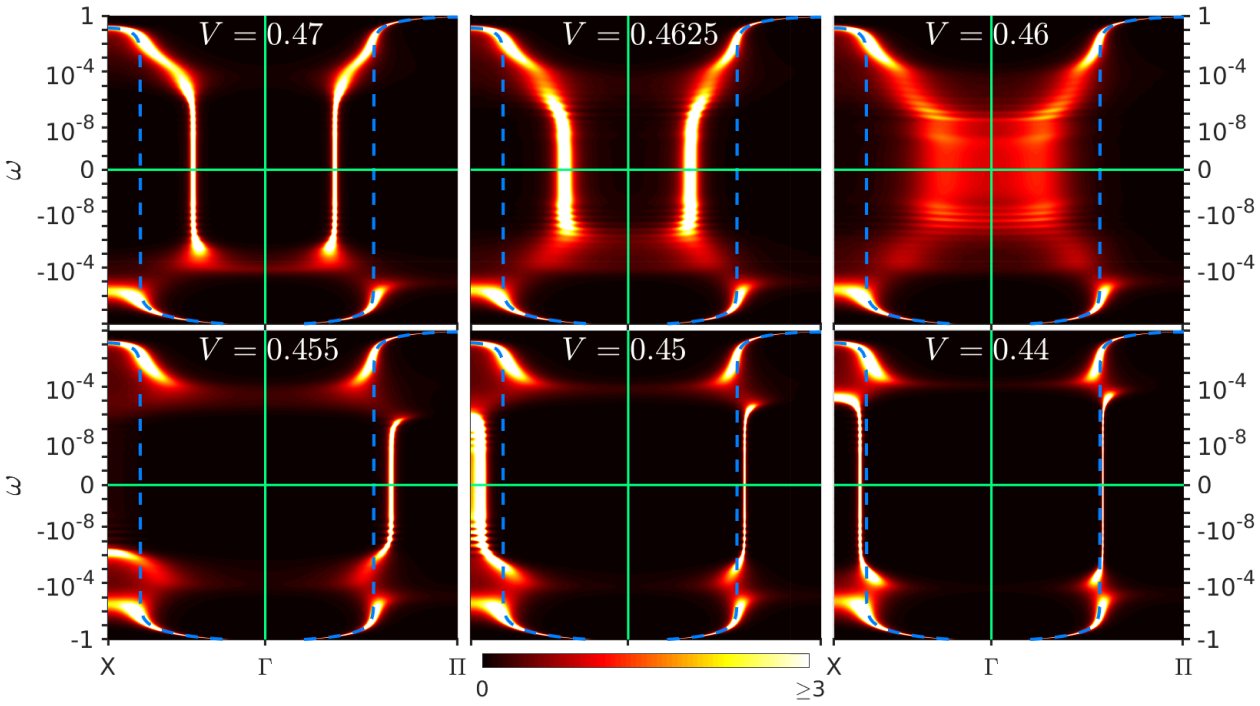

Figure 7.14: Behavior of the $\vec{k}$-dependent c-electron spectral function across the QCP on a logarithmic ω-scale. The path through the Brillouin zone goes from $X = (\pi, \pi, 0)$ over $\Gamma = (0, 0, 0)$ to $\Pi = (\pi, \pi, \pi)$. For $V > V_c = 0.4575$, shown in the upper panels, the system is in a Kondo phase, while for $V < V_c$, it is in an RKKY phase. As a reference, the $V = 0$ dispersion is shown as a blue, dashed line.

the typical energy scale for AFM spin fluctuations in the RKKY phase. We see in Fig. 7.14, that the three band structure is completed by the c-electrons, which is needed to cross the lines of the $V = 0$-dispersion, denoted by the dashed blue line, where the f-electron Green's function necessarily has zeros.

For the c-electrons, we further see that in the Kondo phase, locations with reduced spectral weight start to develop at $V = 0.47$ below $\omega \simeq \pm 10^{-4}$, which become more extended when further moving towards the QCP. Presumably, this is connected to the AFM spin fluctuations becoming quantum critical, extending from $\omega \simeq \pm 10^{-4}$ towards ever lower energies. Directly before the transition, the spectral weight becomes extremely smeared out over $\vec{k}$ near $\omega = 0$, as was already observed for the f-orbitals. However, the c-electrons contribute considerably less weight at the Fermi level. This suddenly changes on the RKKY side of the QCP, at $V = 0.455$, where the c-electrons not only contribute considerably more spectral weight at the Fermi level than the f ones, but the point of crossing $\omega = 0$ also becomes well defined again. It is noticeable that the c spectral function around $\omega = 0$ becomes sharper as V is further lowered, signaling its decoupling from the f-orbitals. All in all this suggests that the Fermi surface gets pulled towards the Γ-point when approaching the QCP from the Kondo side and jumps to the Π-point at the QCP, to then settle at the $V = 0$ Fermi surface when V is further lowered.

That this is indeed the case can be seen from the illustration of the Fermi surface across the

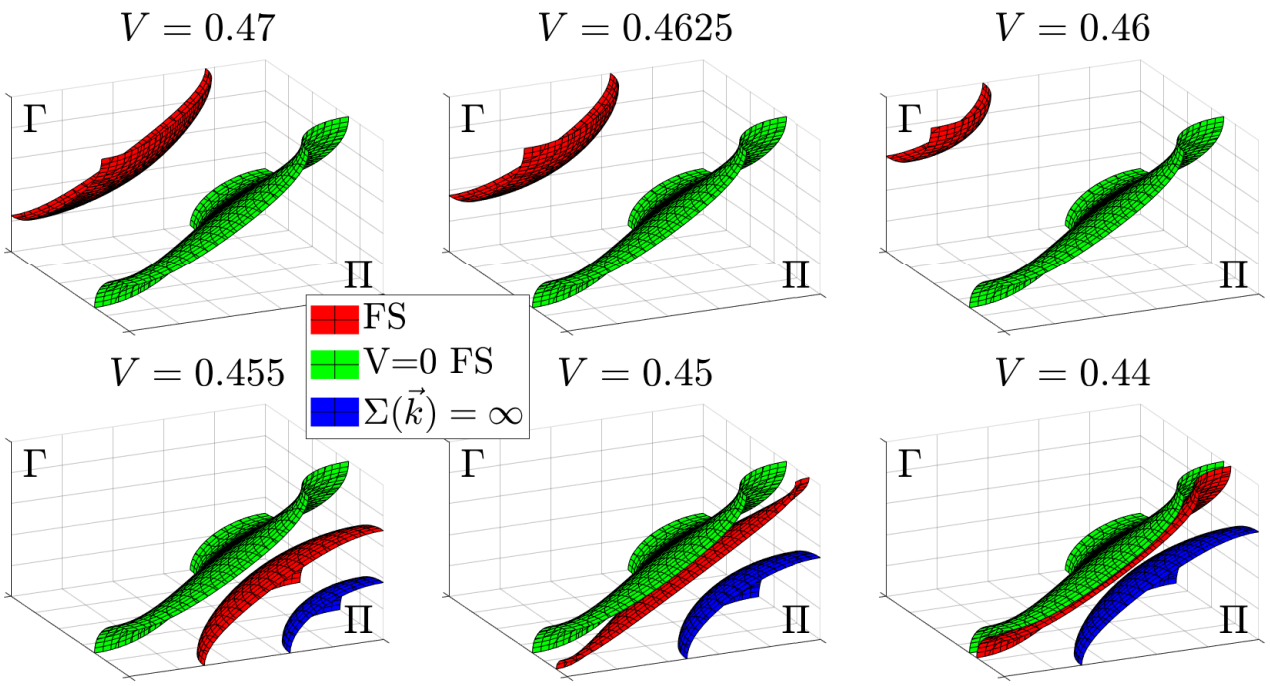

Figure 7.15: Illustration of the Fermi surface (red) reconstructing across the QCP, shown in one octant of the Brillouin zone. The $\Gamma = (0, 0, 0)$-point is in the upper left corner while the $\Pi = (\pi, \pi, \pi)$ is in the lower right corner. In the upper panels, the system is in the Kondo phase while in the lower ones, it is in the RKKY phase. For reference, the $V = 0$ Fermi surface (green) is shown. In the RKKY phase, a $\Sigma(\vec{k}, \omega = 0)$-surface (blue) shows up, calculated via $\mathrm{Re}(M(\vec{k}, \omega = 0)) \stackrel{!}{=} 0$.

QCP in Fig. 7.15. Here, the Fermi surface was again determined by the zeros of the inverse c-electron Green's function at $\omega = 0$, Eq. (7.17). However, at $V = 0.46$, the real part zeros of the inverse f-electron Green's function gives a surface even closer to the Γ-point (not shown) than the one shown, a clear manifestation of the Fermi surface fluctuations already discussed above. Starting from the Kondo side at $V = 0.47$, we see that the Fermi surface closes in towards Γ, reducing in volume. Note that the particle number on the other hand does not decrease, but rather slightly but almost unnoticeable increases, as shown in Fig. 7.16. After the transition on the RKKY side at $V = 0.455$, the Fermi surface jumps towards the Π-point, accompanied by the emergence of a $\Sigma(\vec{k}, \omega = 0) = \infty$ surface between Π-point and Fermi surface. As already mentioned, the Fermi surface then quickly moves towards the corresponding $V = 0$ surface,

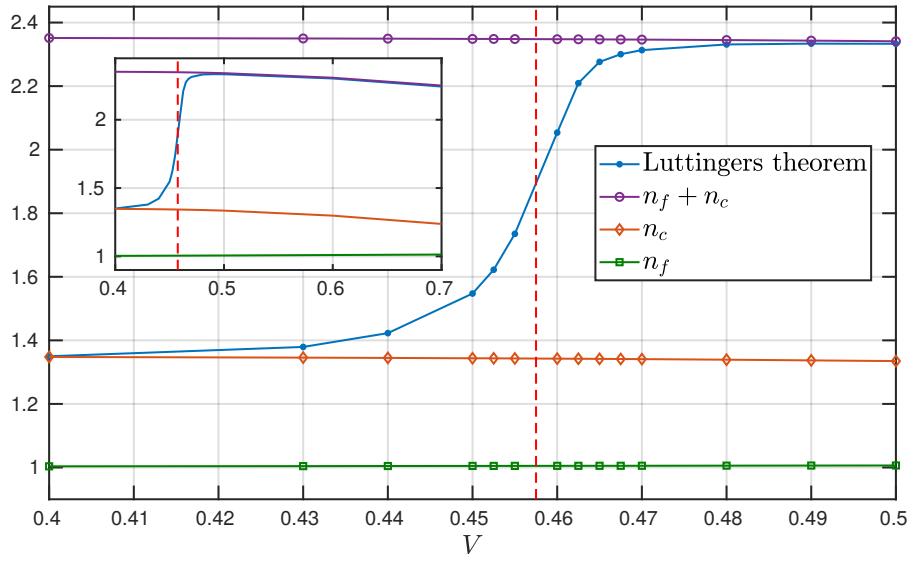

Figure 7.16: Evolution of the actual particle densities and the density calculated from the Fermi surface volume via Luttingers theorem Eq. (7.3) across the QCP. The red dashed line shows the critical hybridization $V_c = 0.4575$, while the inset shows a larger range of V. For $V > V_c$, the system is in the Kondo phase while for $V < V_c$, it is in the RKKY phase.

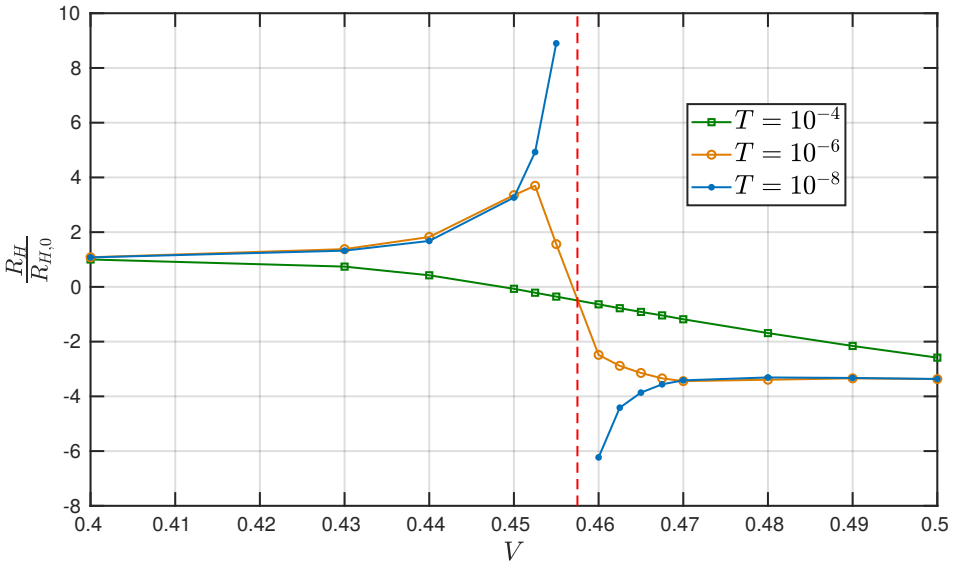

Figure 7.17: Evolution of the Hall coefficient R_H across the QCP for different temperatures, normalized to its value $R_{H,0}$ at $V = 0$. While at large temperatures ($T = 10^{-4}$), a smooth crossover can be observed, which sharpens when temperature is lowered ($T = 10^{-6}$), the Hall coefficient finally diverges close to $T = 0$ ($T = 10^{-8}$). The critical point is at $V_c = 0.4575$, denoted by the red dashed line, while for $V > V_c$ or $V < V_c$, the system is in a Kondo or RKKY phase respectively. To be compared with the experimental results in Fig. 7.2.

followed by the $\Sigma(\vec{k}, \omega = 0) = \infty$ surface. It finally becomes sandwiched between these two surfaces, leading to the suppression of $G_f(\vec{k}, \omega = 0)$ at the Fermi surface as it has zeros at both the $V = 0$ and $\Sigma(\vec{k}, \omega = 0) = \infty$ surfaces.

The change in the Fermi surface described here of course leads to a corresponding difference in actual particle number and the one predicted via the Fermi surface volume by Luttingers theorem Eq. (7.3). This is shown in Fig. 7.16, where both the actual particle numbers and the ones calculated from Eq. (7.3) are displayed. We see that Luttingers theorem is nicely obeyed far from the transition at $V \geq 0.5$, but becomes gradually violated when approaching the transition. The Fermi surface volume seems to continuously decrease through the QCP, to settle at a volume consistent with the particle density of the c-electrons. We see here that the Fermi surface volume therefore does not jump, but rather evolves continuously through the transition. Nevertheless, a clear critical point can be made out, on grounds criteria like the appearance of a $\Sigma(\vec{k}, \omega = 0) = \infty$ surface, the divergence of Z^{-1} and most importantly, the NRG flow Fig. 7.12, impressively showing the suppression of the Fermi liquid scale at the QCP and the emergence of a different Fermi liquid when the QCP is crossed.

Before concluding the discussion on the KB QCP in the CDMFT approximation, we would like to qualitatively compare the theoretically computed Hall coefficient, displayed in Fig. 7.17, with the experimental result from [86], shown in Fig. 7.2. We see that at $T = 10^{-8}$, the theoretical Hall coefficient diverges at the transition, signaling that no charge carriers contributing to the Hall effect are available at the transition. One may infer that this can already be guessed from the volume of the Fermi surface in Fig. 7.16, as this moves through 2 when going over the transition, which corresponds to a completely filled band that does not show a Hall response. Nevertheless, this result is completely unexpected and could not have been guessed from the experimental result in Fig. 7.2, which has however been obtained at small but finite temperatures. We therefore also considered higher temperatures in the numerical calculation. In Fig. 7.17 we see that the evolution of the Hall coefficient starts out with a smooth crossover at $T = 10^{-4}$, which sharpens as the temperature is lowered towards $T = 10^{-6}$, quite in line with the experimental observations. However, the experimental situation is more complicated, as more than one band may contribute to the Fermi surface. As resistivities do not add up in this case, but rather their inverses should be added, there might still be only a sharp crossover visible in experiments for $T \to 0$. This has to be investigated more closely in the future. Note that the sign change of the Hall coefficient is expected, as the Fermi surface changes from particle like in the Kondo regime to hole like in the RKKY phase.

8 Outlook

During this thesis, the numerical renormalization group has been used as a cluster solver for quantum cluster methods. This was inspired by the success of the NRG code, available and thoroughly tested at Jan von Delft's group, when confronted with DMFT calculations. For cluster extensions however, an efficient and accurate integration method for Green's functions had to be implemented, which was the main technical challenge during the course of this thesis. The resulting routines, based on the tetrahedron method, have turned out sufficiently fast and accurate to be practical, at least for the presented problems.

With the two dimensional Hubbard model in a two patch DCA approximation as a testing environment, the NRG combined with the tetrahedron method was able to produce results in good agreement with earlier CTQMC calculations, done by Ferrero *et al.* [7].

This has set the stage for the investigation of the quantum critical point in heavy fermion compounds, where the periodic Anderson model in a two-site CDMFT approximation was employed. There, the NRG revealed its true power, being able to resolve exponentially small energy scales and having arbitrary low temperatures accessible. It allowed for the investigation of the QCP with to date unprecedented accuracy. The ability to calculate real frequency response functions allowed to show that antiferromagnetic spin fluctuations become long ranged in time, while the flow of the eigenspectra generated by the NRG impressively demonstrated the suppression of the Fermi liquid scale at the QCP. Such results will presumably not be available with other cluster solvers in the near future, if ever. All in all, the results chapter 7 are extremely encouraging and shows that the NRG is an invaluable tool to help shed light on quantum criticality in strongly correlated systems, and its relation to their peculiar phenomenology. However, much has still to be done to interpret and further these results, and they will surely lead to a lot of fruitful work in the future.

The calculations done in this paper also set the stage for further projects. In the case of heavy fermion systems, it may actually be desirable to investigate the periodic Anderson model on a frustrated lattice. This is motivated by the experimental results [88] that the antiferromagnetic and Kondo breakdown QCPs can be detached, leading to the proposal that frustration is an important tuning parameter in these systems [90]. The advantage would be that in this case, a three site cluster could be used, allowing to increase the cluster size of our two-site results to a size still in reach of NRG. This would allow, to some extent, to investigate dependence of the quantum critical behavior on cluster size and may shed light on the robustness of the obtained results.

Further, four-site cluster calculations with NRG are highly desirable in the future and may already be in reach of the NRG code available at Jan von Delft's group. These may then, among other things, shed light not only on unconventional superconductivity in strongly correlated systems, but also its proposed relation to quantum criticality.

References

[1] J. G. Bednorz and K. A. Müller. "Possible high-T_c superconductivity in the Ba-La-Cu-O system". In: *Z. Physik B - Condensed Matter* 64.2 (1986), pp. 189–193.

[2] Antoine Georges et al. "Dynamical mean-field theory of strongly correlated fermion systems and the limit of infinite dimensions". In: *Rev. Mod. Phys.* 68.1 (1996), pp. 13–125.

[3] Thomas Maier et al. "Quantum cluster theories". In: *Rev. Mod. Phys.* 77.3 (2005), pp. 1027–1080.

[4] Ralf Bulla, Theo A. Costi, and Thomas Pruschke. "Numerical renormalization group method for quantum impurity systems". In: *Rev. Mod. Phys.* 80.2 (2008), pp. 395–450.

[5] Thomas Pruschke et al. "DCA for the 2D Hubbard Model at T $\to$ 0". In: *High Performance Computing in Science and Engineering, Munich 2004*. Ed. by Siegfried Wagner et al. Springer Berlin Heidelberg, 2005, pp. 309–318.

[6] Žiga Osolin and Rok Žitko. "Fine structure of the spectra of the Kondo lattice model: Two-site cellular dynamical mean-field theory study". In: *Phys. Rev. B* 95.3 (2017), p. 035107.

[7] M. Ferrero et al. "Interplane charge dynamics in a valence-bond dynamical mean-field theory of cuprate superconductors". In: *Phys. Rev. B* 82.5 (2010), p. 054502.

[8] Lorenzo De Leo, Marcello Civelli, and Gabriel Kotliar. "$T = 0$ Heavy-Fermion Quantum Critical Point as an Orbital-Selective Mott Transition". In: *Phys. Rev. Lett.* 101.25 (2008), p. 256404.

[9] Lorenzo De Leo, Marcello Civelli, and Gabriel Kotliar. "Cellular dynamical mean-field theory of the periodic Anderson model". In: *Phys. Rev. B* 77.7 (2008), p. 075107.

[10] Dieter Vollhardt. "Dynamical Mean-Field Theory of Electronic Correlations in Models and Materials". In: *arXiv:1004.5069 [cond-mat]* (2010), pp. 339–403. arXiv: 1004.5069.

[11] Walter Metzner and Dieter Vollhardt. "Correlated Lattice Fermions in $d = \infty$ Dimensions". In: *Phys. Rev. Lett.* 62.3 (1989), pp. 324–327.

[12] Antoine Georges and Gabriel Kotliar. "Hubbard model in infinite dimensions". In: *Phys. Rev. B* 45.12 (1992), pp. 6479–6483.

[13] Gordon Baym and Leo P. Kadanoff. "Conservation Laws and Correlation Functions". In: *Phys. Rev.* 124.2 (1961), pp. 287–299.

[14] Gordon Baym. "Self-Consistent Approximations in Many-Body Systems". In: *Phys. Rev.* 127.4 (1962), pp. 1391–1401.

[15] M. Potthoff. "Self-energy-functional approach to systems of correlated electrons". In: *The European Physical Journal B - Condensed Matter and Complex Systems* 32.4 (2003), pp. 429–436.

[16] M. Potthoff. "Self-energy-functional theory". In: *Strongly Correlated Systems: Theoretical Methods* (2012).

[17] Piers Coleman. *Introduction to Many-Body Physics*. Cambridge University Press, 2015.

[18] Alexander Altland and Ben D. Simons. *Condensed Matter Field Theory*. Cambridge University Press, 2010.

[19] J. M. Luttinger and J. C. Ward. "Ground-State Energy of a Many-Fermion System. II". In: *Phys. Rev.* 118.5 (1960), pp. 1417–1427.

[20] Michael Potthoff. "Non-perturbative construction of the Luttinger-Ward functional". In: *Condens. Mat. Phys.* 9 (2006), p. 557.

[21] E. Müller-Hartmann. "Correlated fermions on a lattice in high dimensions". In: *Z. Physik B - Condensed Matter* 74.4 (1989), pp. 507–512.

[22] P. G. J. van Dongen, F. Gebhard, and D. Vollhardt. "Variational evaluation of correlation functions for lattice electrons in high dimensions". In: *Z. Physik B - Condensed Matter* 76.2 (1989), pp. 199–210.

[23] Walter Metzner. "Variational theory for correlated lattice fermions in high dimensions". In: *Z. Physik B - Condensed Matter* 77.2 (1989), pp. 253–266.

[24] Gabriel Kotliar et al. "Cellular Dynamical Mean Field Approach to Strongly Correlated Systems". In: *Phys. Rev. Lett.* 87.18 (2001), p. 186401.

[25] M. H. Hettler et al. "Nonlocal dynamical correlations of strongly interacting electron systems". In: *Phys. Rev. B* 58.12 (1998), R7475–R7479.

[26] M. H. Hettler et al. "Dynamical cluster approximation: Nonlocal dynamics of correlated electron systems". In: *Phys. Rev. B* 61.19 (2000), pp. 12739–12756.

[27] Th. A. Maier, Th. Pruschke, and M. Jarrell. "Angle-resolved photoemission spectra of the Hubbard model". In: *Phys. Rev. B* 66.7 (2002), p. 075102.

[28] Giulio Biroli and Gabriel Kotliar. "Cluster methods for strongly correlated electron systems". In: *Phys. Rev. B* 65.15 (2002), p. 155112.

[29] Tudor D. Stanescu et al. "A cellular dynamical mean field theory approach to Mottness". In: *Annals of Physics*. July 2006 Special Issue 321.7 (2006), pp. 1682–1715.

[30] Tudor D. Stanescu and Gabriel Kotliar. "Fermi arcs and hidden zeros of the Green function in the pseudogap state". In: *Phys. Rev. B* 74.12 (2006), p. 125110.

[31] B. Kyung et al. "Pseudogap induced by short-range spin correlations in a doped Mott insulator". In: *Phys. Rev. B* 73.16 (2006), p. 165114.

[32] Michel Ferrero et al. "Pseudogap opening and formation of Fermi arcs as an orbital-selective Mott transition in momentum space". In: *Phys. Rev. B* 80.6 (2009), p. 064501.

[33] G. Biroli, O. Parcollet, and G. Kotliar. "Cluster dynamical mean-field theories: Causality and classical limit". In: *Phys. Rev. B* 69.20 (2004), p. 205108.

[34] Peter Staar, Thomas Maier, and Thomas C. Schulthess. "Dynamical cluster approximation with continuous lattice self-energy". In: *Phys. Rev. B* 88.11 (2013), p. 115101.

[35] Peter Staar, Thomas Maier, and Thomas C. Schulthess. "Two-particle correlations in a dynamic cluster approximation with continuous momentum dependence: Superconductivity in the two-dimensional Hubbard model". In: *Phys. Rev. B* 89.19 (2014), p. 195133.

[36] Avraham Schiller and Kevin Ingersent. “Systematic $1/d$ Corrections to the Infinite-Dimensional Limit of Correlated Lattice Electron Models”. In: *Phys. Rev. Lett.* 75.1 (1995), pp. 113–116.

[37] J. Vučičević et al. “Practical consequences of the Luttinger-Ward functional multivaluedness for cluster DMFT methods”. In: *Phys. Rev. B* 97.12 (2018), p. 125141.

[38] Torben Jabben, Norbert Grewe, and Sebastian Schmitt. “Extension of dynamical mean-field theory by inclusion of nonlocal two-site correlations with variable distance”. In: *Phys. Rev. B* 85.16 (2012), p. 165122.

[39] S. Okamoto et al. “Fictive impurity models: An alternative formulation of the cluster dynamical mean-field method”. In: *Phys. Rev. B* 68.19 (2003), p. 195121.

[40] Evgeny Kozik, Michel Ferrero, and Antoine Georges. “Nonexistence of the Luttinger-Ward Functional and Misleading Convergence of Skeleton Diagrammatic Series for Hubbard-Like Models”. In: *Phys. Rev. Lett.* 114.15 (2015), p. 156402.

[41] O. Gunnarsson et al. “Breakdown of Traditional Many-Body Theories for Correlated Electrons”. In: *Phys. Rev. Lett.* 119.5 (2017), p. 056402.

[42] Kenneth G. Wilson. “The renormalization group: Critical phenomena and the Kondo problem”. In: *Rev. Mod. Phys.* 47.4 (1975), pp. 773–840.

[43] H. R. Krishna-murthy, J. W. Wilkins, and K. G. Wilson. “Renormalization-group approach to the Anderson model of dilute magnetic alloys. I. Static properties for the symmetric case”. In: *Phys. Rev. B* 21.3 (1980), pp. 1003–1043.

[44] Frithjof B. Anders and Avraham Schiller. “Real-Time Dynamics in Quantum-Impurity Systems: A Time-Dependent Numerical Renormalization-Group Approach”. In: *Phys. Rev. Lett.* 95.19 (2005), p. 196801.

[45] Andreas Weichselbaum and Jan von Delft. “Sum-Rule Conserving Spectral Functions from the Numerical Renormalization Group”. In: *Phys. Rev. Lett.* 99.7 (2007), p. 076402.

[46] Andreas Weichselbaum. “Tensor networks and the numerical renormalization group”. In: *Phys. Rev. B* 86.24 (2012), p. 245124.

[47] Andreas Weichselbaum. “Non-abelian symmetries in tensor networks: A quantum symmetry space approach”. In: *Annals of Physics* 327.12 (2012), pp. 2972–3047.

[48] L. N. Oliveira et al. “Renormalization-group calculation of dynamical properties for impurity models”. In: *Physica B: Condensed Matter* 171.1 (1991), pp. 61–68.

[49] Wanda C. Oliveira and Luiz N. Oliveira. “Generalized numerical renormalization-group method to calculate the thermodynamical properties of impurities in metals”. In: *Phys. Rev. B* 49.17 (1994), pp. 11986–11994.

[50] Rok Žitko and Thomas Pruschke. “Energy resolution and discretization artifacts in the numerical renormalization group”. In: *Phys. Rev. B* 79.8 (2009), p. 085106.

[51] Rok Žitko. “Adaptive logarithmic discretization for numerical renormalization group methods”. In: *Computer Physics Communications* 180.8 (2009), pp. 1271–1276.

[52] Seung-Sup B. Lee and Andreas Weichselbaum. “Adaptive broadening to improve spectral resolution in the numerical renormalization group”. In: *Phys. Rev. B* 94.23 (2016), p. 235127.

[53] Andrew K. Mitchell et al. “Generalized Wilson chain for solving multichannel quantum impurity problems”. In: *Phys. Rev. B* 89.12 (2014), p. 121105.

[54] K. M. Stadler et al. “Interleaved numerical renormalization group as an efficient multiband impurity solver”. In: *Phys. Rev. B* 93.23 (2016), p. 235101.

[55] O. Jepson and O. K. Anderson. “The electronic structure of h.c.p. Ytterbium”. In: *Solid State Communications* 9.20 (1971), pp. 1763–1767.

[56] G. Lehmann and M. Taut. “On the Numerical Calculation of the Density of States and Related Properties”. In: *Phys. Stat. Sol. (b)* 54.2 (1972), pp. 469–477.

[57] Peter E. Blöchl, O. Jepsen, and O. K. Andersen. “Improved tetrahedron method for Brillouin-zone integrations”. In: *Phys. Rev. B* 49.23 (1994), pp. 16223–16233.

[58] Ph. Lambin and J. P. Vigneron. “Computation of crystal Green’s functions in the complex-energy plane with the use of the analytical tetrahedron method”. In: *Phys. Rev. B* 29.6 (1984), pp. 3430–3437.

[59] J. Molenaar, P. T. Coleridge, and A. Lodder. “An extended tetrahedron method for determining Fourier components of Green functions in solids”. In: *J. Phys. C: Solid State Phys.* 15.34 (1982), pp. 6955–6969.

[60] S. Kaprzyk and P. E. Mijnarends. “A simple linear analytic method for Brillouin zone integration of spectral functions in the complex energy plane”. In: *J. Phys. C: Solid State Phys.* 19.9 (1986), pp. 1283–1292.

[61] Mitsuaki Kawamura, Yoshihiro Gohda, and Shinji Tsuneyuki. “Improved tetrahedron method for the Brillouin-zone integration applicable to response functions”. In: *Phys. Rev. B* 89.9 (2014), p. 094515.

[62] S. Kaprzyk. “An algebraic formulation and implementation of the tetrahedron linear method for the Brillouin zone integration of spectral functions”. In: *Computer Physics Communications* 183.2 (2012), pp. 347–362.

[63] V. I. Anisimov et al. “First-principles calculations of the electronic structure and spectra of strongly correlated systems: dynamical mean-field theory”. In: *J. Phys.: Condens. Matter* 9.35 (1997), pp. 7359–7367.

[64] Tohru Morita. “Useful Procedure for Computing the Lattice Green’s Function-Square, Tetragonal, and bcc Lattices”. In: *Journal of Mathematical Physics* 12.8 (1971), pp. 1744–1747.

[65] G. S. Joyce. “Exact evaluation of the simple cubic lattice Green function for a general lattice point”. In: *J. Phys. A: Math. Gen.* 35.46 (2002), pp. 9811–9828.

[66] Emanuel Gull et al. “Continuous-time Monte Carlo methods for quantum impurity models”. In: *Rev. Mod. Phys.* 83.2 (2011), pp. 349–404.

[67] B. Keimer et al. “From quantum matter to high-temperature superconductivity in copper oxides”. In: *Nature* 518.7538 (2015), pp. 179–186.

[68] Makoto Hashimoto et al. “Energy gaps in high-transition-temperature cuprate superconductors”. In: *Nature Physics* 10.7 (2014), pp. 483–495.

[69] Andrea Damascelli, Zahid Hussain, and Zhi-Xun Shen. “Angle-resolved photoemission studies of the cuprate superconductors”. In: *Rev. Mod. Phys.* 75.2 (2003), pp. 473–541.

[70] Kyle M. Shen et al. “Nodal Quasiparticles and Antinodal Charge Ordering in $Ca_{2-x}Na_xCuO_2Cl_2$”. In: *Science* 307.5711 (2005), pp. 901–904.

[71] Ping Sun and Gabriel Kotliar. “Understanding the Heavy Fermion Phenomenology from a Microscopic Model”. In: *Phys. Rev. Lett.* 95.1 (2005), p. 016402.

[72] D. Tanasković et al. “Phase diagram, energy scales, and nonlocal correlations in the Anderson lattice model”. In: *Phys. Rev. B* 84.11 (2011), p. 115105.

[73] Hilbert v. Löhneysen et al. “Fermi-liquid instabilities at magnetic quantum phase transitions”. In: *Rev. Mod. Phys.* 79.3 (2007), pp. 1015–1075.

[74] Piers Coleman. “Heavy Fermions: Electrons at the Edge of Magnetism”. In: *Handbook of Magnetism and Advanced Magnetic Materials*. American Cancer Society, 2007.

[75] O. Trovarelli et al. “$YbRh_2Si_2$: Pronounced Non-Fermi-Liquid Effects above a Low-Lying Magnetic Phase Transition”. In: *Phys. Rev. Lett.* 85.3 (2000), pp. 626–629.

[76] P. Gegenwart et al. “Magnetic-Field Induced Quantum Critical Point in $YbRh_2Si_2$”. In: *Phys. Rev. Lett.* 89.5 (2002), p. 056402.

[77] P. Gegenwart et al. “High-field phase diagram of the heavy-fermion metal YbRh2Si2”. In: *New J. Phys.* 8.9 (2006), pp. 171–171.

[78] C. Krellner et al. “Violation of Critical Universality at the Antiferromagnetic Phase Transition of $YbRh_2Si_2$”. In: *Phys. Rev. Lett.* 102.19 (2009), p. 196402.

[79] S. Doniach. “The Kondo lattice and weak antiferromagnetism”. In: *Physica B+C* 91 (1977), pp. 231–234.

[80] P. Coleman et al. “How do Fermi liquids get heavy and die?” In: *J. Phys.: Condens. Matter* 13.35 (2001), R723–R738.

[81] John A. Hertz. “Quantum critical phenomena”. In: *Phys. Rev. B* 14.3 (1976), pp. 1165–1184.

[82] A. J. Millis. “Effect of a nonzero temperature on quantum critical points in itinerant fermion systems”. In: *Phys. Rev. B* 48.10 (1993), pp. 7183–7196.

[83] J. M. Luttinger. “Fermi Surface and Some Simple Equilibrium Properties of a System of Interacting Fermions”. In: *Phys. Rev.* 119.4 (1960), pp. 1153–1163.

[84] T. Senthil, Subir Sachdev, and Matthias Vojta. “Fractionalized Fermi Liquids”. In: *Phys. Rev. Lett.* 90.21 (2003), p. 216403.

[85] Qimiao Si et al. “Locally critical quantum phase transitions in strongly correlated metals”. In: *Nature* 413.6858 (2001), p. 804.

[86] S. Paschen et al. “Hall-effect evolution across a heavy-fermion quantum critical point”. In: *Nature* 432.7019 (2004), pp. 881–885.

[87] Sven Friedemann et al. “Fermi-surface collapse and dynamical scaling near a quantum-critical point”. In: *PNAS* 107.33 (2010), pp. 14547–14551.

[88] S. Friedemann et al. “Detaching the antiferromagnetic quantum critical point from the Fermi-surface reconstruction in YbRh2Si2”. In: *Nature Physics* 5.7 (2009), pp. 465–469.

[89] S. Friedemann et al. “Magnetic and Electronic Quantum Criticality in YbRh2Si2”. In: *J Low Temp Phys* 161.1 (2010), pp. 67–82.

[90] Piers Coleman and Andriy H. Nevidomskyy. “Frustration and the Kondo Effect in Heavy Fermion Materials”. In: *J Low Temp Phys* 161.1 (2010), pp. 182–202.

[91] Ekkehard Lange and Gabriel Kotliar. “Magnetotransport in the doped Mott insulator”. In: *Phys. Rev. B* 59.3 (1999), pp. 1800–1807.

[92] A. C. Hewson. “Renormalized perturbation expansions and Fermi liquid theory”. In: *Phys. Rev. Lett.* 70.25 (1993), pp. 4007–4010.

[93] A. C. Hewson, A. Oguri, and D. Meyer. “Renormalized parameters for impurity models”. In: *Eur. Phys. J. B* 40.2 (2004), pp. 177–189.

Erklärung:

Hiermit erkläre ich, die vorliegende Arbeit selbständig verfasst zu haben und keine anderen als die in der Arbeit angegebenen Quellen und Hilfsmittel benutzt zu haben.

München, 04. Juni 2019

Andreas Gleis